High-Resolution Numerical Simulation of Turbulent Interfacial Marine Flows

by

Grzegorz P. Filip

A dissertation submitted in partial fulfillment
of the requirements for the degree of
Doctor of Philosophy
(Naval Architecture and Marine Engineering)
in the University of Michigan
2013

Doctoral Committee:

Professor Kevin J. Maki, Chair
Professor Luis P. Bernal
Sung-Eun Kim, NSWC Carderock
Professor Armin W. Troesch
Professor Yin Lu Young

"A society grows great when old men plant trees in whose shade they know they shall never sit."

– *Greek proverb*

2013

Dedicated to my family.

ACKNOWLEDGMENTS

I would like to give special thanks to Prof. Kevin Maki for his guidance and friendship, and to my committee members, Prof. Luis Bernal, Dr. Sung-Eun Kim, Prof. Armin Troesch, and Prof. Yin Lu Young.

I want to thank my family, especially my parents, Adam and Irena, for their continuous encouragement and support. Special thanks to all my friends who made this endeavor a very memorable part of my life.

This dissertation was funded by the Department of Defense via the National Defense Science and Engineering Graduate (NDSEG) fellowship and it is gratefully acknowledged together with the additional support from the US Office of Naval Research (ONR) grants N00014-10-1-0301 and N00014-11-1-0846.

I would like to acknowledge the Extreme Science and Engineering Discovery Environment (XSEDE), which is supported by National Science Foundation grant number OCI-1053575, and the Computer Aided Engineering Network High Performance Computing (CAEN HPC) Group at the University of Michigan.

TABLE OF CONTENTS

LIST OF FIGURES

LIST OF TABLES

ABSTRACT

High-Resolution Numerical Simulation of Turbulent Interfacial Marine Flows

by

Grzegorz P. Filip

Chair: Kevin J. Maki

An important aspect of designing offshore structures and seagoing vessels is an accurate prediction of the loads associated with wave impacts. In regions near the shore or during storms at sea, breaking waves are a common occurrence and the loading caused by their impact is typically more severe than in the case of regular non-breaking waves. Present methods for numerically predicting the impact forces use potential-flow methods with empirically-derived coefficients or relatively low-order methods in the computational-fluid dynamics (CFD) family. The potential-flow methods usually cannot simulate wave breaking and thus correction factors are necessary to account for slamming-like impacts that may occur due to plunging breakers. In some applications of the CFD tools, turbulence models are used to approximate the turbulent wave-breaking process in an effort to improve the prediction of the flow. The present work expands the understanding of the turbulence-interface interaction using highly-resolved numerical simulations to improve the CFD modeling capabilities in marine applications.

The complex behavior of turbulence in the proximity of a deformable interface separating two incompressible phases is studied using two variants of CFD: direct numerical simulations (DNS) and large-eddy simulations (LES) that require modeling of the turbulence closure terms. Canonical flows are studied with DNS to determine the influence of the information typically not resolved by lower-order CFD methods and to establish the hierarchy of the modeling terms present in the governing equations. The relative magnitude of the convective and the interfacial subgrid terms are found to be significant and thus not negligible for a plunging-breaking wave flow. A scale-similarity-based model is proposed and implemented in the LES solver to include the effects of the unresolved flow features associated with the presence of the interface. The model is found to successfully approximate the subgrid behavior in multiphase flows with sufficient spatial and temporal resolution. The multiphase LES framework is extended to the study of breaking waves impinging on an offshore platform and the importance of the subgrid modeling to an accurate prediction of forces on the structure in demonstrated.

CHAPTER 1

Introduction

High-fidelity numerical simulation of turbulent-interfacial flows is a relatively new research area with applications to many industrial problems. Accurate prediction of such multiphase flows requires an in-depth understanding of the turbulent behavior in each phase and near the deformable interface. Experimental studies and high-resolution numerical tools have allowed for a detailed look into the nature of single-phase turbulence that ultimately resulted in the development of improved turbulence modeling techniques. In the past decade, the same tools have been applied to the study of complex interfacial flows including liquid jet atomization inside of modern engines, particle-laden flows across many industries, and breaking-water waves, among others. The combination of the deformable interface that separates the phases and the immense range of turbulent scales commonly found in these flows poses a major challenge to numerical and experimental studies.

In an experimental study of turbulent-interfacial flows, high-quality data is difficult and expensive to collect because of the chaotic nature of turbulence combined with the complex behavior of interface break-up and coalescence typically occurring on very small time and length-scales. Spilling and plunging breaking water waves are an example of turbulent-interfacial flows common to the marine industry that are particularly difficult to examine experimentally as discussed by Perlin et al. (2013). Furthermore, collecting accurate impact-load data on offshore structures due to im-

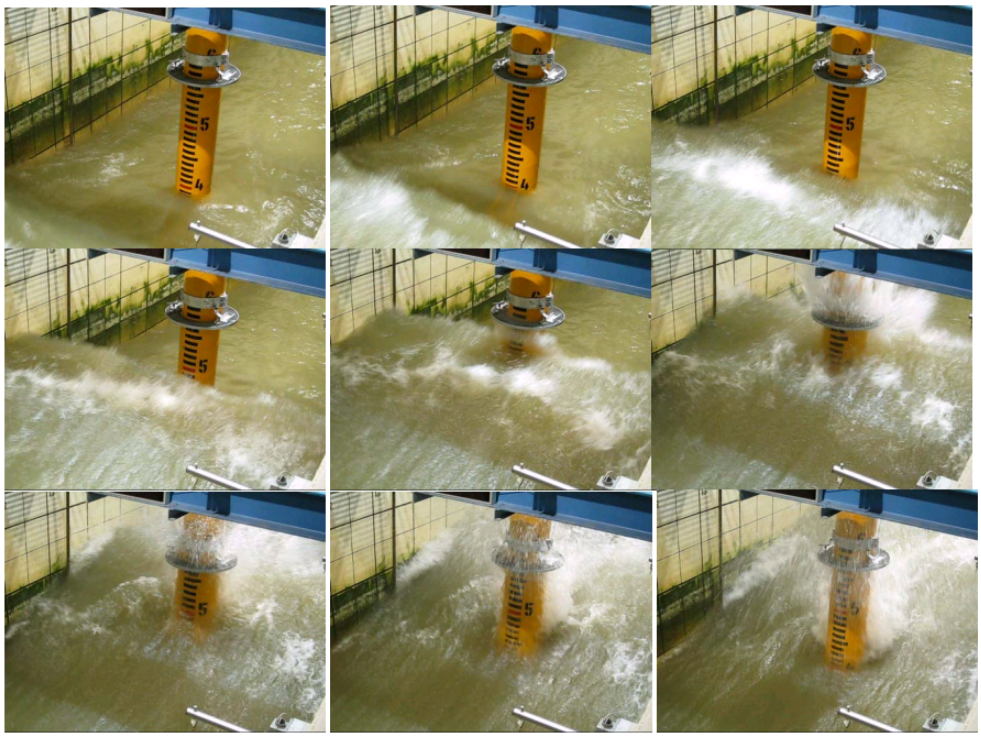

Figure 1.1: Experimental study of plunging-breaking wave impacts on an offshore wind turbine platform (Frigaard et al. (2010))

pinging breaking waves (an example is shown in Figure 1.1) requires an understanding of the breaking process and its interaction with the structure, as well as of the scaling effects. Wienke et al. (2001) has shown that the nature of the impact forces is highly dependent on the initial conditions of the wave and the relative location and type of wave breaking. Nonetheless, many experimental campaigns have set out to characterize the impact loads associated with spilling and plunging breakers in order to enhance the understanding of the problem and to provide empirical corrections for load-prediction methods (Goda et al. (1966), Apelt and Piorewicz (1987), Chan and Melville (1989), Chan et al. (1995), Chakrabarti et al. (1997), Irschik et al. (2002), Zang et al. (2010), Hildebrandt and Schlurmann (2012)). For example, the Morison's equation (Morison (1950)) has been extended in an attempt to incorporate the impact loading using an additional term based on empirically-derived curling and slamming factors. However, the curling and slamming factors used to describe the impact event

are strong functions of the problem setup including the type of wave breaking, position and orientation of the structure, as well as the water depth. The test matrix required to characterize the empirical-correction factors for a typical offshore structure can be large and hence expensive and time consuming.

An alternative to the physical experiments are the computational tools of varying fidelity and accuracy that can also be used to study the complex interaction of breaking waves and offshore structures, as well as other turbulent-interfacial flows. Computational fluid dynamics (CFD) solvers can eliminate the need for empirical coefficients, and impact loads can be computed from a direct integration of the pressure and viscous forces acting on the structure. Additionally, numerical simulations allow for a complete control of the problem's initial conditions and for repeatable results unaffected by random error. In practice, multiple simulations can be executed in parallel using large computing clusters if necessary, whereas in typical experimental campaigns, only one testing facility is used and each experimental run is conducted in sequence. The three variants of the CFD methods relevant to the current work include: direct numerical simulations (DNS), large-eddy simulation (LES), and Reynolds-averaged Navier-Stokes (RANS) solvers.

Direct numerical simulations can provide extremely accurate predictions of turbulent flow but they are usually limited to research applications because of the computational cost associated with the direct representation of the entire turbulent spectrum. The log-log plot shown in Figure 1.2 illustrates the typical distribution of turbulent kinetic energy across the entire spectrum of the length scales (represented by the wave number k) in homoegenous turbulence. In order to conduct direct numerical simulations of such a flow, the energy cascade between all the turbulent scales must be resolved. The energy cascade can be characterized by the transfer of energy from the energy-containing range at low wave numbers (largest turbulent scales) down to the inertial subrange where inertial forces prevail over viscous forces. The forward energy

cascade continues down to the dissipation subrange where turbulent kinetic energy is converted to heat at the molecular level. Direct simulation of the entire range of

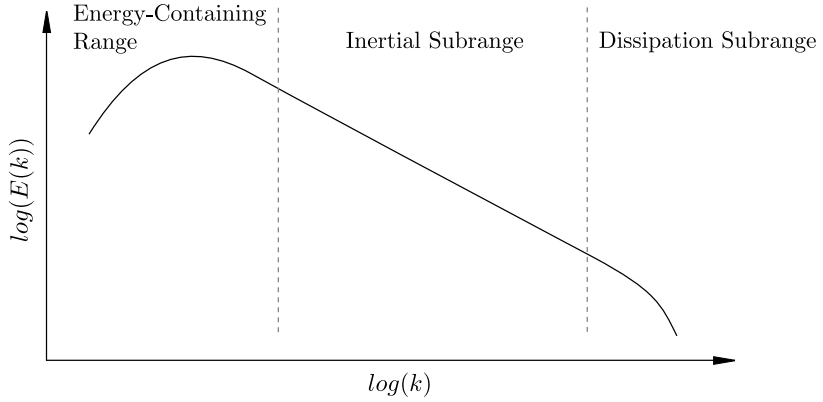

Figure 1.2: Energy spectrum of turbulent flows

turbulent structures requires grids dense enough to resolve the smallest-dissipative Kolmogorov length-scales η_k and time-steps small enough to resolve the Kolmogorov time-scales τ_η that are estimated using:

$$\eta_k = \left(\frac{\nu^3}{\epsilon}\right)^{1/4} \tag{1.1}$$

$$\tau_\eta = \left(\frac{\nu}{\epsilon}\right)^{1/2} \tag{1.2}$$

where ν is the fluid kinematic viscosity and ϵ is the rate of dissipation of turbulent kinetic energy (Pope (2000)). The computational expense of DNS can be approximated as the cube of the Reynolds number based on the energy-containing scales, making DNS highly impractical for engineering applications where the typical Reynolds numbers are commonly larger than $O(10^5)$. Canonical flows at relatively low Reynolds numbers and based on simple geometry can be simulated with DNS to gain an insight into the nature of turbulence and to extract information that may then be used to create turbulence models for lower-fidelity CFD methods.

Turbulence models are used in large-eddy simulations to reduce the number of degrees-of-freedom that must be directly simulated. The large and unsteady features

of turbulent flow are directly resolved, whereas the smallest scales are separated (filtered-out) and modeled using so-called subgrid-scale models (Sagaut (2001)). The large-scale flow features in the energy-containing range are often a function of the geometry of interest and the smallest turbulent features are assumed to be universal at sufficiently high Reynolds numbers and hence they should be easier to model. Unlike the Reynolds-averaged Navier-Stokes approach where the ensemble-averaged mean flow is computed, large-eddy simulations require relatively dense computational grids and time-accurate numerical methods to directly represent the large energy-carrying eddies.

Large-eddy simulations are typically placed between RANS and DNS on the computational expense and accuracy scales (de Villiers (2006)). RANS solvers have been the main numerical simulation tools for engineering problems due to their relatively small computational-cost requirements. However, important flow features such as flow separation, wave breaking, vortex shedding, and turbulence are typically not resolved accurately or at all. The separation of resolved and modeled scales in LES theoretically allows for a much improved representation of these important features that are problem-dependent. Furthermore, the introduction of super-computers and powerful workstations has allowed for LES and its variants (wall-modeled LES, detached eddy simulations) to become attractive alternatives or complements to the RANS tools.

In this work, direct numerical simulations and large-eddy simulations are used to study turbulent-interfacial flows relevant to the marine industry. The DNS data are used for *a priori* analysis of the subgrid-scale terms not resolved in LES in order to understand turbulence in the proximity of a deformable interface. Additionally, the ability of select turbulence models to account for the subgrid effects in turbulent-interfacial flows is examined. The *a priori* analysis is based on two canonical problems: oil and water phase inversion, and a plunging-breaking wave. The relevant

subgrid terms are modeled and assessed *a posteriori* with large-eddy simulations of the two canonical problems. The multiphase LES concept is also extended to the simulation of breaking waves impinging on a vertical circular cylinder to examine the benefits of high-resolution simulations for industrial problems.

In the following sections, Chapter 2 gives an overview of the literature associated with numerical simulation of interfacial marine flows with emphasis on breaking-wave flows. The concept of large-eddy simulations is introduced for single-phase flows and some of the most common turbulence-closure models are discussed. The LES concept is then extended to the governing equations of incompressible multiphase flows and the related literature is summarized. The details of the numerical method are described in Chapter 3 along with the results of direct numerical simulations of the two canonical multiphase flows. Chapter 4 presents the *a posteriori* analysis of the two canonical problems and of breaking-wave impacts on an offshore structure studied with large-eddy simulations. Finally, a summary and conclusions are given and possible future work is proposed in Chapter 5.

CHAPTER 2

Background and Related Work

2.1 Simulation of Interfacial Marine Flows

Numerical simulation of turbulent flows with a deformable fluid interface is a complex problem that is relevant to the marine industry. The interaction of the fluid interface with turbulence has been studied numerically using several different methodologies that are typically problem-dependent. In the marine industry, air and water multiphase problems are the most common, but the interaction of fuel oil and air as well as of liquid natural gas (LNG) and air inside of a ship's storage tanks may also be of interest. Multiphase flows involving the interaction of air and water are especially challenging to simulate because the drastic difference of the phase properties can result in large velocity gradients near the interface and an intricate energy exchange between the two phases. Additionally, Shen and Yue (2001) have demonstrated that near-interface turbulent structures are highly anisotropic and can be responsible for the backscatter of energy that may be on the order of the forward energy cascade in the proximity of the interface. Breaking-water waves are a common example of a turbulent-interfacial flow featuring all of the these characteristics.

Early attempts of simulating breaking waves typically involved modeling of the water phase only. For example, Christensen and Deigaard (2001) describe the free surface and only the water phase using the surface marker method in order to reduce

the computational costs. The simulation of turbulence is based on the large-eddy simulations approach combined with the traditional Smagorinsky model. Some of the important features of spilling and plunging-breaking waves such as the near-interface vortical structures are identified with this approach, but the dissipation of energy through the air cavity entrainment process and backscatter are unaccounted for due to the formulation of the numerical method. Watanabe et al. (2005) also study spilling and plunging breakers using LES of the water phase only and by applying the kinematic and dynamic boundary conditions at the location of the free surface. Surface tension effects and air entrainment are not simulated and the authors focus on the description of the vortical-structures formation process away from the interface.

Several published works focus on the transfer of energy between air and water during the wave-breaking event. In these types of simulations, the numerical treatment of the interface is commonly based on the Eulerian approach that uses a fixed grid and a tracking variable assigned to each grid element. Two popular examples of the Eulerian interface-capturing approach are the volume-of-fluid (VOF) method and the level-set (LS) method. In VOF, each grid element is assigned a value of the phase fraction corresponding to the average proportion of each fluid at that location. The discontinuity of the phase fraction is commonly handled through the simple line interface calculation (SLIC) or the piecewise-linear interface calculation (PLIC) approach used to geometrically reconstruction the interface. The level-set method tracks a signed variable that represents the distance from each cell to the nearest point on the interface and is positive in one phase and negative in the other phase. Both methods rely on an additional advection equation that governs the evolution of the interface. Iafrati (2009) and Iafrati et al. (2012) study two-dimensional water waves with direct numerical simulations and the level-set interface treatment. The dissipation of energy through the breaking process is described in detail for both spilling and plunging breakers in deep water. The early stages of breaking are described well

but the three-dimensional turbulent and interfacial structures present in the latter stages of the flow development cannot be represented on the 2D grids. Zhao et al. (2004) also use two dimensional domains to study wave breaking using VOF and LES where the subgrid behavior is modeled with a multi-scale turbulence closure. The authors report a clear separation between the regions of subgrid-scale turbulent kinetic energy production and dissipation. The lack of local equilibrium during the strong wave-breaking events can be associated with the backscatter of energy near the interface. Additionally, because eddy-viscosity models are formulated on the basis of such a local equilibrium, their application to turbulent-interfacial flows is questionable at best. Two-dimensional waves breaking over a sloping seabed are simulated with LES by Lubin et al. (2011). The authors acknowledge the need for 3D simulations and a sufficient level of spatial resolution to correctly describe the energy transfer process associated with wave breaking. Furthermore, development of a modeling approach to account for the unresolved-interfacial scales is suggested as an important component of the future of multiphase large-eddy simulations.

Lubin et al. (2006) examine three-dimensional plunging-breaking waves with large-eddy simulations and the mixed-scales SGS model. The flow field is initialized with an artificially-steep linear wave that develops in a computational domain with cyclical boundary conditions. The same concept is used by Iafrati (2009) to reduce the computational cost of the simulations. The general features of a plunging breaker are reproduced including the overturning jet and splash-up, and the 3D results indicate an increase in the energy dissipation rate during the breaking process compared to the 2D results. Lakehal and Liovic (2011) study the breaking process along a sloping seabed with LES and a VOF-based method that utilizes a secondary refined grid to capture the evolution of the interface in greater detail. The information from the finer grid is used to form a near-interface damping function to correct the overly-dissipation behavior of the selected eddy-viscosity model. Using spanwise domain

averaging, turbulent kinetic energy of a weak plunging-breaking wave is estimated and found to be not necessarily in equilibrium with the turbulent kinetic energy dissipation. High levels of three-dimensional turbulence are reported in the proximity of the interface during the breaking process.

Numerical study of wave breaking near the shore is important to the understanding of sediment transport along the coast and simulation of open-ocean wave breaking can provide detailed information about the energy exchange process between the atmosphere and large bodies of water. High-resolution numerical simulation of turbulent-interfacial flows is also important to the prediction of breaking-wave impacts on offshore structures because of the highly-nonlinear nature of the problem. de Ridder et al. (2011), Ramirez et al. (2012), and Bredmose et al. (2013) use experimental and numerical analyses to study the response of a bottom-fixed offshore wind turbine impinged upon by regular and irregular seas that include breaking waves. A nonlinear potential flow solver is combined with a Morison-based force estimation in an attempt to numerically replicate the experimental loads on the platform. The authors report good agreement for relatively small-steepness non-breaking impacts, whereas the maximum in-line force on the cylindrical platform due to breaking-wave impacts is significantly under-predicted. The combination of the nonlinear potential flow and the Morison's equation cannot sufficiently account for all the phenomena of plunging breakers that can result in slamming-like impacts. Christensen et al. (2005) use a volume-of-fluid solver to simulate breaking-wave impacts on a vertical-circular cylinder. The loads and wave run-up on the structure are found to be strongly influenced by the type and location of wave breaking which are known to be a function of the air-water interaction. The evolution of the breaking process is further complicated by the close proximity to the seabed and the turbulent energy exchange between the two phases that is typically not accounted for in low-order numerical simulations.

The work presented here expands the field of high-resolution simulations of turbulent-

interfacial marine flows using direct and large-eddy simulations. The use of high-resolution methods is important because these methods can describe the complex interaction between turbulence and the fluid interface in detail and can lead to the formulation of improved turbulence-closure models. The present analysis evaluates the turbulence closure terms in the multiphase large-eddy simulations equations that have been shown to be important in some types of turbulent-interfacial flows. Furthermore, numerical methods readily available for use in complex-industrial large-eddy simulations are selected in order to allow for a straightforward transfer of the present findings to practitioners.

2.2 Overview of Large-Eddy Simulations

The separation of scales at the core of the large-eddy simulations concept is formally achieved through the application of a spatial filter to the governing equations of the flow. The scales present in the flow are separated into resolved scales and unresolved or the so-called subgrid scales. The term "subgrid" is used because the concept of LES is applied on computational domains divided into a matrix (grid) of discrete computational elements that – unlike DNS grids – cannot fully resolve the entire range of turbulent scales. The influence of the subgrid scales is represented by the subgrid-scale (SGS) stress which appears in the filtered momentum equation. This additional unclosed term can be modeled using several approaches commonly divided into the functional and structural types.

In the following sections, the filtering concept is first demonstrated for a single-phase incompressible flow. Different types of interpretation and numerical implementation of LES are also discussed. Several of the most common subgrid-scale stress closure models are then described based on Sagaut (2001) who gives a detailed description of the LES methodology including SGS stress modeling in applications to

incompressible flows.

2.2.1 Filtering of the Governing Equations

The low-pass spatial filtering used to obtain the filtered governing equations is defined as the convolution integral between a filter function G and a generic flow variable ϕ:

$$\overline{\phi}(x,t) = \int G(x-\xi)\phi(\xi,t)\mathrm{d}\xi \tag{2.1}$$

where the over-bar indicates the filtered or resolved variable and the convolution kernel G is associated with a characteristic cutoff length $\overline{\Delta}$. The unresolved component of the generic flow variable is defined as:

$$\phi' = \phi - \overline{\phi}. \tag{2.2}$$

The three most common filters used in large-eddy simulations are the top-hat or box filter, the Gaussian filter, and the spectral or sharp cutoff filter. In application to the Navier-Stokes equations, the selected filter must satisfy linearity, commutation with derivatives, and the preservation of constants (de Villiers (2006)). In spectral space (denoted with a hat), the filter kernel is a function of wave number k and the spatial cutoff length $\overline{\Delta}$ is associated with a cutoff wave number k_c.

For the one-dimensional case, the top-hat filter is defined in physical space using:

$$G(x-\xi) = \begin{cases} 1/\overline{\Delta} & \text{if} \quad |x-\xi| \leq \overline{\Delta}/2 \\ 0 & \text{otherwise,} \end{cases} \tag{2.3}$$

and in spectral space:

$$\hat{G}(k) = \frac{\sin\left(k\overline{\Delta}/2\right)}{k\overline{\Delta}/2}. \tag{2.4}$$

The top-hat filter is commonly used in practical LES applications because it is easy

to implement numerically and the filter-cutoff length-scale is often taken to be proportional to the grid spacing. Additionally, realistic boundary conditions, such as solid walls, can be easily used to bound the computational domain because of the compact support of the filter stencil.

The Gaussian filter is defined as:

$$G(x-\xi) = \left(\frac{C}{\pi\overline{\Delta}^2}\right)^{1/2} \exp\left(\frac{-C|x-\xi|^2}{\overline{\Delta}^2}\right), \tag{2.5}$$

$$\hat{G}(k) = \exp\left(\frac{-\overline{\Delta}^2 k^2}{4C}\right) \tag{2.6}$$

where C is a constant commonly set equal to 6. Chumakov (2005) shows that the Gaussian filter is always positive and it retains the desired shape in spectral space. Such properties are desirable, however, implementing this type of an LES filter in real applications is complicated by the near-boundary behavior associated with the filter's lack of compact support.

The spectral or the sharp cutoff filter is defined using

$$G(x-\xi) = \frac{\sin\left(k_c(x-\xi)\right)}{k_c(x-\xi)} \tag{2.7}$$

in physical space, and with

$$\hat{G}(k) = \begin{cases} 1 & \text{if} \quad |k| \leq k_c \\ 0 & \text{otherwise} \end{cases} \tag{2.8}$$

in spectral space, where the filter retains compact support. The sharp cutoff filter is highly non-local in physical space and hence its implementation is mostly limited to spectral simulations of unbounded flows.

The filtering procedure is illustrated in Figure 2.1 using a one-dimensional ex-

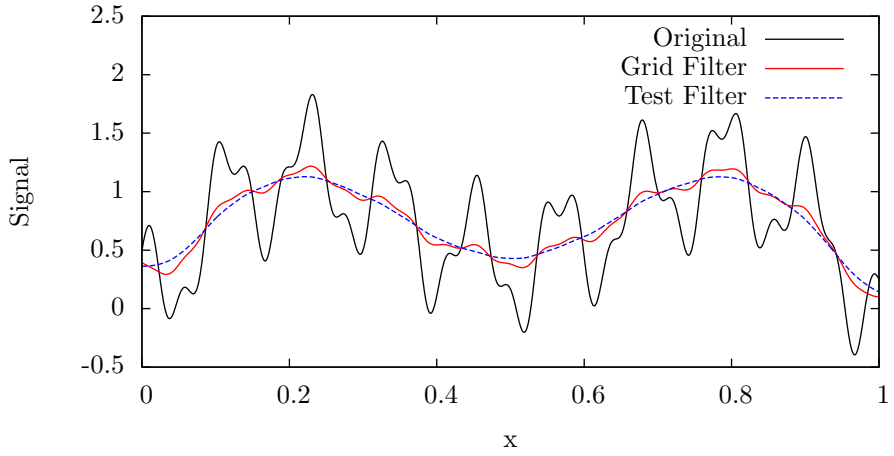

Figure 2.1: Illustration of low-pass filtering in one dimension using a top-hat filter

ample. The high-frequency content of the original signal is filtered out through the application of a "grid-level" filter. The resulting filtered signal is a function of the filter kernel and the associated cutoff length. A secondary "test filter" is commonly used by certain types of SGS models (see Section 2.2.2), where the test-level cutoff length $\widehat{\overline{\Delta}}$ is greater than the grid-level cutoff. Because the ratio of the two cutoff-length scales $\widehat{\overline{\Delta}}/\overline{\Delta}$ is typically greater than one, some of the high-frequency content present in the grid-filtered level is removed to form the test-filtered signal.

The governing equations of large-eddy simulations for an incompressible single-phase flow are obtained by applying the same filtering concept to the Navier-Stokes equations (conservation of mass and fluid momentum), giving:

$$\frac{\partial \overline{u}_i}{\partial x_i} = 0, \tag{2.9}$$

$$\frac{\partial \overline{u}_i}{\partial t} + \frac{\partial \overline{u}_i \overline{u}_j}{\partial x_j} = -\frac{1}{\rho}\frac{\partial \overline{p}}{\partial x_i} + \frac{\partial}{\partial x_j}\left(\nu\left(\frac{\partial \overline{u}_i}{\partial x_j} + \frac{\partial \overline{u}_j}{\partial x_i}\right) - \tau_{ij}\right), \tag{2.10}$$

where the over-bars represent the resolved quantities and $\overline{u}_i$ is the velocity vector, $\overline{p}$ is the fluid pressure, ρ is the fluid density, ν is the kinematic fluid viscosity, and τ_{ij} is the subgrid-scale stress tensor. The influence of the subgrid scales is grouped into

τ_{ij} which is defined as

$$\tau_{ij} = \overline{u_i u_j} - \overline{u}_i \overline{u}_j, \tag{2.11}$$

based on the decomposition of the nonlinear convective term:

$$\overline{u_i u_j} = \overline{u}_i \overline{u}_j + \tau_{ij}. \tag{2.12}$$

The SGS stress can be further decomposed using the resolved and subgrid quantities following Germano (1986):

$$\tau_{ij} = L_{ij} + C_{ij} + R_{ij}, \tag{2.13}$$

where

$$L_{ij} = \overline{\overline{u}_i \overline{u}_j} - \overline{\overline{u}}_i \overline{\overline{u}}_j, \tag{2.14}$$

$$C_{ij} = \overline{\overline{u}_i u'_j} + \overline{\overline{u}_j u'_i} - \overline{\overline{u}}_i \overline{u'_j} - \overline{\overline{u}}_j \overline{u'_i}, \tag{2.15}$$

$$R_{ij} = \overline{u'_i u'_j} - \overline{u'_j u'_j} \tag{2.16}$$

are the modified Leonard stress tensor, modified cross-stress tensor, and the modified Reynolds subgrid tensor, respectively. The modification presented by Germano (1986) ensures that all three components of the SGS stress are Galilean-invariant. The Leonard stress represents the interaction of the resolved scales, the cross-stress is responsible for the interaction between the resolved and the unresolved scales, and the Reynolds subgrid tensor describes the interaction of the subgrid scales. Certain SGS models attempt to approximate the indivdual components using information from the resolved flow (structural type), whereas other types of SGS models approximate the influence of the entire unclosed term (functional type; see Section 2.2.2 for details of both modeling approaches).

Several different interpretations and practical implementations of the LES con-

cepts can be found in the literature as discussed by Sagaut (2001). The different methodologies stem from the lack of a consensus on the best-practice guidelines, as well as from the assumptions and generalizations that are often necessary in practice to overcome limited computational resources and implementation challenges.

In what is termed the explicit-filtering approach, the filters described above are applied explicitly on the numerical grid, resulting in the separation of the resolved scales, subfilter scales, and the subgrid scales. The filter width is selected to be greater than the grid spacing to allow for an explicit calculation of the filtered quantities based on the flow information available on the grid level. The scales that cannot be resolved on the grid due to the limitation of the spatial discretization are represented by the subgrid-scale stress. This approach is appealing because it can theoretically separate the influence of the discretization error from the solution approach and because the explicit application of a filter follows directly from the theoretical formulation of the LES concept. However, the benefits of explicit LES are unclear in practice. The grid-level filtering procedure adds an additional computational cost to what are typically already very expensive computations, and the explicit filtering has been shown to not guarantee an improvement in the accuracy of the solution. The fully-developed turbulent channel flow study of Gullbrand and Chow (2003) indicates that a sufficient grid resolution and an appropriate selection of the SGS model may have a greater influence on the quality of the solution.

A common alternative to the explicit-filtering approach is referred to as the implicit-filtering approach, or as the traditional LES solution method in Gullbrand and Chow (2003). The numerical discretization used to compute the flow solution is interpreted as an effective low-pass filter and no explicit grid-level filtering is used. The only filtering that may be applied is used in the calculation of the subgrid-scale stress model terms such as in the case of a dynamic Smagorinsky model. This method is commonly found in applications of LES to flows with real-complex geometries and

in industrial settings where limited computational resources are available and rapid turn-around times are necessary. The implicit-filtering method should not be confused with "no-model" LES or the Monotone Integrated Large-Eddy Simulation (MILES) in the compressible-flow case where the effective dissipation of high-order upwind schemes is used exclusively to account for the SGS effects (Fureby (2007)).

In the large-eddy simulations presented in Chapter 4, the implicit-filtering method is used. Explicit test-level filtering is utilized to model the subgrid-scale behavior based on the resolved-flow information.

2.2.2 Subgrid-Scale Stress Closure Models

The role of the subgrid-scale stress model is to account for the effects of the unresolved scales, including the forward and backward energy cascade process. Most models are categorized as either structural or functional. Structural models (scale-similarity based) attempt to represent the stress tensor based on the resolved scales, whereas functional models (eddy-viscosity based) approximate the actual contribution of the subgrid scales in the momentum equation.

Smagorinsky Model

The simplest SGS stress modeling is based on the eddy-viscosity approach where the model acts to functionally represent the forward energy cascade necessary to drain energy from the resolved scales into the subgrid range. The behavior of the smallest dissipative scales typically not resolved in LES is modeled using the eddy-viscosity hypothesis (de Villiers (2006)). The model based on the original work of Smagorinsky (1963) is the best-known model of this type. The deviatoric part of τ_{ij} is related to the resolved rate-of-strain tensor $\overline{S}_{ij}$ by:

$$\tau_{ij} - \frac{1}{3}\tau_{ii}\delta_{ij} = \tau_{ij}{}^{d} = -2\nu_{\text{sgs}}\overline{S}_{ij} = -\nu_{\text{sgs}}\left(\frac{\partial \overline{u}_i}{\partial x_j} + \frac{\partial \overline{u}_j}{\partial x_i}\right) \tag{2.17}$$

where

$$\overline{S}_{ij} = \frac{1}{2}\left(\frac{\partial \overline{u}_i}{\partial x_j} + \frac{\partial \overline{u}_j}{\partial x_i}\right). \tag{2.18}$$

The eddy-viscosity coefficient ν_{sgs} is obtained through the mixing-length hypothesis relating characteristic length and time-scales:

$$\nu_{\text{sgs}} = C_s \overline{\Delta}^2 |\overline{S}| \tag{2.19}$$

The magnitude of the resolved rate-of-strain tensor is defined by $|\overline{S}| \equiv (2\overline{S}_{ij}\overline{S}_{ij})^{1/2}$, C_s is the Smagorinsky constant, and $\overline{\Delta}$ is the characteristic filter width commonly taken as $\overline{\Delta} = (\Delta x \Delta y \Delta z)^{1/3}$ or the cube-root of the cell volume. The Smagorinsky constant has been determined for several canonical flows but no universal constant has been found. Additionally, the model is overly dissipative in regions of laminar or high shear flow. A popular ad-hock solution to the near-wall behavior is the van Driest damping function which acts to reduce the eddy-viscosity near the solid boundaries.

A priori studies have shown that the Smagorinsky type of SGS modeling can exhibit relatively poor correlation with the actual turbulent-stress behaviour due to the lack of aligment between the deviatoric SGS stresses and the resolved strain-rate tensor as discussed by Vreman et al. (1995). The purely-dissipative nature of the Smagorinsky model also does not allow for the reverse transfer of energy (backscatter) from the small scales to the larger scales. These characteristics render the constant-coefficient form of the eddy-viscosity approach questionable for multiphase simulations where the importance of backscatter and correct modeling of the turbulent stress behaviour have been demonstrated (Chesnel et al. (2011a); Labourasse et al. (2007)).

Dynamic Smagorinsky Model

A dynamic procedure proposed by Germano et al. (1991) improves on the original Smagorinsky model by determining the Smagorinsky coefficient as a function of time

and space. A secondary test filter, larger than the grid filter and commonly taken as $\widehat{\overline{\Delta}}/\overline{\Delta} = 2$, is used to extract information from the resolved scales close to the grid-filter cutoff. The grid-filtered Navier-Stokes equations are test-filtered (denoted with the top-hat symbol) to yield a new subtest stress tensor T_{ij}:

$$T_{ij} = \widehat{\overline{u_i u_j}} - \widehat{\overline{u}}_i \widehat{\overline{u}}_j \tag{2.20}$$

that can be related to the subgrid stress and the resolved stress tensor L_{ij} through the Germano identity:

$$L_{ij} = \widehat{\overline{u_i}\overline{u_j}} - \widehat{\overline{u}}_i \widehat{\overline{u}}_j = T_{ij} - \widehat{\tau}_{ij}. \tag{2.21}$$

Both the subtest and the subgrid stresses can be represented by a general eddy-viscosity form with the same unknown coefficient C_d:

$$\tau_{ij} - \frac{1}{3}\tau_{kk}\delta_{ij} = C_d \left(-2\overline{\Delta}^2 \left|\overline{S}\right| \overline{S}_{ij} \right) = C_d \beta_{ij} \tag{2.22}$$

$$T_{ij} - \frac{1}{3}T_{kk}\delta_{ij} = C_d \left(-2\widehat{\overline{\Delta}}^2 \left|\widehat{\overline{S}}\right| \widehat{\overline{S}}_{ij} \right) = C_d \psi_{ij} \tag{2.23}$$

The system is over-determined because there are five independent equations and a single unknown. A least-squares error minimization was proposed by Lilly (1992) to find an appropriate eddy-viscosity coefficient where the error E_{ij} is minimized:

$$E_{ij} = L_{ij} - \frac{1}{3}L_{kk}\delta_{ij} - C_d\psi_{ij} + C_d\widehat{\beta}_{ij} \tag{2.24}$$

and the dynamic coefficient is removed from the test-filtering operation in the last term on the right-hand side through the assumption of C_d being constant over an interval on the order of the test filter length. The coefficient is then obtained from:

$$C_d = \frac{m_{ij}L^d_{ij}}{m_{kl}m_{kl}} \tag{2.25}$$

and

$$m_{ij} = \psi_{ij} - \widehat{\beta}_{ij}. \tag{2.26}$$

In this formulation the coefficient can become negative to approximate the action of backscatter, or zero in regions of laminar flow. However, the dynamic procedure can result in numerical instabilities and hence it usually requires some form of coefficient averaging or an ad hoc clipping of the effective viscosity $\nu_{\text{eff}} = \nu + \nu_{\text{sgs}}$. For example, the denominator and numerator can be averaged individually to give:

$$C_d = \frac{\langle m_{ij} L_{ij}^d \rangle}{\langle m_{kl} m_{kl} \rangle} \tag{2.27}$$

where the averaging is typically performed over homogeneous directions. Most flows found in practice do not contain any easily identified homogeneous directions. Some practitioners choose to average the coefficient locally among neighboring cells or over the entire computational domain, effectively making the dynamic coefficient a function of time only. Another alternative is to compute the time-averaged coefficient along the pathlines that form in the flow. This so-called Lagrangian model of Meneveau et al. (1996) utilizes a weighting function to balance the impact of the coefficients computed in the past with the current-time coefficients. Meneveau and Katz (2000) report that the model has been successfully used in non-equilibrium and reacting flows, but the user must specify a time-scale parameter that may require tuning for the individual flows of interest.

One-Equation Model

Transport-equation based LES models attempt to further improve the subgrid modeling by incorporating non-local and memory effects of the subgrid terms. The one-equation model and its dynamic variant introduced by Kim and Menon (1995) relate

the turbulent viscosity to the subgrid turbulent kinetic energy by:

$$\nu_{\text{sgs}} = C_k \overline{\Delta} k_{\text{sgs}}^{1/2}. \tag{2.28}$$

A transport equation for k_{sgs} is constructed and takes the form:

$$\frac{\partial k_{\text{sgs}}}{\partial t} + \frac{\partial \overline{u}_j k_{\text{sgs}}}{\partial x_j} = -\tau_{ij}\frac{\partial \overline{u}_i}{\partial x_j} - C_\epsilon \frac{k_{\text{sgs}}^{3/2}}{\overline{\Delta}} + \frac{\partial}{\partial x_j}\left(\nu_{\text{sgs}}\frac{\partial k_{\text{sgs}}}{\partial x_j}\right) \tag{2.29}$$

where the first term on the right-hand side is the production term. The dissipation term follows and its coefficient C_ϵ together with C_k can be determined dynamically based on the Germano identity previously discussed in the case of the dynamic Smagorinsky model (Equation 2.21). An approximation of backscatter is possible without the numerical stability issues often found in the original Smagorinsky models because of the implemented limiting mechanisms (Carati et al. (1995)). The additional transport-equation and the dynamic procedure required to compute the model's coefficients make this form of LES modeling more computationally expensive. Carati et al. (1995) has shown that the dynamic one-equation model requires approximately 70% more computational overhead than the original constant-coefficient Smagorinsky model for simulations of isotropic turbulence decay and forced turbulence.

Scale-Similarity Models

Bardina et al. (1980) proposed the scale-similarity model in which the modeled subgrid terms are computed from the smallest resolved scales. This form of structural LES turbulence modeling is based on the conjecture that the SGS stresses are correlated with the Reynolds stresses due to the smallest resolved scales (Sarghini et al. (1999)). A secondary grid-level filtering operation is performed to obtain the subgrid stress term of the form:

$$\tau_{ij} = \overline{\overline{u}_i \overline{u}_j} - \overline{\overline{u}}_i \overline{\overline{u}}_j \tag{2.30}$$

which corresponds to the modified Leonard stress and is expressed in terms of the resolved quantities only. *A priori* studies of Bardina et al. (1980) and others have shown excellent correlation between the similarity-modeled SGS stress and the true SGS stress computed from DNS data of homoegenous isotropic turbulence and shear turbulent flows. The backscatter of energy is accounted for in a stable manner using this formulation but because the pure scale-similarity model is not dissipative in nature, it is often found to lack sufficient dissipation in the subgrid regime (Zang et al. (1993)).

A generalized version of the scale-similarity model formulated by Liu et al. (1994) (stress-similarity or the Liu-Meneveau-Katz model) uses a secondary cutoff length in the form of a larger test filter:

$$\tau_{ij} = C\left(\widehat{\overline{u}_i\overline{u}_j} - \widehat{\overline{u}}_i\widehat{\overline{u}}_j\right) \tag{2.31}$$

to utilize the grid-resolved information available in the so-called window stress between $\widehat{\overline{\Delta}}$ and $\overline{\Delta}$ cutoff lengths. The constant C can be determined from *a priori* analysis or dynamically by employing a third filter operating at a cutoff length greater than the test-filter cutoff. In the open-turbulent jet experiments of Liu et al. (1994), the coefficient was found to vary between approximately 0.3 and 0.6, whereas other practitioners have found the coefficient to be approximately 1.0 for several canonical flows. Cook (1997) studied the behavior of the stress-similarity coefficient as a function of several simulation parameters: filter ratio $\widehat{\overline{\Delta}}/\overline{\Delta}$, turbulent Reynolds number Re_l, and the level of resolution of the large eddies $l/\overline{\Delta}$. The coefficient is found to be a weak function of all the tested parameters, especially at high Reynolds numbers ($Re_l > 10^5$).

A component of the true SGS stress computed from the experimental data of Liu et al. (1994) and the modeled equivalent using the Smagorinsky model and the

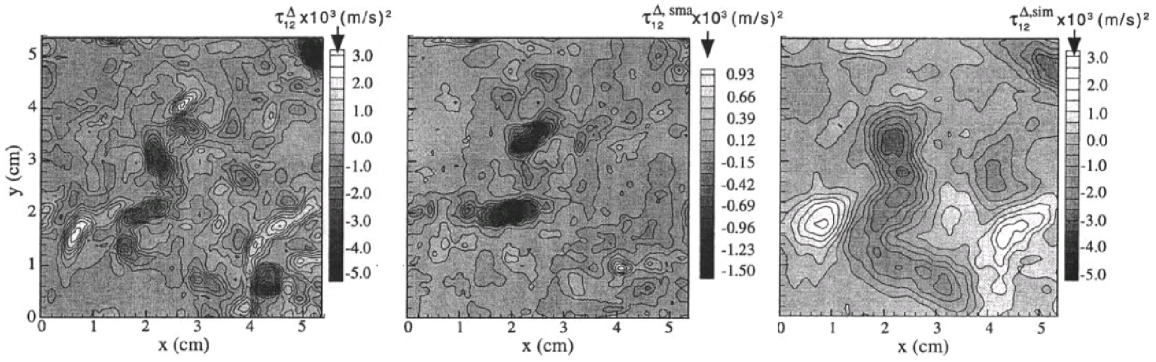

Figure 2.2: True SGS stress (far left) in an open-jet flow compared to the modeled stress using the Smagorinsky model (middle) and the stress-similarity (far right) models. Reprinted based on Meneveau and Katz (2000) and Liu et al. (1994).

stress-similarity model are shown in Figure 2.2. The stress-similarity model is found to reproduce the magnitude of the subgrid stress and to better represent the overall spatial distribution of the main turbulent features. However, the secondary test-level filter that is twice the size of the grid-level filter effectively smears away the detail of the smallest turbulent scales.

Mixed Models

Similarity-based models can be combined with eddy-viscosity models to improve the dissipative behavior, forming a general mixed model of the form:

$$\tau_{ij} - \frac{1}{3}\tau_{kk}\delta_{ij} = -2\nu_{\text{sgs}}\overline{S}_{ij} + L_{ij} - \frac{1}{3}L_{kk}\delta_{ij}. \tag{2.32}$$

The dynamic procedure for the determination of the coefficient C_d used to compute the eddy-viscosity component is popular for non-equilibrium flows because this type of procedure allows for the adaptation of the coefficients to the local flow. The Germano identity is used as in the case of the dynamic eddy-viscosity model to relate the subtest and subgrid stresses to the resolved window stresses. A least-squares approach is then used to calculate the coefficient as a function of space and time.

Additionally, a third filter-cutoff length-scale can be utilized to dynamically compute the coefficient for the similarity contribution, resulting in the so-called dynamic two parameter model of Salvetti and Banerjee (1995).

Mixed models have been found to improve on the correlation between the modeled SGS stresses and the true SGS stresses compared to the original Smagorinsky model because the eddy-viscosity contribution is typically much smaller compared to the scale-similarity term. *A priori* testing of DNS data for spray atomization flows by Chesnel et al. (2011a) showed a significant improvement in the correlation coefficient between the modeled and true SGS stresses and the author also acknowledged the mixed model as the most promising approach to future multiphase large-eddy simulations.

Evaluating Model Performance

Two methods of SGS model evaluation are commonly used in practice: *a priori* and a posteriori studies. In the *a priori* analysis, direct numerical simulations or experimental measurements are used as the exact solution to the flow of interest. Because the experimental data set is a direct representation of the real flow and the DNS data is considered to be fully resolved across all the scales of turbulence, the resolved and subgrid quantities are computed freely. Liu et al. (1994) outlines the *a priori* procedure conducted for experimental measurements of an open jet at a relatively high Reynolds number. The consistency of the procedure is emphasized to ensure that when computing the flow quantities for the analysis of the large-eddy simulations models, only the information available at the LES grid level is used. This entails explicit filtering of the experimental data and sampling it onto the effective LES grid that is coarser than the spatial resolution of the experiments. The true subgrid-scale stress can then be compared to the modeled stress at the locations of the LES grid points without the influence of additional information that is not available

during the execution of large-eddy simulations. The same procedure has been applied to *a priori* studies of various flows resolved with direct numerical simulations (see for example Vreman et al. (1995), Chesnel et al. (2011a)).

The *a priori* analysis is useful for a direct comparison of the true SGS stress and the modeled SGS stress, but because the flow quantities that are used originate from either DNS or experiments, the effects of numerical error that is inherent to LES solutions is not taken into account. The a posteriori method includes the numerical error effects into the evaluation of the SGS models by comparing the results of actual large-eddy simulations against reference data. The difficulty of this method stems from a large number of factors that may affect the LES results and that may be beyond the control of the practitioner. The approach used in this work is to use both the *a priori* (Chapter 3) and the a posteriori (Chapter 4) analyses to study the nature of the subgrid terms and to evaluate the subgrid-scale models of interest based on two canonical turbulent-interfacial flows.

2.3 Large-Eddy Simulations of Interfacial Flows

The filtering concept is now extended to the governing equations of multiphase flow. Two incompressible and immiscible fluids separated by a deformable interface can be simulated numerically based on the formulation of Scardovelli and Zaleski (1999). In this so-called one-fluid formulation, a single set of governing equations (here also referred to as the multiphase equations) describes the entire computational domain and the behavior of the fluid interface is captured by an additional equation. The governing equations are filtered and the relative magnitudes of the resulting subgrid-scale stresses are discussed based on published *a priori* studies of relavent turbulent-interfacial flows.

2.3.1 Governing Equations

The general form of the multiphase equations including gravitational and viscous forces can be formulated as:

$$\frac{\partial u_i}{\partial x_i} = 0 \tag{2.33}$$

$$\frac{\partial \rho u_i}{\partial t} + \frac{\partial \rho u_i u_j}{\partial x_j} = -\frac{\partial p}{\partial x_i} + \rho g_i + \frac{\partial}{\partial x_j}\left(\mu\left(\frac{\partial u_i}{\partial x_j} + \frac{\partial u_j}{\partial x_i}\right)\right) - S(x_i, t). \tag{2.34}$$

The equations include the conservation of mass and momentum with a generic source term $S(x_i, t)$. The general form of the interface equation for interface-capturing methods applied to incompressible flows can be formulated as:

$$\frac{\partial \alpha}{\partial t} + \frac{\partial u_i \alpha}{\partial x_i} = 0. \tag{2.35}$$

The fluid properties are defined everywhere in the domain using the phase-indicator variable α that is represented by the volume fraction in the volume-of-fluid (VOF) method and the regularized characteristic function in the conservative level-set (CLS) method that is adapted in this work. The fluid density and viscosity is defined everywhere in the domain using:

$$\rho(x_i) = \rho_w \alpha(x_i) + \rho_a \left(1 - \alpha(x_i)\right), \tag{2.36}$$

$$\mu(x_i) = \mu_w \alpha(x_i) + \mu_a \left(1 - \alpha(x_i)\right). \tag{2.37}$$

In simulations of air and water, $\alpha = 0$ corresponds to a computational cell occupied by air and $\alpha = 1$ indicates a computational cell occupied by water. The interface between the two fluids is a thin smoothly-varying region referred to as the diffuse interface and the nominal free surface is found where $\alpha = 0.5$. The continuum surface force (CSF) model of Brackbill et al. (1992) is adapted in the present work to include the effects of surface tension. A continuous volumetric force is introduced into the momentum

equation to model surface tension acting within the diffuse interface (Rusche (2002)).

Following the single-phase derivation presented in Section 2.2.1, the generalized governing equations are filtered to yield:

$$\frac{\partial \overline{u}_i}{\partial x_i} = 0, \tag{2.38}$$

$$\frac{\partial \overline{\rho u_i}}{\partial t} + \frac{\partial \overline{\rho u_i u_j}}{\partial x_j} = -\frac{\partial \overline{p}}{\partial x_i} + \overline{\rho g_i} + \frac{\partial}{\partial x_j}\overline{\left(\mu\left(\frac{\partial u_i}{\partial x_j} + \frac{\partial u_j}{\partial x_i}\right)\right)} - \overline{\gamma\kappa\frac{\partial \alpha}{\partial x_i}} \tag{2.39}$$

for the conservation of fluid mass and momentum in the one-fluid formulation. The last term of the right-hand side of Equation 2.39 is the continuum surface force model for surface tension where γ is the surface tension coefficient, and κ is the surface curvature. The interface-advection equation is also filtered resulting in:

$$\frac{\partial \overline{\alpha}}{\partial t} + \frac{\partial \overline{u_i \alpha}}{\partial x_i} = 0. \tag{2.40}$$

The low-pass filtering operation commutes with the derivative operator and constants that are not a function of the spatial coordinates are unaffected. The nonlinear terms that depend on the unresolved scales are decomposed using the generalized form of Equation 2.12 to give the following set of governing equations:

$$\frac{\partial \overline{\rho}\,\overline{u}_i}{\partial t} + \frac{\partial \overline{\rho}\,\overline{u}_i\overline{u}_j}{\partial x_j} = -\frac{\partial \overline{p}}{\partial x_i} + \overline{\rho} g_i + \frac{\partial}{\partial x_j}\left(\overline{\mu}\left(\frac{\partial \overline{u}_i}{\partial x_j} + \frac{\partial \overline{u}_j}{\partial x_i}\right)\right) - \frac{\partial \tau_{Ai}}{\partial t} - \frac{\partial \tau_{Cij}}{\partial x_j} - \frac{\partial \tau_{Dij}}{\partial x_j} - \tau_{STi} \tag{2.41}$$

$$\frac{\partial \overline{\alpha}}{\partial t} + \frac{\partial \overline{u}_i\overline{\alpha}}{\partial x_i} = -\frac{\partial \tau_{Ii}}{\partial x_i} \tag{2.42}$$

$$\tag{2.43}$$

The influence of the unresolved scales is grouped into four subgrid-scale terms in the

filtered momentum equation and into one SGS term in the filtered interface equation:

$$\tau_{Ai} = \overline{\rho u_i} - \overline{\rho}\,\overline{u}_i \tag{2.44}$$

$$\tau_{Cij} = \overline{\rho u_i u_j} - \overline{\rho}\,\overline{u}_i\overline{u}_j \tag{2.45}$$

$$\tau_{Dij} = \overline{\mu\left(\frac{\partial u_i}{\partial x_i} + \frac{\partial u_j}{\partial x_i}\right)} - \overline{\mu}\left(\frac{\partial \overline{u}_i}{\partial x_j} + \frac{\partial \overline{u}_j}{\partial x_i}\right) \tag{2.46}$$

$$\tau_{STi} = \overline{\gamma\kappa\frac{\partial \alpha}{\partial x_i}} \tag{2.47}$$

$$\tau_{Ii} = \overline{u_i\alpha} - \overline{u}_i\overline{\alpha} \tag{2.48}$$

The five terms are referred to as the acceleration, convective, diffusive, surface tension, and interfacial subgrid-scale terms, respectively. The convective term is found in the single-phase LES equations, whereas the other terms are related to the presence of the fluid interface (Labourasse et al. (2007), Chesnel et al. (2011a)).

The application of the spatial filter across the finite thickness of the interface has the side-effect of introducing the new subgrid terms in the single-fluid equations. The effects of the additional subgrid terms are a function of the interface thickness. In order to avoid filtering across the interface, the filter size must diminish in the interface region, or in the case of the implicit filtering, the grid size near the interface must be infinitesimally small. However, because the approximation of the interface using the diffuse-interface approach and implicit filtering are common in engineering applications, it is important to understand the impact of the additional terms using grid refinement levels that are used in practice.

In applications to compressible flow, the Navier-Stokes equations are commonly Favre-averaged to reduce the number of subgrid terms in the filtered equations. The

Favre-averaged generic flow variable is obtained from:

$$\widetilde{\phi} = \frac{\overline{\rho\phi}}{\overline{\rho}}. \tag{2.49}$$

The correlation between the variable-fluid density ρ and the flow variable ϕ is removed using the Favre-average and hence the acceleration SGS term τ_A is eliminated. In the present work, the Favre-average is not used because when both phases are incompressible the application of the Favre operation yields a source term in the conservation of mass equation (see Toutant et al. (2009), Chesnel et al. (2011a), Labourasse et al. (2007) for details). The additional source term is not trivial to handle numerically and the added difficulty of its implementation at least partially outweighs the benefits of reducing the number of SGS terms. Additionally, as will be shown in the *a priori* study of Chapter 3, the acceleration term that is eliminated by the Favre-average is found to be several orders of magnitude smaller than the other SGS terms for the two flows studied.

2.3.2 Role of Subgrid Scales

Several recently published works have investigated the subgrid-scale terms present in the multiphase LES equations. Lakehal and Liovic (2011) note that the choice to either model or neglect the SGS terms should be made based on a thorough study of their relative importance. Such studies have been conducted for relatively simple turbulent-interfacial flows to allow for the use of direct numerical simulations and the *a priori* analysis. The magnitudes of the SGS terms are quantified using the filtered DNS data and compared to the resolved terms to determine the amount of information that would typically be not resolved through large-eddy simulations of the same flows.

The problem of oil-water phase inversion in a closed box is examined by Labourasse

et al. (2007), Vincent et al. (2008), and Larocque et al. (2010). The same flow is also studied in the present work. Labourasse et al. (2007) use a two-dimensional 512^2 cell grid together with the piecewise-linear interface calculation (VOF-PLIC) method and hybrid center-upwind discretization schemes. The *a priori* analysis uses a top-hat filter with four different stencil sizes. A comparison is also made between the results obtained with and without Favre-averaging of the governing equations. The authors report that the subgrid behavior of the flow cannot be fully represented with modeling of the convective term only. The convective term is found to be the largest contributor relative to the resolved quantities, but the magnitudes of the diffusive and surface-tension SGS terms change rapidly as the filter size is modified. The Favre-filtered version of the governing equations is recommended for use in LES because the results with this approach were found to be less diffusive and hence possibly easier to correct for with the addition of eddy-viscosity models. However, the implementation of the source term in the continuity equation that is due to Favre-averaging is not taken into account. The benefits of the mixed model for the convective term are also reported in comparison to pure eddy-viscosity models.

Vincent et al. (2008) and Larocque et al. (2010) study the phase inversion problem using three-dimensional grids with 128^3 elements and two sizes of the top-hat filter. Favre-averaging is used in both works to eliminate the acceleration SGS term. The relative magnitude of the remaining SGS terms is examined as a function of the fluid density and viscosity ratios. The Reynolds number in water is varied between 1×10^4 and 5.54×10^5, and the Weber number is varied between 26 and 1.3×10^4. In this parametric study, Larocque et al. (2010) find the magnitude of the convective SGS term to be approximately 25% of the resolved counterpart. The subgrid interfacial term τ_I is found to be on the order of the resolved component, and the authors state that τ_C and τ_I should be the focus of SGS modeling in large-eddy simulations of similar turbulent-interfacial flows. The relative order of the SGS term contributions

is unaffected by the adjustment of the non-dimensional flow parameters.

Chesnel et al. (2011a) conduct direct numerical simulations of spray atomization to study the hierarchy of the subgrid terms present in the multiphase formulation. The simulations are conducted on a grid with approximately 134 million cells and the ghost fluid method is coupled with a VOF/LS approach to preserve the sharp fluid interface. *A priori* analysis indicates that the evolution of the fluid interface is heavily influenced by the subgrid behavior. The stress-similarity model was found to exhibit an excellent correlation between the true and modeled subgrid interfacial contribution. However, the coefficient of the model was adjusted based on the filter-size ratio using the DNS results. A procedure for calculating the coefficient dynamically is indicated as the optimal solution for the application of the stress-similarity model in practical multiphase LES. The authors report that the convective SGS stress cannot be successfully modeled with a pure eddy-viscosity concept when a fluid interface is present. The poor performance of the eddy-viscosity model is associated with the formation of strong velocity gradients caused by the presence of the interface rather than turbulent motion. The mixed modeling concept shows a much improved correlation with the true SGS stress compared to the dynamic Smagorinsky model.

The current work utilizes similar analyses based on highly-resolved numerical simulations to study the subgrid behavior in turbulent-interfacial flows relevant to the marine industry. *A priori* analysis of the LES subgrid-scale terms is carried out to determine their relative importance in incompressible multiphase flows using DNS data for two canonical problems: oil and water phase inversion, and a plunging-breaking wave. The performance of select turbulence models in multiphase applications involving a deformable interface is examined using the DNS data. The relevant subgrid terms are then modeled and assessed *a posteriori* with large-eddy simulations of the two canonical problems. The additional subgrid terms are modeled with the stress-similarity concept that is implemented into the LES solver. Additionally, the multi-

phase large-eddy simulations concept is extended to an industrial problem involving breaking waves impinging on a vertical circular cylinder. The effects of the subgrid modeling on the ability to predict the force on the cylinder and the free-surface elevation profiles are investigated, and the contributions of the subgrid terms due to the presence of the interface are examined.

CHAPTER 3

Direct Numerical Simulations of Canonical Interfacial Flows

In this chapter, highly-resolved numerical simulations are used to study two types of turbulent-interfacial flows. The generated data is used for *a priori* analysis of the various subgrid-scale terms present in the grid-filtered governing equations, and for the analysis of several commonly used subgrid-scale modeling approaches.

First, the problem of two fluids interacting inside of a closed two-dimensional domain is examined. This phase-inversion problem involves a complex interaction of a wide range of turbulent and interfacial scales that are resolved on a fine numerical grid. The turbulent and interfacial structures present in this canonical flow are of interest because they are directly related to the types of turbulent and interfacial structures found in marine flows with breaking waves. The problem setup allows for the use of a trivial domain geometry, high-accuracy uniform numerical grids and discretization schemes. The second canonical flow study involves a three-dimensional plunging-breaking wave. Uniform grids and high-accuracy discretization schemes are also used here to simulate the breaking process of a steep water wave.

An overview of the numerical method employed in this work is presented first. The sections that follow introduce the two canonical flows and present the details of grid convergence studies that are conducted to ensure an adequate resolution of the turbulent and interfacial scales of interest. The subgrid-scale terms identified in

Chapter 2 are then quantified and examined for their relative importance. The results of the two *a priori* studies are used in Chapter 4 to carry out large-eddy simulations of the two turbulent-interfacial flows.

3.1 Numerical Method

The numerical simulations performed in this work utilize the OpenFOAM open-source toolkit that consists of a large set of numerical solvers and discretization schemes commonly used to numerically solve partial differential equations that govern fluid flow. The standard set of C++ libraries can be easily modified and extended to include new turbulence models, treatments of the fluid interface, solution algorithms, etc. The capabilities of OpenFOAM to simulate single and multiphase flows have been studied and validated by a large community of developers, researchers, and practitioners across many industries.

The computational domain is decomposed into a set of control volumes (computational cells) and the governing equations are discretized based on the finite-volume method (FVM, see Ferziger and Perić (1996) for details). Because the OpenFOAM toolkit is three-dimensional in nature, two-dimensional grids are one-cell thick and use special boundary conditions to eliminate the influence of the third dimension. The governing equations of the fluid flow, such as those presented in Sections 2.2.1 and 2.3.1, contain spatial terms that are discretized based on the generalized form of Gauss' theorem (see for example Damian (2012)). The temporal terms of the governing equations can be handled with explicit or implicit methods. The flow variables are stored at the cell centers in a co-located arrangement and the system of equations is solved in a segregated approach. Jasak (1996) provides a detailed description of the general discretization and solution methodology.

3.1.1 Solution Procedure

The solution to the discretized incompressible Navier-Stokes equations is computed using the classical PISO (Pressure Implicit with Splitting of Operators) algorithm where the momentum predictor and corrector steps handle the pressure-velocity coupling (Issa (1986)). The fluid-interface equation is solved with the conservative level-set method (CLS) of Olsson and Kreiss (2005) and Olsson et al. (2007). In this method, the mass-conserving properties of the volume-of-fluid formulation are combined with the benefits of the level-set approach including the smooth transition of the fluid properties across the interface region of constant width. The regularized characteristic function α varies from 0 to 1 across the interface thickness defined by the hyperbolic tangent function and the nominal interface is defined where $\alpha = 0.5$. The process of advecting the characteristic function is completed in two steps that involve solving a set of partial differential equations:

$$\frac{\partial \alpha}{\partial t} + \frac{\partial u_i \alpha}{\partial x_i} = 0, \tag{3.1}$$

$$\frac{\partial \alpha}{\partial \tau} + \frac{\partial}{\partial x_i}\left(\alpha\left(1-\alpha\right) n_i\right) = \varepsilon \frac{\partial}{\partial x_i}\left(\left(\frac{\partial \alpha n_i}{\partial x_i}\right) n_i\right). \tag{3.2}$$

The first equation corresponds to the interface-advection equation presented in Section 2.3.1. The steady-state solution of Equation 3.2 is obtained between each time step to preserve the desired interface thickness and is referred to as the reinitialization step. The constant ε is proportional to the thickness of the diffuse interface and its value is selected at run-time. The vector normal to the fluid interface n_i is found using:

$$n_i = \frac{\partial \alpha}{\partial x_i}\left|\frac{\partial \alpha}{\partial x_i}\right|^{-1}. \tag{3.3}$$

The CLS method has been validated for both convergence and mass-conservation properties using several canonical interfacial-flow problems including falling droplets,

raising air bubbles, vortex and rotating circle tests.

The two flows studied in this chapter use simple domain geometries that are discretized using uniformly-spaced hexahedral cells with an aspect ratio of one. The quality of these grids allows for the use of second-order accurate central-difference schemes to discretize the spatial terms in the governing equations. The geometry used in last case study of Chapter 4 is far-more complex because it involves a sloping seabed and a vertical-circular cylinder piercing the air-water interface. Because cell stretching and relatively large cell aspect ratios are necessarily used in this case, flux-limited schemes are used to discretize the convective terms in both the momentum equation and the interface equation to preserve the monotonicity of the solution while retaining an overall second-order accuracy (Jasak (1996)). The temporal derivatives are discretized using backward differencing that utilizes two old time levels to achieve second-order accuracy. The pressure equation is solved with a generalized geometric-algebraic multi-grid (GAMG) solver and the other linear systems are solved with the preconditioned bi-conjugate gradient (PBiCG) solver.

3.1.2 Filtering Operation

The explicit filters applied in both the *a priori* and *a posteriori* studies are based on the top-hat filter discussed in Section 2.2.1. The filter stencil is discretized based on the work of Chesnel et al. (2011a), Larocque et al. (2010), Toutant et al. (2009), Vincent et al. (2008), and Labourasse et al. (2007) where an effective volume-average of the sampled neighboring cells is computed at each cell center using:

$$\overline{\phi}(i,j,k) = \frac{1}{(2N+1)^3} \sum_{n=-N}^{N} \sum_{m=-N}^{N} \sum_{l=-N}^{N} \phi(i+n, j+m, k+l) \tag{3.4}$$

with $2N+1 = \overline{\Delta}/\Delta$, and $\overline{\Delta}$ is the LES grid-level cutoff length and Δ is the DNS grid spacing. In the *a priori* analysis, the filtered data is then down-selected onto an

effective LES grid that is coarser than the DNS resolution and is a function of the $\overline{\Delta}/\Delta$ ratio. This process ensures that only the information that would be available during actual large-eddy simulations is used to compute the modeled subgrid-scale terms and that the correlation between the modeled and true subgrid terms is not artificially enhanced by the use of information only accessible at the DNS level.

3.1.3 Validation of the *A Priori* Procedure

The *a priori* procedure is validated using the classical DNS and LES benchmarking study of the fully-developed turbulent channel flow. Several components of the subgrid-scale stress τ_{ij} are calculated using DNS data and compared to the results of Salvetti and Banerjee (1995). Additionally, the implementation of the coefficient calculation procedure used by dynamic SGS models is verified by comparing the spatial distribution of C_d inside of the channel against the previously-published results. The consistency of the *a priori* procedure is ensured by following the detailed description of Liu et al. (1994).

Salvetti and Banerjee (1995) calculate the SGS stresses using direct numerical simulations of a modified channel flow problem characterized by a no-slip wall and a free-slip boundary. The Reynolds number based on the shear velocity at the no-slip wall is $Re_\tau = 171$. The same problem setup is reproduced in OpenFOAM using second-order schemes that are demonstrated by van Haren (2011) to be fully capable of reproducing high-accuracy DNS results of canonical flows. The computational grid consists of uniformly spaced cells in the streamwise and spanwise directions and of nonuniform grid spacing in the wall-normal direction. The small cells near the no-slip boundary allow for a detailed resolution of the viscous sublayer. The RMS velocity fluctuations and the mean velocity profile are compared against the published DNS data to ensure that the solution is converged. Additionally, the classical fully-developed turbulent channel flow at $Re_\tau = 180$ with two no-slip walls is also validated

against the results of Kim et al. (1987) to verify an adequate resolution of the smallest scales of turbulence with the current numerical method.

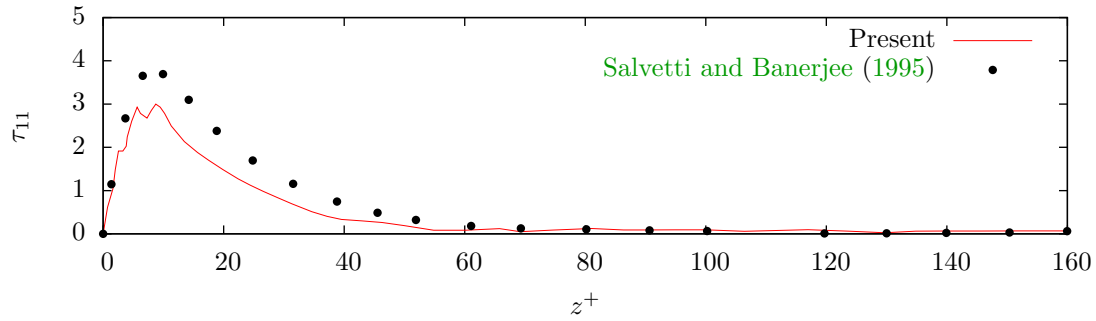

(a) SGS Stress: τ_{11}

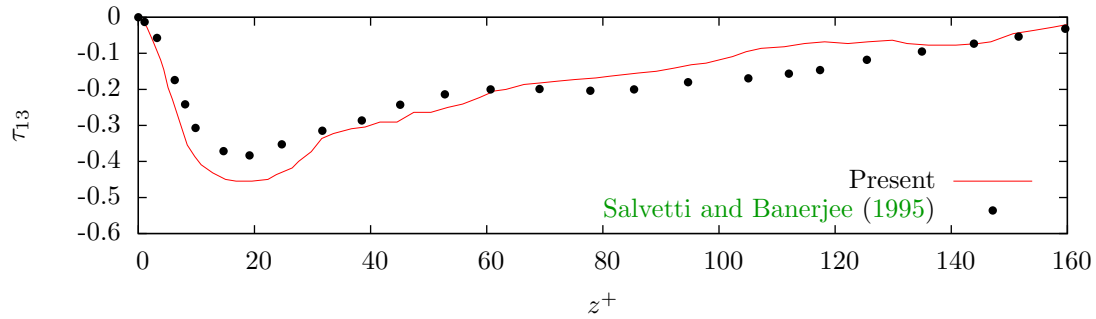

(b) SGS Stress: τ_{13}

Figure 3.1: Subgrid-scale stress components for the fully-developed turbulent channel flow ($Re_\tau = 171$)

Two components of the subgrid-scale stress (τ_{11} and τ_{13}) are shown in Figure 3.1(a) and Figure 3.1(b) as a function of non-dimensional distance to the wall z^+. The stress components are averaged on the homogeneous-horizontal planes parallel to the wall boundary. The component subscripts (1,2,3) correspond to the streamwise, spanwise, and normal directions, respectively. The general trends of the two subgrid stress components agree well with the reference results. Both stresses approach zero close to the no-slip boundary at $z^+ = 0$ and towards the middle of the channel approaching $z^+ = 160$. The location of the peak values of both components is predicted correctly, but the magnitudes are somewhat different compared to the reference results. Unlike the DNS method used here, the DNS data used by Salvetti and Banerjee (1995) were

generated using spectral methods and hence some differences between the two results are expected.

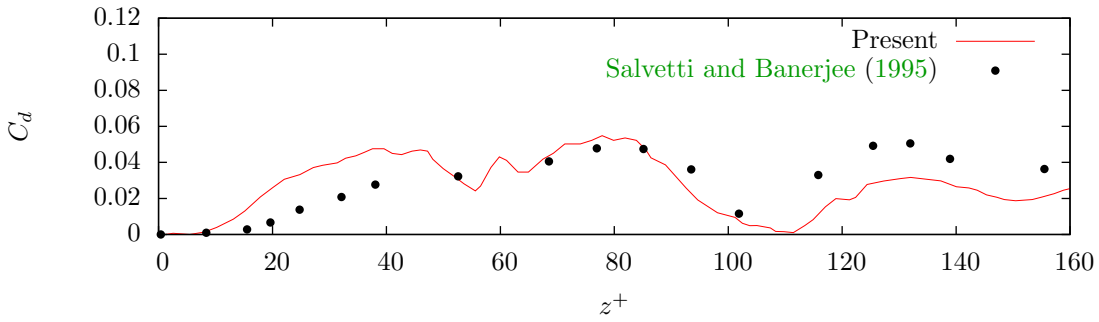

Figure 3.2: Dynamically-computed eddy-viscosity coefficient for the dynamic Smagorinsky model

The coefficient used by the dynamic Smagorinsky model is compared to the published results in Figure 3.2. The coefficient is computed dynamically based on the flow information available on the test and grid levels, and then it is averaged on the homogeneous planes parallel to the wall. The coefficient computed in the present validation study is somewhat over-estimated near the no-slip boundary, but the general variation and magnitude of the coefficient as a function of distance to the wall compares well to the reference data.

3.2 Phase Inversion

The phase-inversion problem is based on the numerical setup of Labourasse et al. (2007) used to investigate turbulence and its effect on the fluid interface. Figure 3.3 depicts a sketch of the computational domain where a square inclusion of oil initially resides in the lower left corner of a closed box filled with water. Both incompressible and immiscible fluids are initially at rest before being released and allowed to be acted upon by gravity and fluid forces. The density and kinematic viscosity of the two fluids are presented in Table 3.1. The surface tension coefficient γ is set to 0.045 N/m giving

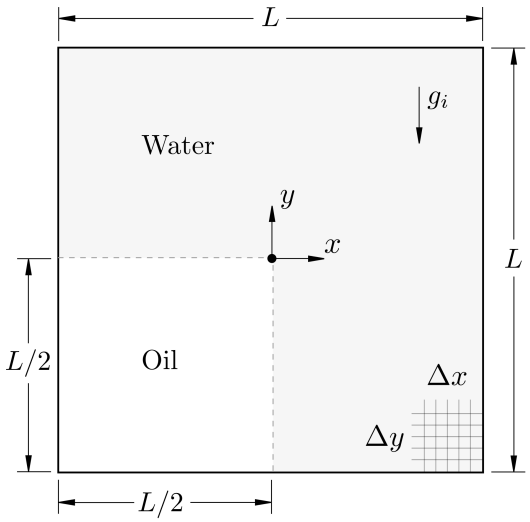

Figure 3.3: Sketch of the computational domain with the main parameters for the phase-inversion problem

a Weber number of $We = 1,090$ defined as:

$$We = \frac{(\rho_w - \rho_o)\, {u_0}^2 L/2}{\gamma}. \tag{3.5}$$

A references velocity is obtained from $u_0 = \sqrt{gL}$ where g is the gravitational acceleration and L is the width and height of the computational domain. The Reynolds number based on u_0, the height of the oil inclusion $L/2$, and the corresponding fluid density and viscosity is computed as:

$$Re_{o,w} = \frac{\rho_{o,w} u_0 L/2}{\mu_{o,w}} \tag{3.6}$$

to give $Re_w = 99,000$ in water and $Re_o = 1,456$ in oil. No-slip boundary conditions are applied at all four walls bounding the domain.

Several grid resolutions are tested to ensure solution convergence with grid refinement and a sufficient resolution of the turbulent scales. The details of the grids, including the spatial and temporal resolution, are included in Table 3.2. The previously published DNS studies of the same phase-inversion problem used uniform

Table 3.1: Properties of the water and oil phases

Phase	α $[-]$	ρ $[kg/m^3]$	ν $[m^2/s]$
Water	1	1000	5.0×10^{-6}
Oil	0	900	3.4×10^{-4}

two-dimensional grids with up to 512^2 cells. In this study, a finer grid with 768^2 cells is selected as a compromise between the resolution of the turbulent and interfacial scales of interest and the computational expense. Because the phase inversion is not a stationary problem, statistics of the velocity field are not readily accessible. The turbulent kinetic energy $k = \frac{1}{2}\left(\langle u_1' \rangle^2 + \langle u_2' \rangle^2 + \langle u_3' \rangle^2\right)$ based on the RMS of the velocity fluctuations cannot be computed without an appropriate mean velocity profile and hence determining the turbulent kinetic energy dissipation rate is difficult. The dissipation rate can be estimated based on Kolmogorov's hypotheses and dimensional analysis arguments as shown in Sagaut (2001). The turnover time of the large energetic eddies is estimated using L/u_0 and the kinetic energy of the flow is taken to be proportional to ${u_0}^2$, giving an estimated dissipation rate of turbulent kinetic energy as $\epsilon \approx {u_0}^3/L$. Using this method, the estimated Kolmogorov length scale is found to be approximately $0.0001L$ in water and $0.003L$ in oil. By similar arguments, the smallest time scale of turbulence $\tau_{\eta,K}$ is approximately 0.003 s in water and 0.022 s in oil. The resolution of the grid used in this study is not sufficient to resolve the estimated smallest scales but because close to 90% of the turbulent kinetic energy dissipation occurs at scales larger than η_K ($l/\eta_K > 8$ where l is the eddie size, see Pope (2000)), the 768^2 grid is sufficient to resolve the most active turbulent and interfacial scales of interest.

The evolution of the flow on the 768^2 grid is illustrated in Figure 3.4 through the phase-indicator variable α and contours of the second invariant of the velocity gradient tensor Q used to identify vortex structures (Chong et al. (1990)). The magnitude of

Table 3.2: Properties of the phase inversion computational grids

Grid	Cell Count	Δx, Δy $[m]$	Δt $[t]$
DNS	768^2	0.0013	0.0005
M	383^2	0.0026	0.001
	256^2	0.0039	0.001
C	191^2	0.0052	0.001

the velocity vector is also shown at the same instances in time. The less-dense oil is driven upward by buoyancy once released from the unstable initial conditions. The fluid interface undergoes a complex deformation due to the interaction between the interfacial and turbulent scales associated with the velocity and pressure gradients. The most energetic stages of the flow development take place between approximately $t = 5\ s$ and $t = 25\ s$. The interface breaks apart as the oil reaches the top wall and reflects back to further interact with the water phase. Turbulence is also generated at the no-slip boundaries because of large velocity gradients that develop near the four walls. The near-wall eddies are initially driven upwards together with the bulk of the oil phase. Once the bulk of oil collides with the top wall, droplets of various sizes develop as shown in Figure 3.4(d). The vorticies identified through the Q-criterion contours are primarily found in the water phase and near the interface of the two fluids because of the greater density and larger velocity gradients in the water phase. After approximately 100 s the flow becomes quasi-steady with the oil phase settled on top of the heavier water phase. Very small droplets of oil remain in the water phase at this point as they are slowly driven upwards by buoyancy.

3.2.1 Quantification of the Subgrid Contributions

This section focuses on quantifying the subgrid-scale terms identified in Section 2.3 using the results of the phase inversion problem. Labourasse et al. (2007), Vincent

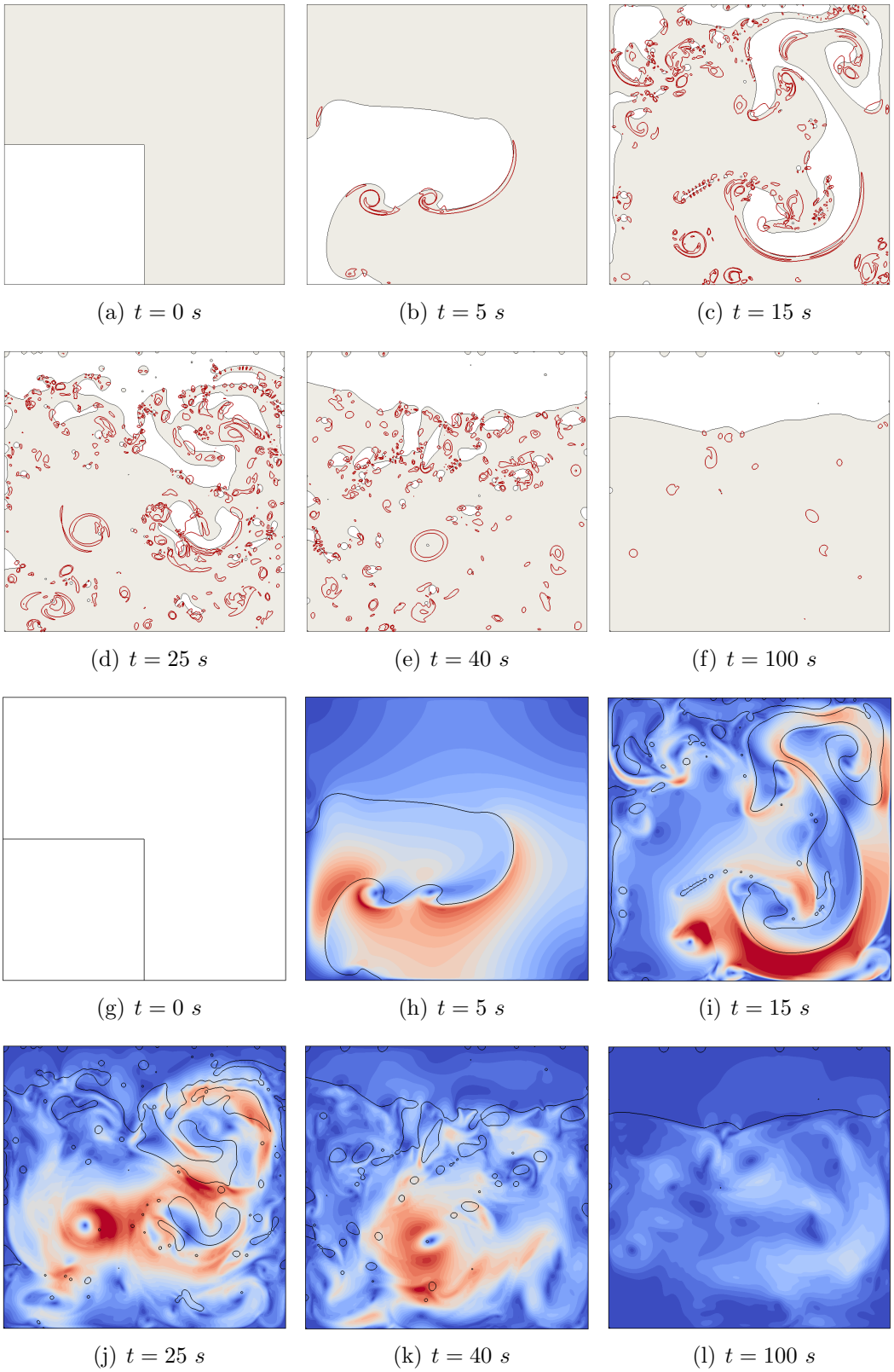

(a) $t = 0\ s$ (b) $t = 5\ s$ (c) $t = 15\ s$

(d) $t = 25\ s$ (e) $t = 40\ s$ (f) $t = 100\ s$

(g) $t = 0\ s$ (h) $t = 5\ s$ (i) $t = 15\ s$

(j) $t = 25\ s$ (k) $t = 40\ s$ (l) $t = 100\ s$

Figure 3.4: Evolution of the flow on the 768^2 DNS grid. Top two rows: phase indicator and contours of Q. Bottom two rows: magnitude of the velocity vector.

et al. (2008), and Larocque et al. (2010) have carried out a similar type of analysis of this problem while employing different numerical simulation and SGS quantification methods (see Section 2.3 for details).

Two sizes of the top-hat filter stencil are used: 3x3 (hereafter referred to as the small filter, SF) and 5x5 (large filter, LF). By changing the size of the filter, each subgrid term can be evaluated to determine its sensitivity to the change of the spatial resolution of the computational grid used for large-eddy simulations. Increasing of the filter-cutoff length-scale can be thought of as effectively using a coarser LES grid in practice. The four subgrid-scale terms quantified include the traditional convective term τ_C, diffusive term τ_D, acceleration term τ_A, and the interface term τ_I. The contribution of each of the SGS terms to the discretized equations is examined by quantifying the divergence of the convective term $\partial\tau_{Cij}/\partial x_j$, the diffusive term $\partial\tau_{Dij}/\partial x_j$, and the interface term $\partial\tau_{Ii}/\partial x_i$, as well as the time derivative of the acceleration term $\partial\tau_{Ai}/\partial t$. The surface tension SGS term is not considered in this analysis because it has been shown by Larocque et al. (2010) to have a minor effect among the hierarchy of the other subgrid-scale terms. Additionally, Lakehal and Liovic (2011) reports that for most types of breaking-wave flows, the SGS surface tension contribution is several orders of magnitude smaller than the resolved component due to the relatively negligible impact of the smallest scales on the total action of the surface tension.

The time evolution of the four SGS terms obtained through the *a priori* procedure is shown in Figure 3.5 for the first 40 seconds of the simulation time. During this stage of the flow development, the largest dissipation rates and peak kinetic energy occur. Additionally, the most complex flow features associated with the generation of turbulence and the deformation of the interface also occur at this time.

At each sampled time, the maximum of each subgrid term contribution ($\partial\tau^{max}/\partial x_i$ or $\partial\tau^{max}/\partial t$) is computed and non-dimensionalized by the largest resolved term in the

appropriate governing equation. The y-component of the divergence of the resolved convective acceleration $\partial\overline{\rho}\,\overline{u}_i\overline{u}_j/\partial x_j$ dominates the other resolved terms in magnitude and hence the subgrid terms found in the momentum equation ($\partial\tau_{Ai}/\partial t$, $\partial\tau_{Cij}/\partial x_j$, and $\partial\tau_{Dij}/\partial x_j$) are non-dimensionalized by $\partial\overline{\rho}\,\overline{u}_2\overline{u}_j/\partial x_j$. Similarly, the resolved convective term in the interface equation $\partial\overline{u}_2\overline{\alpha}/\partial x_2$ is used to non-dimensionalize the interfacial subgrid term $\partial\tau_{Ii}/\partial x_i$. This form of normalization was adapted by Larocque et al. (2010) and it was proven to give a valuable insight in the relative importance of each subgrid-scale term.

The semi-log plots (Figure 3.5) illustrate several interesting trends. The vertical component of the convective subgrid term is found to be the largest for the majority of the simulation, reaching up to approximately 35% of the resolved component at the most energetic stages of the flow. Its contribution is found to increase with the application of the larger filter as also shown by Labourasse et al. (2007) and Larocque et al. (2010). The two components of the diffusive SGS term behave similarly and are found to be the second largest subgrid contributor to the momentum equation. The contribution of the acceleration term is on the order of 10^{-4} of the maximum resolved term, or over two orders of magnitude less than the convective and diffusive terms. The importance of the interfacial term is found to increase when a larger filter is used and its overall contribution to the maximum resolved term in the interface equation is less than 3%.

In the first few seconds after the oil phase begins to rise due to buoyancy, the diffusive SGS contribution increases relative to the other SGS terms. Because the fluids are initially at rest in a highly-unstable condition, large velocity gradients form immediately upon release and the difference between the subgrid velocity gradients and the resolved gradients results in the diffusive SGS term's relative magnitude. At the same time, the subgrid interface term decreases in its contribution to the resolved component until reaching its minimum value at $t = 8\ s$. Before the bulk of the oil

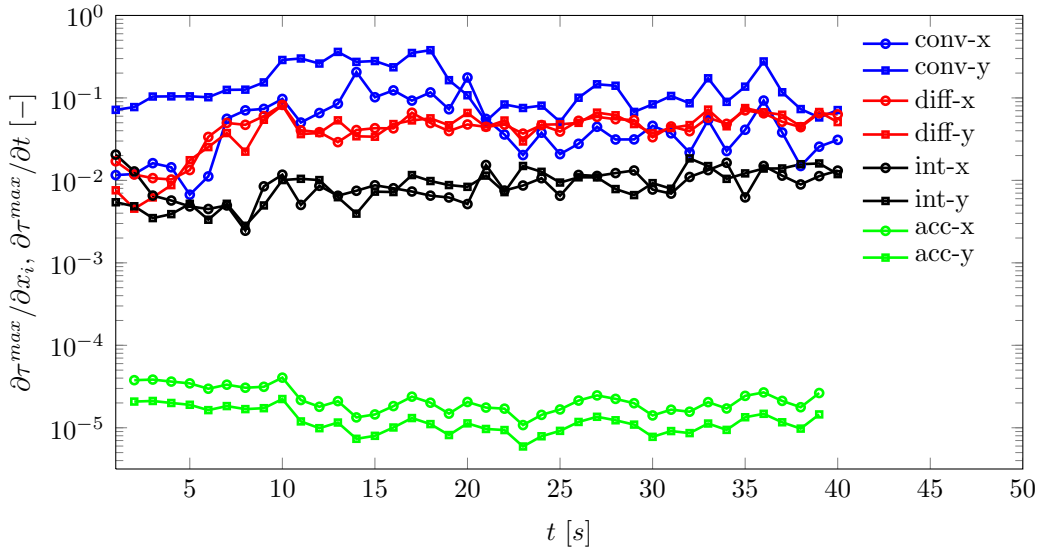

(a) Small filter: 3x3

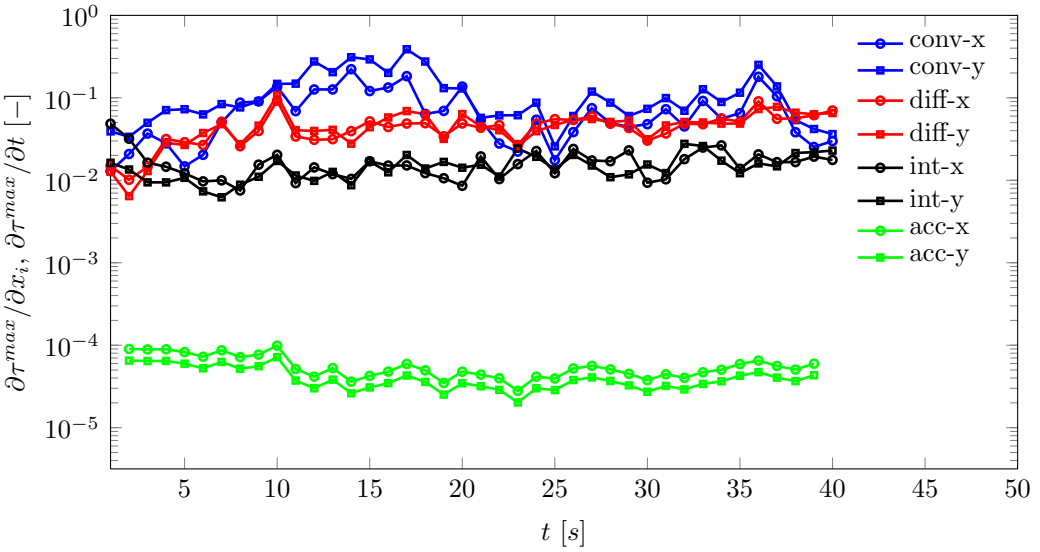

(b) Large filter: 5x5

Figure 3.5: Normalized maximum of the divergence / time derivative of the SGS terms

reaches the top of the domain, the interface is well resolved and hence the subgrid contribution is minimal. Once the oil impacts the top wall and small oil droplets form, the subgrid interfacial term increases because a significant portion of the interfacial structures are smaller than the filter cutoff. The acceleration term is affected by the change of the filter size but its relative magnitude remains small throughout the simulation, likely due to the very small size of the computational time-step used to perform the direct numerical simulations.

In the next step of the analysis, contours of the magnitude of the four subgrid-scale terms ($|\tau_C|$, $|\tau_D|$, $|\tau_A|$, $|\tau_I|$) are examined at three instances in time and as a function of the filter size. It is important to understand the behavior of the subgird terms and not just their relative size compared to the resolved terms of the governing equations because it is the individual terms that are modeled in LES using the structural approach. The contours are presented in units of kg/m^2s for τ_A, kg/ms^2 for τ_C and τ_D, and m/s for τ_I. The magnitude of a second-rank tensor is obtained using:

$$|A| = \sqrt{A_{ij}A_{ij}} \tag{3.7}$$

where A_{ij} is a generic symmetric tensor, and the magnitude of a vector is found using:

$$|B| = \sqrt{B_iB_i} \tag{3.8}$$

where B_i represents a generic vector.

The diffusive stress contribution at $t = 5\ s$ is illustrated in Figure 3.6(a) using the small filter stencil. The convective and acceleration subgrid terms are also included at this time in Figure 3.6(b) and 3.6(c). The maximum diffusive subgrid stress is found in a relatively small region of the oil phase near the left wall of the domain. At the latter stages of the simulation, the subgrid diffusive term decreases in magnitude and its contribution is mostly found near the oil-water interface as shown in Figures 3.6(d)

and 3.6(g). As expected, the overall subgrid contribution decreases with time as the flow approaches a steady state. An increase of the filter stencil size results in the diffusive SGS stress mostly retaining its relative magnitude as shown in Figure 3.5(b). The contours of $|\tau_D|$ obtained using the 5x5 filter shown in Figures 3.7(d) and 3.7(g) indicate that the diffusive SGS term becomes more active near the interface.

The convective subgrid term reaches its maximum contribution between $10\ s < t < 20\ s$ once the bulk of the oil reaches the top of the domain. As the filter stencil is increased, the convective SGS term increases and reaches up to 40% of the resolved maximum. Figures 3.6(b), 3.6(e), and 3.6(h) show how the convective subgrid term behaves at three instances in time. This term is found to be active in highly-vortical regions and near the interface. In Figure 3.7(h), the contours of $|\tau_C|$ are relatively small in magnitude but they populate the majority of the water phase where vorticies and droplets of oil are present. A large portion of the turbulent structures is found to be below the cutoff length of the large filter at this time.

The interface term is examined in Figure 3.8. As anticipated, this term is active only in the diffuse-interface region where the value of the volume fraction α changes between the oil and water phases. The application of the spatial filter in this region results in an effective coarsening of the interface which in turn results in a loss of interfacial detail. As the filter size is increased, the magnitude of the subgrid term is found to increase rapidly. Figure 3.5 indicates that the ratio of $\partial\tau_{Ii}/\partial x_i$ to its resolved equivalent increases by approximately 50% when the large filter is used. The interfacial subgrid term accounts for only approximately 1 to 3% of the resolved term with the application of the large filter, but because its rate of change is higher than of the other subgrid terms, the contribution of the interfacial term is likely to be on the order of the convective SGS term on coarse LES grids. Additionally, the fluid interface is governed by a separate equation from the Navier-Stokes equations, allowing for a unique approach to the modeling of the subgrid interfacial term as part

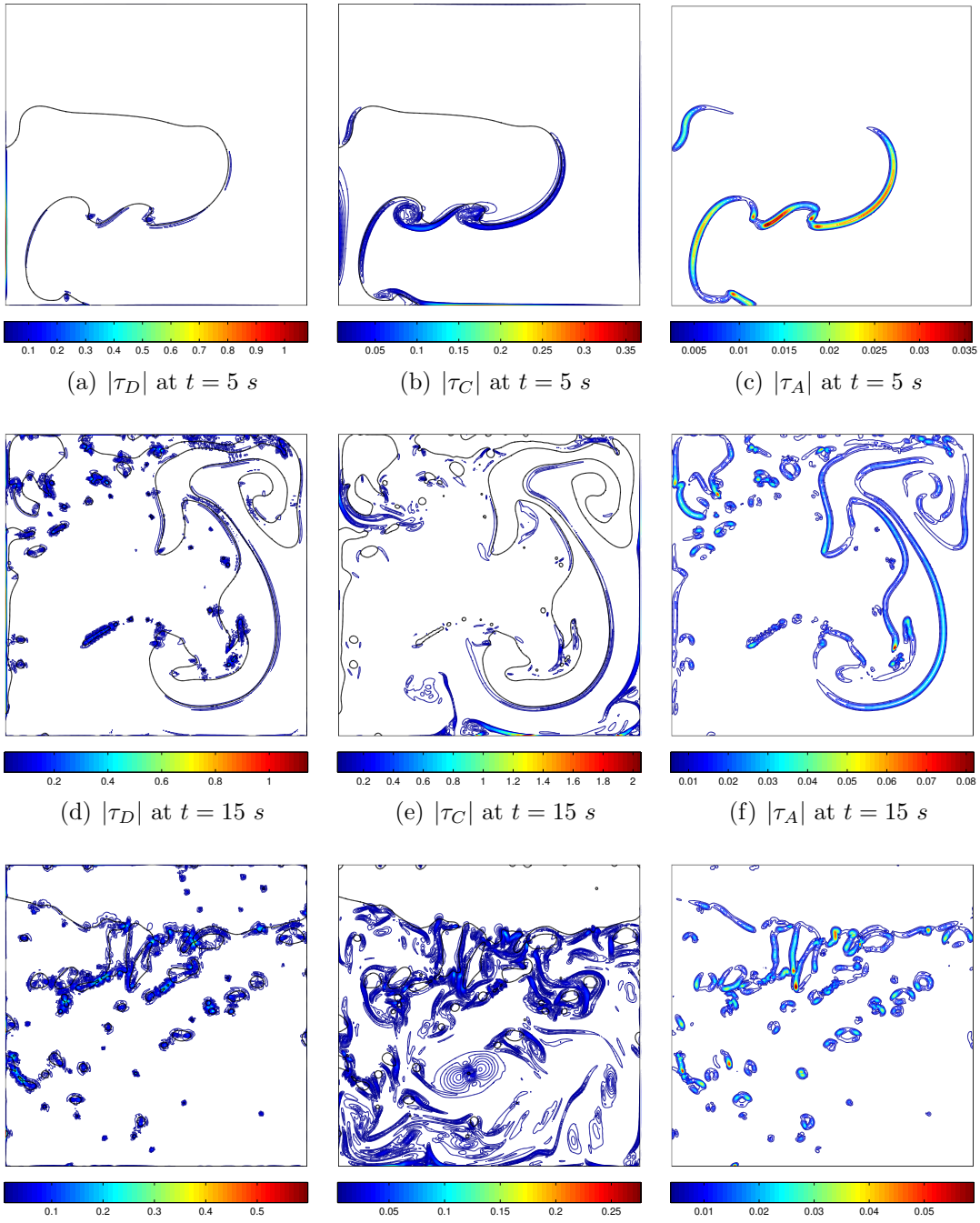

(a) $|\tau_D|$ at $t = 5\ s$ (b) $|\tau_C|$ at $t = 5\ s$ (c) $|\tau_A|$ at $t = 5\ s$

(d) $|\tau_D|$ at $t = 15\ s$ (e) $|\tau_C|$ at $t = 15\ s$ (f) $|\tau_A|$ at $t = 15\ s$

(g) $|\tau_D|$ at $t = 40\ s$ (h) $|\tau_C|$ at $t = 40\ s$ (i) $|\tau_A|$ at $t = 40\ s$

Figure 3.6: Magnitude of the subgrid terms in the momentum equation using the small filter (3x3)

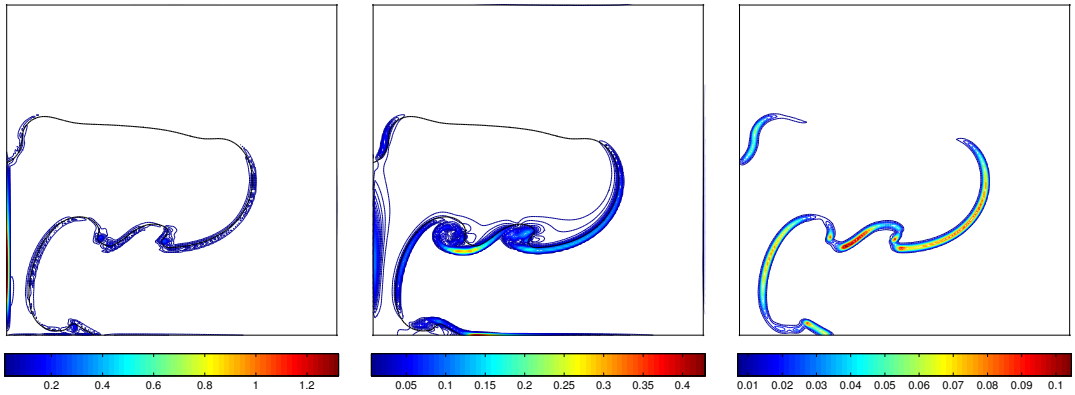

(a) $|\tau_D|$ at $t = 5\ s$ (b) $|\tau_C|$ at $t = 5\ s$ (c) $|\tau_A|$ at $t = 5\ s$

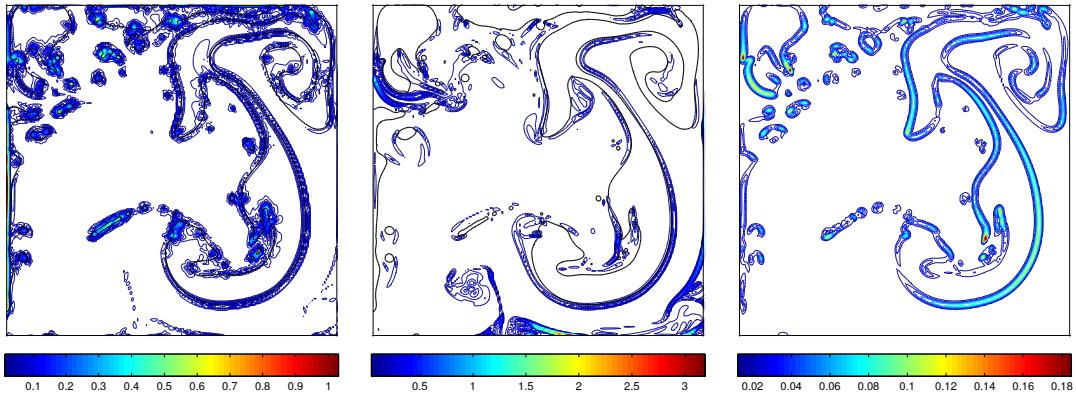

(d) $|\tau_D|$ at $t = 15\ s$ (e) $|\tau_C|$ at $t = 15\ s$ (f) $|\tau_A|$ at $t = 15\ s$

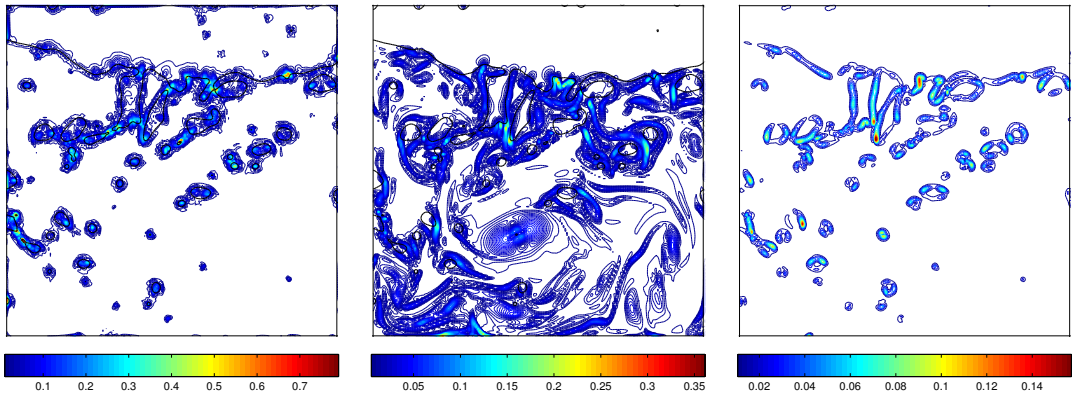

(g) $|\tau_D|$ at $t = 40\ s$ (h) $|\tau_C|$ at $t = 40\ s$ (i) $|\tau_A|$ at $t = 40\ s$

Figure 3.7: Magnitude of the subgrid terms in the momentum equation using the large filter (5x5)

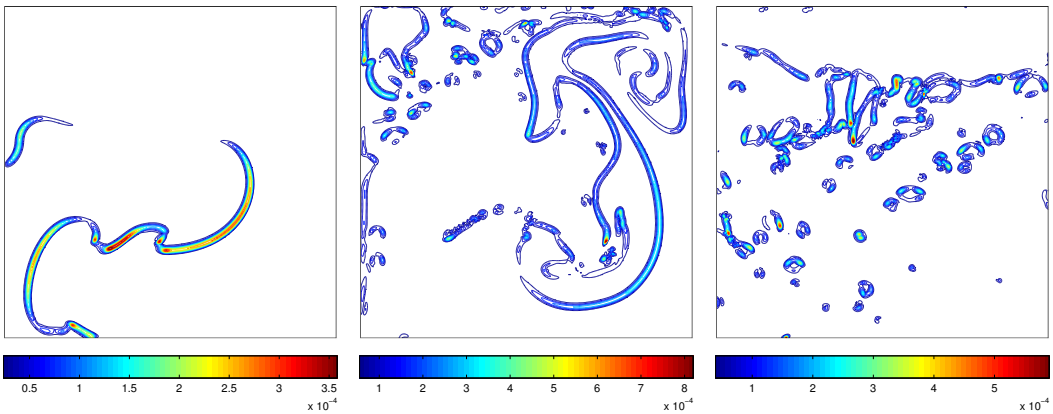

(a) SF, $t = 5\ s$ (b) SF, $t = 15\ s$ (c) SF, $t = 40\ s$

(d) LF, $t = 5\ s$ (e) LF, $t = 15\ s$ (f) LF, $t = 40\ s$

Figure 3.8: Magnitude of the interface subgrid term $|\tau_I|$

of the interface equation.

3.2.2 Modeling of the Subgrid-Scale Terms

In this section, the subgrid-scale terms are modeled using the filtered DNS data of the phase-inversion problem. The filtered data available on the LES grid level is used to compute the contribution of the tested LES models, as described in Chapter 2. The *a priori* testing of the SGS models allows for an insight into the model's ability to replicate the interaction of the resolved and subgrid scales. The traditional convective SGS stress tensor τ_C is modeled using the dynamic Smagorinsky, the scale-similarity, and the stress-similarity models. The original scale-similarity model of Bardina et al. (1980) is compared to its generalized version or the stress-similarity model introduced by Liu et al. (1994). The two similarity-based models and the dynamic eddy-viscosity model are also used as a proxy to evaluate the potential benefit of the mixed SGS modeling that combines an eddy-viscosity contribution with a similarity-type contribution. The stress-similarity concept is extended to the modeling of the diffusive, the acceleration, and the interfacial subgrid-scale terms.

The performance of each model is evaluated based on the correlation coefficients between the real subgrid stresses and the modeled stresses. This approach is based on the work of Liu et al. (1994) that involved the study of turbulence in a round jet, as well as the work of Chesnel et al. (2011a) which focused on spray-atomization problems. The magnitude of each subgrid term (see Equations 3.7 and 3.8) is used for the correlation coefficient calculation to simplify the analysis. The correlation coefficient r for two variables a and b is found using:

$$r = \frac{\langle ab \rangle - \langle a \rangle \langle b \rangle}{\sqrt{\left(\langle a^2 \rangle - \langle a \rangle^2\right)\left(\langle b^2 \rangle - \langle b \rangle^2\right)}} \tag{3.9}$$

where $\langle\rangle$ is the mean. The coefficient can vary between -1 indicating negative corre-

lation, and 1 indicating positive correlation, while a zero value of r corresponds to no correlation between the two variables.

The convective SGS term is studied first. The general forms of the modeled convective SGS stress tensor can be summarized as:

$$\tau_{C_{ij}}^{*} - \frac{1}{3}\tau_{C_{ii}}^{*}\delta_{ij} = -C_d\overline{\Delta}^2\left|\overline{S}\right|\left(\frac{\partial\overline{u}_i}{\partial x_j} + \frac{\partial\overline{u}_j}{\partial x_i}\right), \tag{3.10}$$

$$\tau_{C_{ij}}^{*} = \overline{\overline{\rho}\,\overline{u}_i\overline{u}_j} - \overline{\overline{\rho}}\,\overline{\overline{u}}_i\,\overline{\overline{u}}_j, \tag{3.11}$$

$$\tau_{C_{ij}}^{*} = C_C\left(\widehat{\overline{\rho}\,\overline{u}_i\overline{u}_j} - \widehat{\overline{\rho}}\,\widehat{\overline{u}}_i\,\widehat{\overline{u}}_j\right), \tag{3.12}$$

for the dynamic Smagorinsky, scale-similarity, and stress-similarity models, respectively. The star superscript is used to denote the modeled terms. The correlation coefficient for the three models are shown as a function of time and filter size in Figure 3.9. The scale-similarity model employing a double grid filtering procedure shows the best correlation with the true subgrid-scale convective stress, while the stress-similarity model yields a comparable time history but with a slightly lower correlation throughout the simulation. The difference between the two results is associated with the use of two different filter-cutoff lengths for the stress-similarity model and one filter-cutoff length in the case of the original scale-similarity model (Sagaut (2001)). The correlation coefficient of the dynamic Smagorinsky model drops off to approximately 0.3 after the first two seconds of the simulation. Unlike the dynamic Smagorinsky model, the two similarity-type models show a rapid increase in their correlation coefficients after $t = 15\ s$. A close inspection of C_d for the eddy-viscosity model indicates large fluctuations of the dynamically-computed coefficient throughout the domain after $t = 2\ s$. One of the assumptions of the dynamic procedure involves the use of the same coefficient for the description of the subtest and subgrid stresses. Because a significant portion of the domain contains the fluid interface and hence the fluid properties change rapidly as a function of space, this assumption breaks down

leading to very large oscillations of the dynamic coefficient.

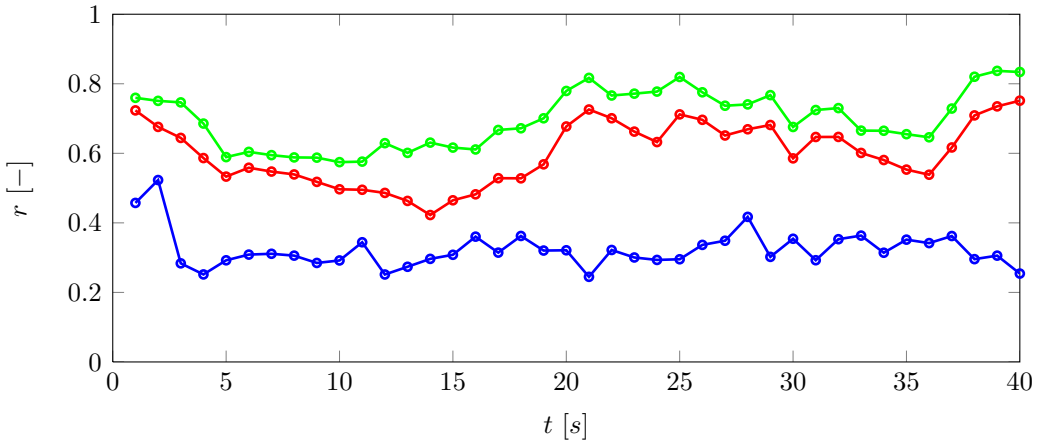

(a) Small filter: 3x3

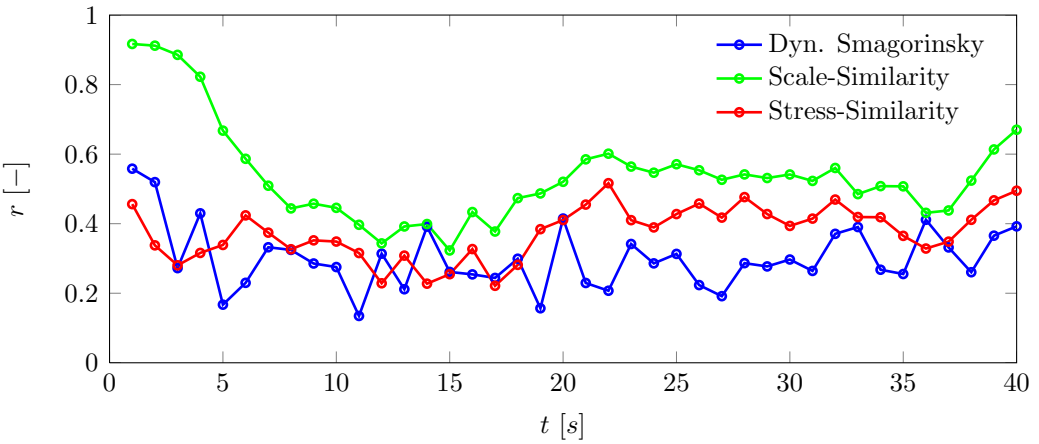

(b) Large filter: 5x5

Figure 3.9: Correlation coefficient for the convective SGS stress magnitude

The application of the larger filter stencil degrades the performance of all three tested models for a large portion of the sampled simulation time. The average correlation coefficient of the dynamic Smagorinsky model remains close to approximately 0.3, but the coefficient is found to oscillate in time to a greater extent. Because both the grid-level and test-level filter size is increased, the previously discussed assumption of the dynamic procedure further degrades the model's performance. The stress-similarity model is found to collerate just as poorly as the eddy viscosity model between $0\ s < t < 20\ s$. The correlation of the scale-similarity model is also degraded

during this time, reaching a low of approximately 0.35 at $t = 15\ s$. The use of the large filter stencil effectively corresponds to an LES grid with 128^2 cells. The relatively coarse grid is then test filtered using a stencil size based on $\widehat{\overline{\Delta}} = 2\overline{\Delta}$, resulting in a poor estimation for the test-level stress from the grid-filtered information. This behavior will be examined further as part of the following analysis.

The stress-similarity model with constant coefficients is now used to compute the modeled subgrid contribution of the acceleration, the interfacial, and the diffusive terms. The terms are modeled using:

$$\tau_{A_i}^* = C_A \left(\widehat{\overline{\rho}\,\overline{u}_i} - \widehat{\overline{\rho}}\,\widehat{\overline{u}}_i \right), \tag{3.13}$$

$$\tau_{I_i}^* = C_I \left(\widehat{\overline{u}_i\,\overline{\alpha}} - \widehat{\overline{u}}_i\,\widehat{\overline{\alpha}} \right), \tag{3.14}$$

$$\tau_{D_{ij}}^* = C_D \left(\widehat{M} - N \right), \tag{3.15}$$

where

$$M = \overline{\mu} \left(\frac{\partial \overline{u}_i}{\partial x_j} + \frac{\partial \overline{u}_j}{\partial x_i} \right) \tag{3.16}$$

$$N = \widehat{\overline{\mu}} \left(\frac{\partial \widehat{\overline{u}}_i}{\partial x_j} + \frac{\partial \widehat{\overline{u}}_j}{\partial x_i} \right) \tag{3.17}$$

and C_A, C_I, C_D are the stress-similarity coefficients set equal to one based on the arguments presented in Section 2.2.2. The convective term modeled using stress-similarity (Equation 3.12) is also included as a reference. The correlation coefficients for the four subgrid stresses are included in Figure 3.10(a) for the small filter and in Figure 3.10(b) for the large filter. It is worthwhile to point out that the interface and the acceleration terms have the same correlation coefficient and hence the two lines overlap in the plots. This result is due to the definitions of the two terms and of the correlation coefficient. The acceleration term involves products of the filtered velocity field and the filtered density while the interface term contains products of the

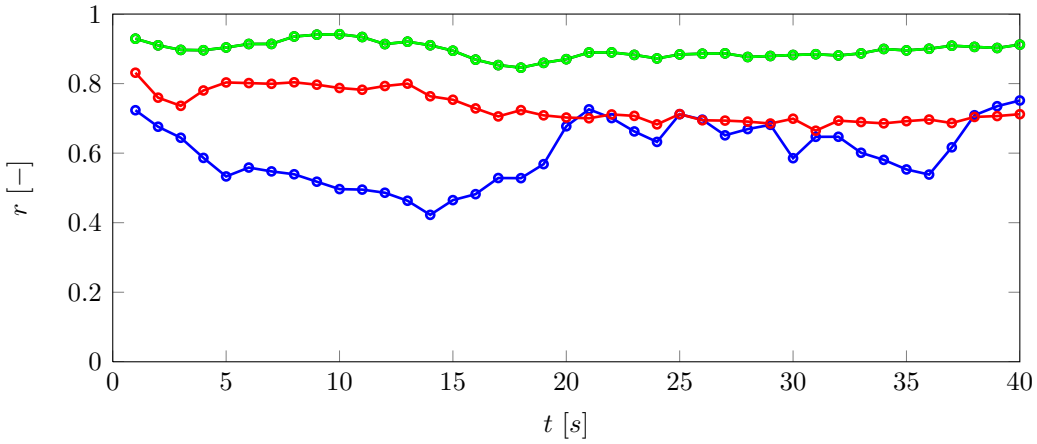

(a) Small filter: 3x3

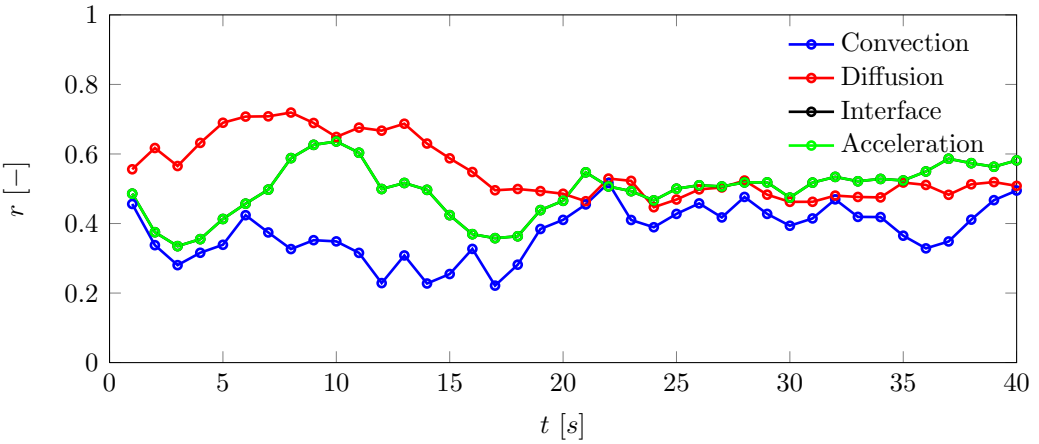

(b) Large filter: 5x5

Figure 3.10: Stress-similarity correlation coefficient for the convective, diffusion, acceleration, and interface SGS stress magnitudes

filtered velocity field and the filtered volume fraction. The density and the volume fraction fields are only different in magnitude and units because the density field is a function of the volume fraction (see Equation 2.36). The correlation coefficients of the interface and acceleration terms stay between 0.8 and 1.0 for the entire sampled simulation time when the small filter stencil is applied, indicating that the test-level information adequately models the subgrid stresses. The correlation of the two terms is significantly reduced to an average value of approximately 0.5 by filtering the DNS data with a greater filter-cutoff length. A similar trend of the correlation coefficient degradation is found for the diffusive and convective terms modeled with the stress-similarity approach.

The effects of the filter size on the robustness of the stress-similarity model can be studied further by examining the modeled contribution directly and comparing it to the true subgrid term obtained from the DNS data. The analysis is carried out for the interface SGS term only at three instances in time (t = 5, 15, 40 s), but the findings are directly relevant to the other SGS stresses modeled with the stress-similarity technique. Contours of $|\tau_I|$ are compared to the contours of the modeled term $|{\tau_I}^*|$ in Figure 3.11. The small grid filter is used and the stress-similarity model utilizes a secondary test-level filter that is twice the size of the grid filter ($\widehat{\overline{\Delta}} = 2\overline{\Delta}$). A close inspection of the results shows that the model is active in the appropriate regions of the domain where the true SGS term is present. At $t = 5\ s$ and $t = 15\ s$, the maximum of the modeled contribution is between two to three times greater than the maximum of the true subgrid term, but the locations of the peak subgrid contribution are reproduced well by the model. Based on these findings, a dynamic determination of the stress-similarity coefficient or an adjustment to the ratio between the test and grid filter cutoff could be beneficial to the prediction of the correct magnitude of the modeled contribution.

Figure 3.12 illustrates the limitation of the test-filtering procedure that is at the

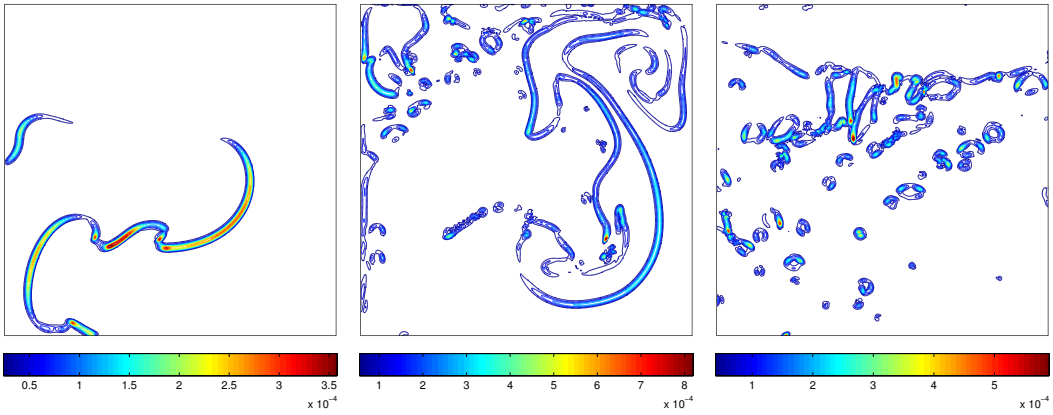

(a) $|\tau_I|$ at $t = 5\ s$ (b) $|\tau_I|$ at $t = 15\ s$ (c) $|\tau_I|$ at $t = 40\ s$

(d) $|\tau_I{}^*|$ at $t = 5\ s$ (e) $|\tau_I{}^*|$ at $t = 15\ s$ (f) $|\tau_I{}^*|$ at $t = 40\ s$

Figure 3.11: Magnitude of the true interface subgrid term $|\tau_I|$ and the modeled contribution $|\tau_I{}^*|$ using the stress-similarity approach. Small filter (3x3) and $C_I = 1$.

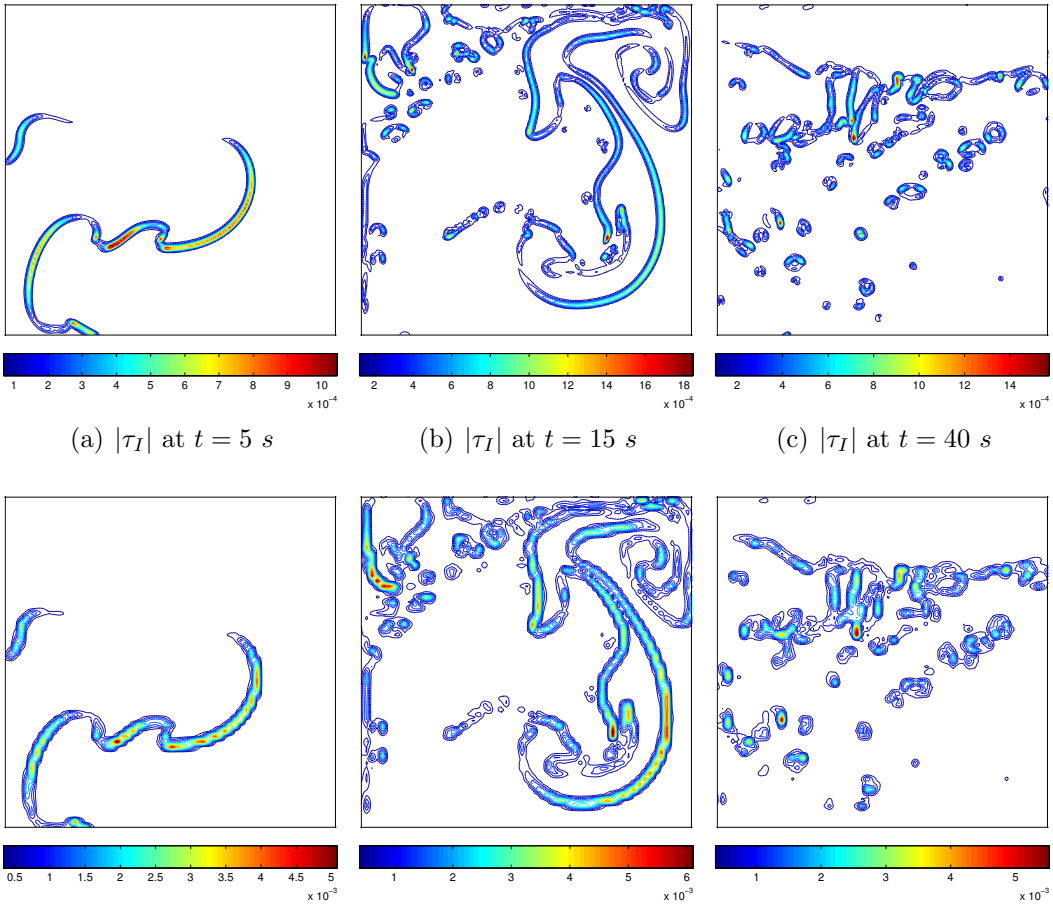

(a) $|\tau_I|$ at $t = 5\ s$ (b) $|\tau_I|$ at $t = 15\ s$ (c) $|\tau_I|$ at $t = 40\ s$

(d) $|\tau_I{}^*|$ at $t = 5\ s$ (e) $|\tau_I{}^*|$ at $t = 15\ s$ (f) $|\tau_I{}^*|$ at $t = 40\ s$

Figure 3.12: Magnitude of the true interface subgrid term $|\tau_I|$ and the modeled contribution $|\tau_I{}^*|$ using the stress-similarity approach. Large filter (5x5) and $C_I = 1$.

core of the stress-similarity model. The grid filter is now increased to the 5x5 stencil and the test-level filter is increased accordingly. The magnitude of the true subgrid stress is found to increase as previously shown, but the contribution of the model is poorly correlated with the true SGS stress in terms of magnitude and location in the domain. The peak contribution is more than an order of magnitude smaller at all three instances in time and the flow information available on the test-filter level is not sufficiently resolved to model the subgrid term. The locations of the peak model contribution at the fluid interface no longer match the locations of the peak magnitude of $|\tau_I|$ and the modeled subgrid stress appears heavily smeared and contaminated with spurious information.

Highly-resolved simulations of the phase-inversion problem are used to determine the hierarchy of the subgrid-scale terms present in the governing equations. The convective term is found to be the largest subgrid contributor relative to the resolved quantities, but the diffusive and the interfacial subgrid terms can also be significant. The acceleration term is the smallest subgrid contributor regardless of the filter size used. The interfacial term rapidly increases in magnitude with the increase of the filter stencil. The stress-similarity-based modeling of the subgrid terms is found to correlate well with the true subgrid behavior, but the correlation degrades as the filter size is increased.

3.3 Plunging-Breaking Wave

In this section, a plunging-breaking water wave is examined using high-resolution numerical simulations. The plunging-breaking wave flow shares some important characteristics with the phase-inversion problem, but the greater fluid density and viscosity ratios used in the wave-breaking problem introduce new unknowns and challenges in the understanding of the interface-turbulence interaction. The results presented

here are based on the work of Iafrati (2009, 2011) and Iafrati et al. (2012) where two-dimensional simulations are used to study the early stages of wave breaking. In those works, several modes of breaking are investigated ranging from a weak-spilling type to a strong-plunging type depending on the initial conditions used.

A similar simulation technique is used here to extend on the previously-published two-dimensional results. An artificially-steep wave is initialized in a domain with periodic boundaries in the streamwise direction and no-slip top and bottom boundaries. The periodic boundaries and the wave initialization at $t = 0$ s allow for a significant savings in terms of computational expense because the dispersive focusing of a set of waves does not need to be simulated to obtain the initial conditions of interest. This approach for simulating water waves has also been adapoted in Song and Sirviente (2004) and Lubin (2004) among others. Three-dimensional simulations are conducted using a computational domain shown in Figure 3.13 with dimensions of $\lambda \times \lambda \times \lambda/2$ (in the x, y, and z directions, respectively) and where the lateral boundaries are also periodic. Stokes's third-order wave theory is used to initialize the free-surface elevation η and the streamwise and vertical water-particle velocities u, v using:

$$\eta(x,0) = \frac{A}{\lambda}\left(\cos(kx) + \frac{1}{2}\sigma\cos(2kx) + \frac{3}{8}\sigma^2\cos(3kx)\right), \tag{3.18}$$

$$u(x,y,0) = \Omega A e^{ky}\cos(kx), \tag{3.19}$$

$$v(x,y,0) = \Omega A e^{ky}\sin(kx), \tag{3.20}$$

where $\sigma = Ak$ is the wave steepness and $\Omega = \sqrt{gk\,(1+\sigma^2)}$ is the wave frequency corrected for nonlinear effects as shown in Whitham (1974). The wave train is simulated in deep water with $h/\lambda = 0.5$ resulting in negligible effects of the no-slip bottom on the evolution of the wave-breaking process.

Parameters of air and water are included in Table 3.3 and both phases are assumed

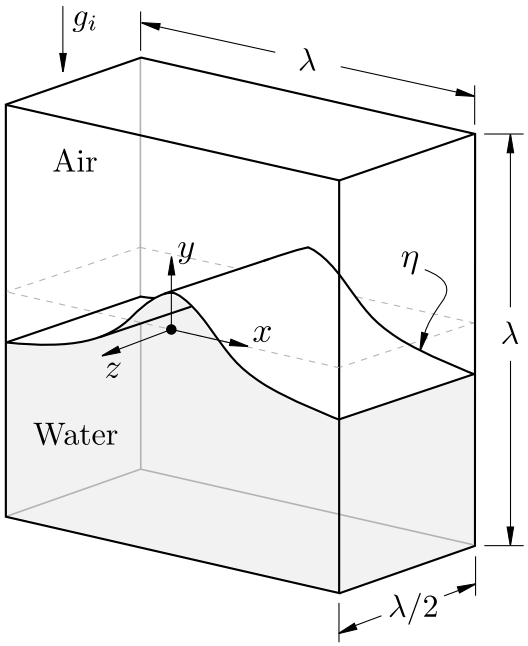

Figure 3.13: Sketch of the computational domain with the main parameters for the plunging-breaking wave problem

to be incompressible. Following Iafrati (2011), the ratio of the fluid densities is set to the physical value of $\rho_a/\rho_w = 0.00125$, whereas the ratio of the dynamic viscosities is $\mu_a/\mu_w = 0.04$ or approximately twice the physical value at room temperature. The adjustment of the viscosity ratio was justified based on numerical stability reasoning and was shown to have a minor impact on the analysis of the wave-breaking process. The same ratio is adapted in this work because the present results are first validated in two dimensions against the previously-published data. The reference velocity is

Table 3.3: Properties of the air and water phases

Phase	α $[-]$	ρ $[kg/m^3]$	ν $[m^2/s]$
Air	0	1.25	3.2×10^{-3}
Water	1	1000	1.0×10^{-4}

found using $u_0 = \sqrt{\lambda g}$ and the surface tension coefficient is chosen to give $We = 100$

using:

$$We = g^{1/2}\lambda\sqrt{\frac{\rho_w}{\gamma}}. \tag{3.21}$$

Selecting this Weber number corresponds to simulating a wave with $\lambda = 0.27\ m$, the Reynolds number in water is set to $Re_w = 10,000$, and the Froude number is $Fr = 1.0$.

3.3.1 Validation Study

The resolution of the smallest scales of turbulence necessary to conduct direct numerical simulations is first verified using two-dimensional simulations. Two types of breaking are studied: a spilling-breaking wave with an initial steepness of $\sigma = 0.35$ as well as a plunging-breaking wave with a steepness of $\sigma = 0.60$. The reference grid is selected to have 512 uniformly-spaced cells in the streamwise and vertical directions based on the previously-published results. One coarser grid with 256^2 cells and two finer grids with 1024^2 and 2048^2 uniformly-spaced cells are also constructed. All simulations span six wave periods defined as $T = \sqrt{gk}$.

The simulations are carried out using second-order numerical schemes and the interface capturing method described in Section 3.1. The interface is spread across approximately 1% of the wave length. The influence of the interface thickness was examined by comparing the global flow quantities with the thickness varying between 0.2% and 3% of wave length on the finest grid. Negligible differences of the global quantities such as the total energy in the domain and each phase were found across all tested interface thicknesses. Further analysis of the impact of the diffuse-interface technique can be found in Iafrati (2009).

The mechanical energy is each phase is found by summing the kinetic and potential

energy contributions and integrating over the phase volume:

$$E = KE + PE = \frac{1}{2}\int_{V_\alpha} \rho\left(u^2 + y^2\right)\,\mathrm{d}V + \int_{V_\alpha} \rho g y\,\mathrm{d}V. \tag{3.22}$$

The energy in the water phase is summed over the regions where $1 \geq \alpha \geq 0.99$ and in the air phase where $0 \leq \alpha \leq 0.01$. Figure 3.14 shows the total energy in each phase for the spilling-breaking wave, non-dimensionalized with $\rho_w g \lambda^3$. Results on the four different grid resolutions are plotted.

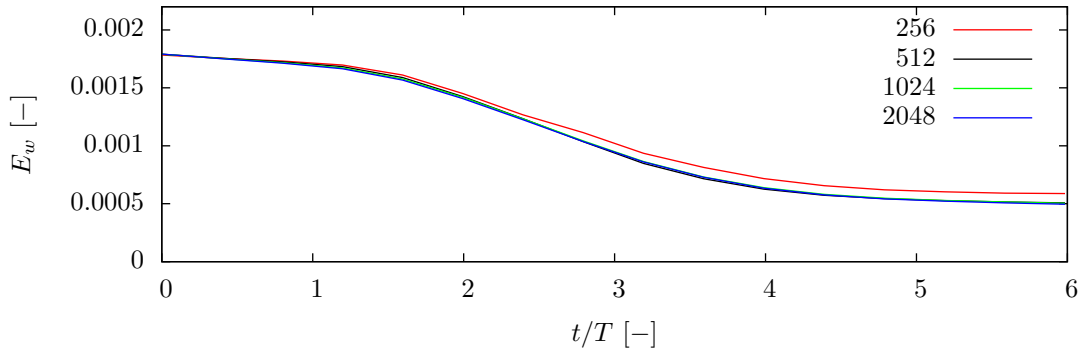

(a) Water phase

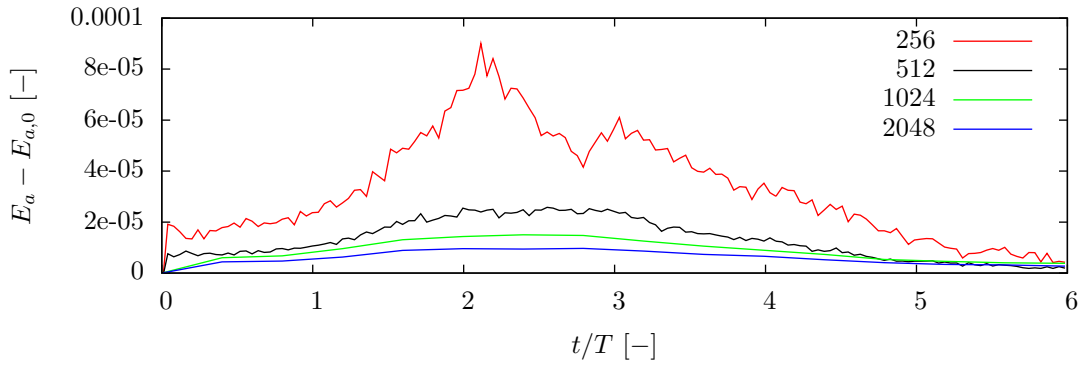

(b) Air phase

Figure 3.14: Total non-dimensional energy in each phase as a function of time and grid resolution. Two-dimensional simulation of the spilling-breaking wave with $\sigma = 0.35$.

The water phase is found to contribute the majority of the total energy in the domain because of the greater density. After approximately $1.5T$ the wave train breaks through spilling and the energy initially contained in water is transfered to

the air phase. The flow reaches a quasi-steady state after approximately $t/T = 5$. The solution in both phases converges with grid refinement and the reference grid with 512^2 cells is found to sufficiently resolve the flow. The difference between the tested grid resolutions appears greater in the air phase because the energy in air is several orders of magnitude smaller than in water. The details of simulations and the estimated smallest scales of turbulence found in the two interfacial flows is included in Table 3.4. Moin and Mahesh (1998) note that when using second-order central-

Table 3.4: Simulation parameters for the validation study

N_i	η_K/λ [−]	$\Delta x_i/\lambda$ [−]	$\eta_K/\Delta x_i$ [−]	$\tau_{\eta,K}/T$ [−]	$\tau_{\eta,K}/\Delta t$ [−]
	0.0010			0.004	
256		0.0040	0.25		20
512		0.0020	0.50		20
1024		0.0010	1.00		30
2048		0.0005	2.00		30

difference schemes the grid resolution must be finer than the Kolmogorov length scales to accurately reproduce the smallest scales of turbulence. Only the finest grid with 2048^2 cells has the sufficient resolution to simulate the Kolmogorov length scales, but based on the arguments presented in Section 3.2, the resolution of the reference grid (512^2) is sufficient to reproduce the most active dissipative scales. These arguments are also verified by the converged kinetic and potential energy throughout the simulation.

3.3.2 Results and Discussion

The problem of a plunging-breaking wave is now studied in three dimensions based on the results of the two-dimensional validation study. The addition of the spanwise dimension allows for a more-complete description of the turbulent breaking process, especially in the latter stages of the flow development where three-dimensional tur-

bulent and interfacial structures are important (Iafrati (2011); Lubin et al. (2006)). The domain spans over 0.5λ in the z-direction and is discretized with 512 cells in the streamwise and vertical directions, and 256 cells in the spanwise direction. The cells are uniformly spaced in all directions. The selected discretization of the domain is based on the two-dimensional validation study where the results obtained on the reference grid with 512^2 cells were shown to be converged. Lubin et al. (2006) reports a slight increase in the dissipation rate of a three-dimensional plunging breaker compared to a two-dimensional simulation but the grid resolution used here is sufficient to resolve at least the early stages of the breaking process because the increase in the dissipation rate was found in the post-breaking stages of the flow development. The three-dimensional simulations are conducted on a grid with over 67 million cells and approximately 1,100 computational cores were used to execute the simulations over 144 hours on the Lonestar High Performance Computing (HPC) cluster. The Lonestar HPC is part of the Extreme Science and Engineering Discovery Environment (XSEDE) and the cluster consist of over 22,000 modern computational cores with 44 terabytes of total memory and a peak performance of 302 teraflops.

The initial free-surface profile and the early stages of the breaking process are shown on a centerline plane in Figure 3.15. Several contours of the second invariant of the velocity gradient tensor Q and the magnitude of the velocity vector are also included. The identified turbulent structures are found to remain in close proximity to the fluid interface and to the entrained air cavities. The peak velocities are located in the region of the jet splash-up and where the overturning jet collapses. The magnitude of the velocity decreases rapidly away from the interface, resulting in large gradients of velocity in both phases.

The evolution of the potential and the kinetic energy in the water phase is shown in Figure 3.16. The total kinetic energy in the domain including the air phase is also shown. The bulk of the kinetic energy is contained within the water phase. The

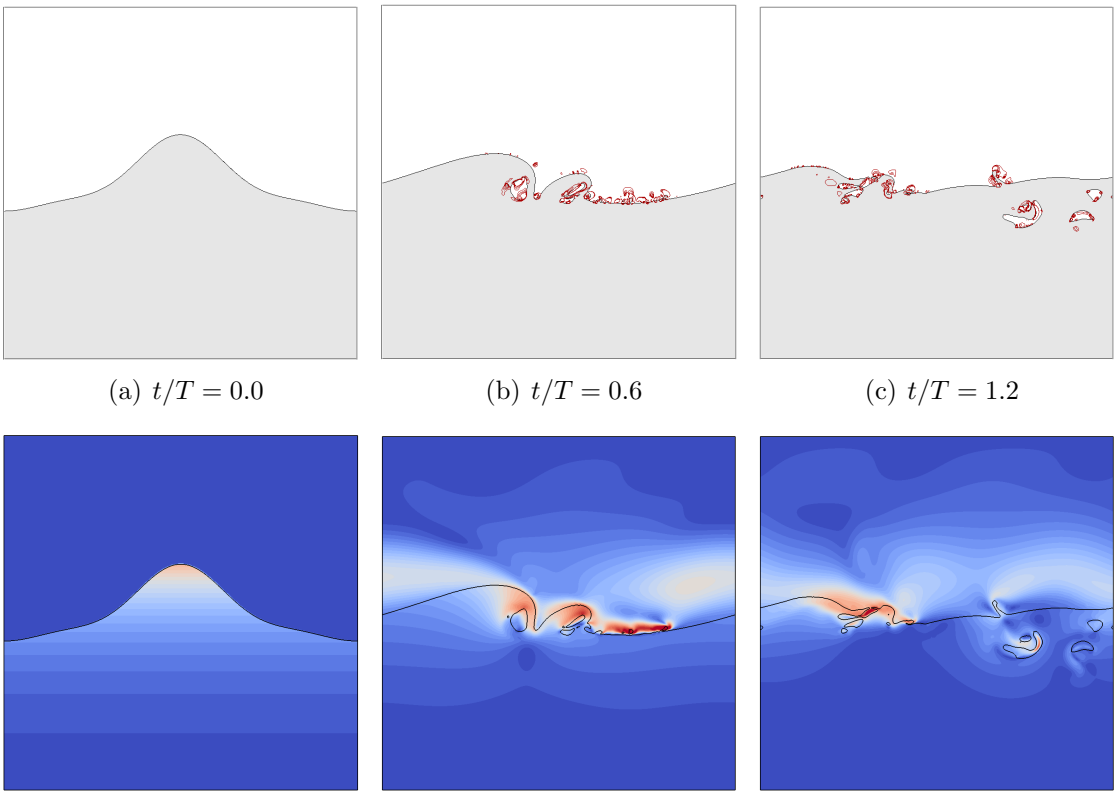

(a) $t/T = 0.0$ (b) $t/T = 0.6$ (c) $t/T = 1.2$

(d) $t/T = 0.0$ (e) $t/T = 0.6$ (f) $t/T = 1.2$

Figure 3.15: Evolution of the plunging-breaker flow on the DNS grid. Top row: dark gray regions represent the water phase and the contours of the second invariant of the velocity gradient tensor Q are shown in red. Bottom row: magnitude of velocity vector.

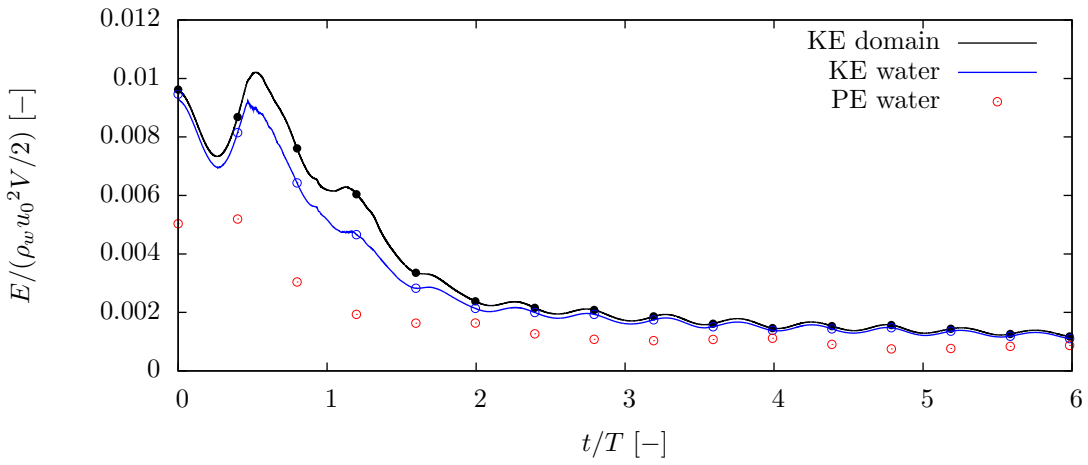

Figure 3.16: Time evolution of the potential and kinetic energy of the three-dimensional plunging-breaking wave

kinetic energy is initially converted into potential energy as the crest of the wave gains height between $0 < t/T < 0.25$. Once the maximum steepness is reached, the local water particle velocity increases significantly in the "toe" region and eventually a jet is ejected from the crest. The jet then impacts the front face of the wave and entrains a large air cavity. The air entrainment and the splash-up of the overturning jet after impact is depicted in Figure 3.17(a). Several smaller structures ejected

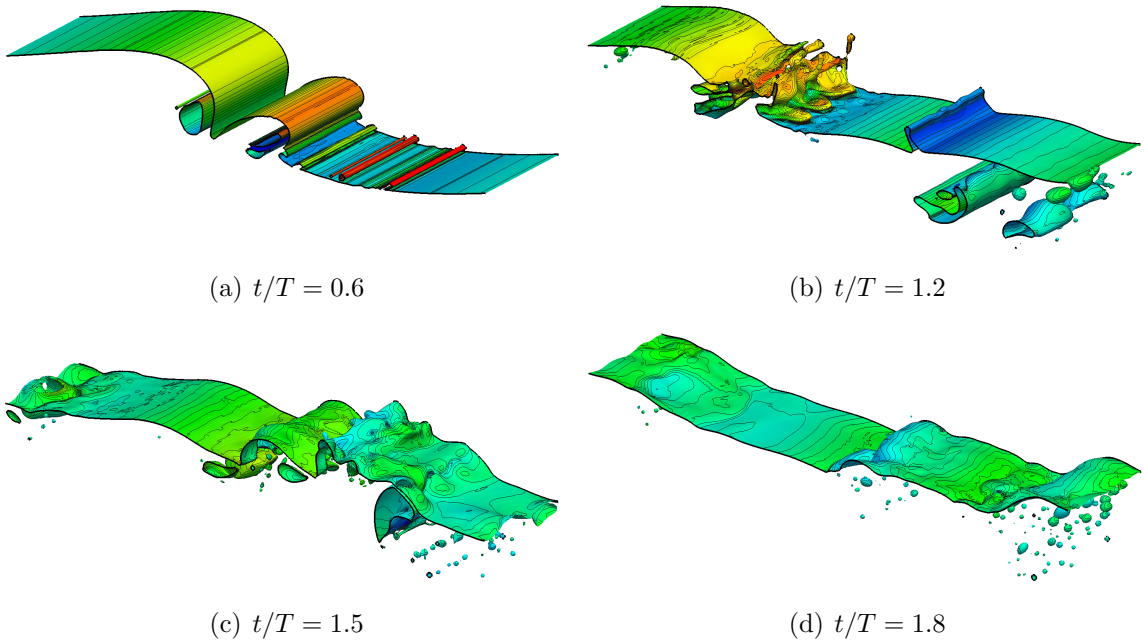

(a) $t/T = 0.6$ (b) $t/T = 1.2$

(c) $t/T = 1.5$ (d) $t/T = 1.8$

Figure 3.17: Free surface of the plunging-breaking wave colored by streamwise velocity

during the initial jet impact are shown to have a much larger streamwise velocity compared to the bulk flow. The majority of the water's initial energy is dissipated between $0.6 < t/T < 1.8$ through the breaking process. The initial stage of energy dissipation takes places while the flow is mostly two-dimensional. The development of three-dimensional interfacial structures is clearly visible in Figure 3.17(b) where filament-like jets are ejected after the bulk of the toe collapses. Additionally, the entrained air cavities which are initially two-dimensional, begin to break up into smaller three-dimensional structures. At $t/T = 1.8$ shown in Figure 3.17(d), only small air bubbles remain in the water once the largest air cavities break up or are

driven towards to the free surface by buoyancy. The major features of the breaking process including the toe formation, jet ejection and splash-up, and the exponential decay of the wave's energy is found to be reproduced well in the present simulation compared to the documented studies of plunging-breaking waves.

3.3.3 Quantification of the Subgrid Contributions

The subgrid contribution is now quantified for the plunging-breaking wave flow through the *a priori* approach. The *a priori* analysis of the direct numerical simulation data is conducted in the same consistent manner as previously shown for the phase-inversion problem. To the author's knowledge, this type of analysis of a plunging-breaking water wave has not been previously published.

The top-hat filter stencils are now three dimensional to account for the spanwise extent of the computational domain. The small filter uses a 3x3x3 stencil and the large filter uses a 5x5x5 stencil. The same four subgrid-scale terms are studied as in the phase-inversion problem of Section 3.2: τ_C, τ_D, τ_A, and τ_I. The contribution of each of the subgrid terms to the corresponding discretized governing equations is studied by quantifying the divergence of the spatial terms and the time derivative of the acceleration term ($\partial\tau_{Cij}/\partial x_j$, $\partial\tau_{Dij}/\partial x_j$, $\partial\tau_{Ai}/\partial t$, and $\partial\tau_{Ii}/\partial x_i$). The maximum of each subgrid contribution ($\partial{\tau_{ij}}^{max}/\partial x_i$ or $\partial{\tau_{ij}}^{max}/\partial t$) is computed at each sampled time for the duration of the simulation. The maxima are then non-dimensionalized by the largest resolved term in the corresponding governing equation. In the case of the momentum equation, the vertical component of the resolved convective acceleration $\partial\overline{\rho}\,\overline{u}_2\overline{u}_j/\partial x_j$ is used, whereas in the interface equation, $\partial\overline{u}_2\overline{\alpha}/\partial x_2$ is used for normalization of the subgrid contributions. The non-dimensionalize process follows the work of Larocque et al. (2010) and is consistent with the approach used for the phase-inversion *a priori* study.

The three normalized components of each studied subgrid term are plotted in

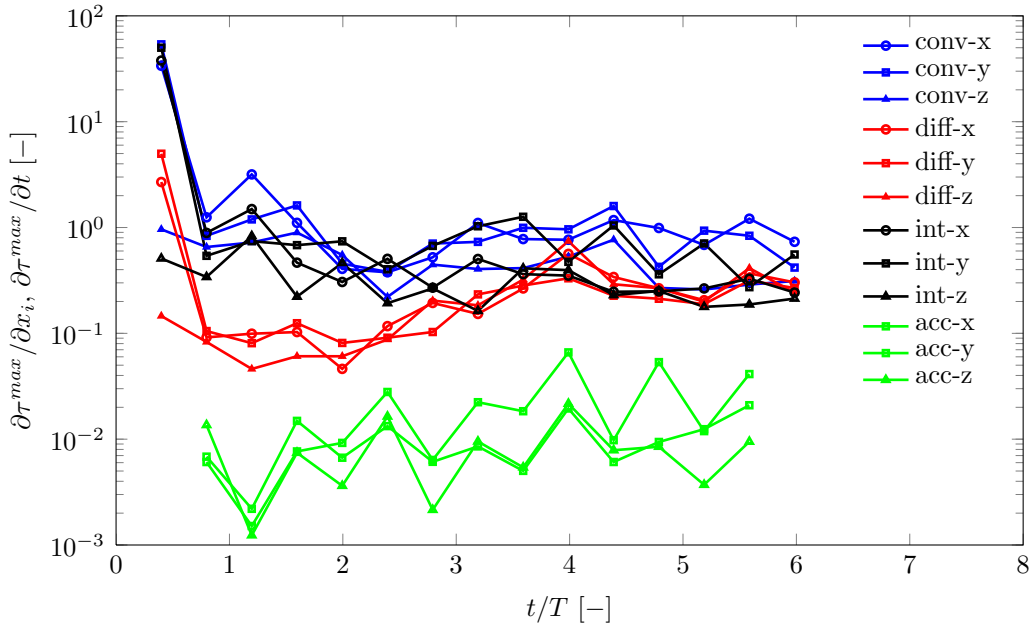

(a) Small filter: 3x3

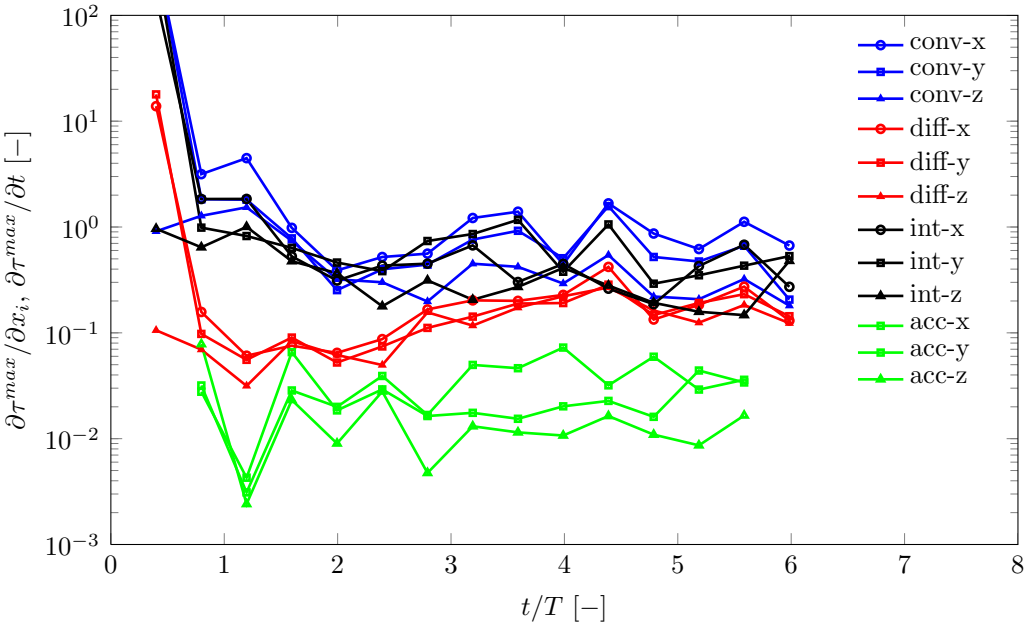

(b) Large filter: 5x5

Figure 3.18: Normalized maximum of the divergence / time derivative of the SGS terms

Figure 3.18 for both filter sizes. The most energetic stage of the wave-breaking process takes place between $0.4 < t/T < 2.4$. The most significant changes of the subgrid term contributions also occur during this time. The maximum of the convective and the interfacial SGS terms are found to be on the order of magnitude of the resolved contributions for the majority of the simulation, and to be the largest subgrid contributors at the time of breaking. The diffusive SGS term is much less active during the breaking process and it remains smaller than the convective SGS contribution at most instances in time. The acceleration subgrid term is once again found to have the smallest contribution to the momentum equation. It is worthwhile pointing out that Chesnel et al. (2011a) investigated this term's relative contribution for the spray-atomization problem and as a function of the order of the time-integration scheme used. The authors found that the relative contribution of the acceleration term was not affected by the order of the numerical scheme, and hence the order of the temporal scheme used in this work is unlikely to affect the term's magnitude.

At the first sampled time of $t/T = 0.4$, the streamwise and the vertical components of the convective, diffusive, and interfacial SGS terms dominate the corresponding resolved terms. The same trend is found when the larger grid filter is used as shown in Figure 3.18(b). The relatively small magnitude of the resolved convective terms in the momentum and interface equations at this point in the flow's development is responsible for the relative subgrid contributions. The normalized subgrid terms are drastically reduced at the next sampled time ($t/T = 0.8$) once the magnitude of the resolved terms increases with the evolution of the wave-breaking process. At the time of the jet splash-up and the formation of three-dimensional interfacial structures, the z-component of the interfacial SGS term becomes more important relative to the resolved interfacial component. Once the flow begins to settle and approaches a steady state after approximately $t/T = 4$, the magnitude of the spanwise components of the subgrid terms decreases.

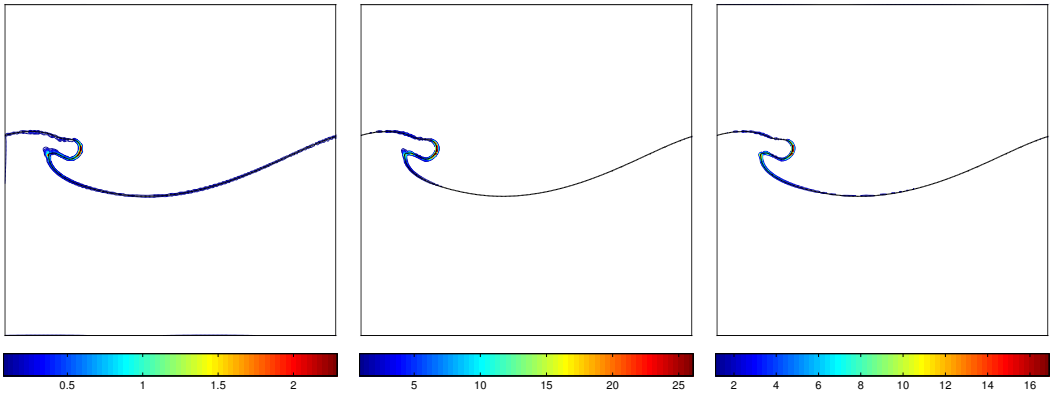

(a) $|\tau_D|$ at $t/T = 0.4$ (b) $|\tau_C|$ at $t/T = 0.4$ (c) $|\tau_A|$ at $t/T = 0.4$

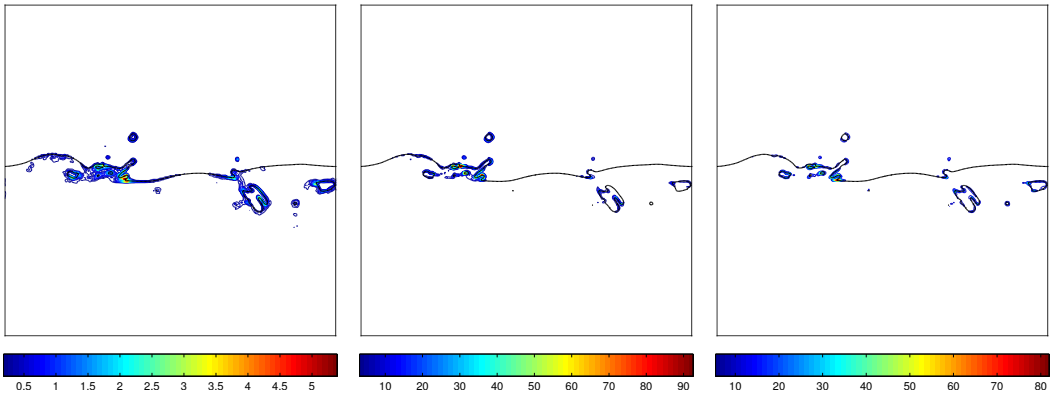

(d) $|\tau_D|$ at $t/T = 1.2$ (e) $|\tau_C|$ at $t/T = 1.2$ (f) $|\tau_A|$ at $t/T = 1.2$

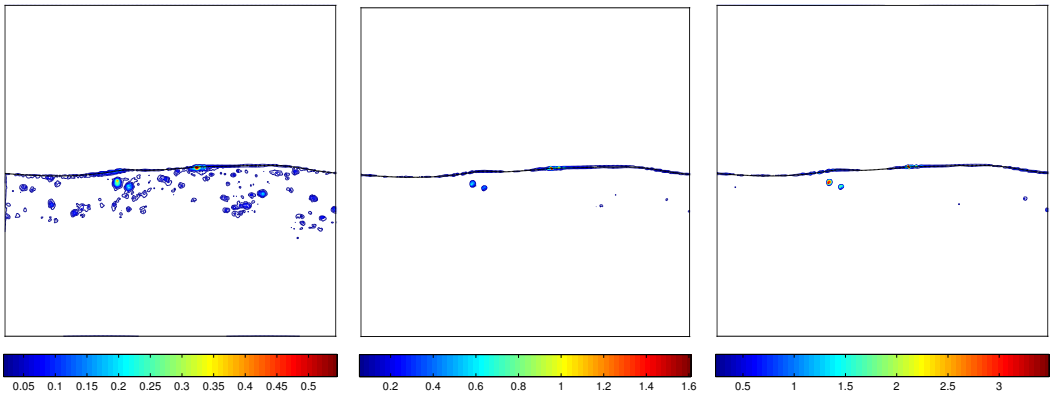

(g) $|\tau_D|$ at $t/T = 4.8$ (h) $|\tau_C|$ at $t/T = 4.8$ (i) $|\tau_A|$ at $t/T = 4.8$

Figure 3.19: Magnitude of the subgrid terms in the momentum equation using the small filter (3x3x3). Center-plane at $z = 0.5W$.

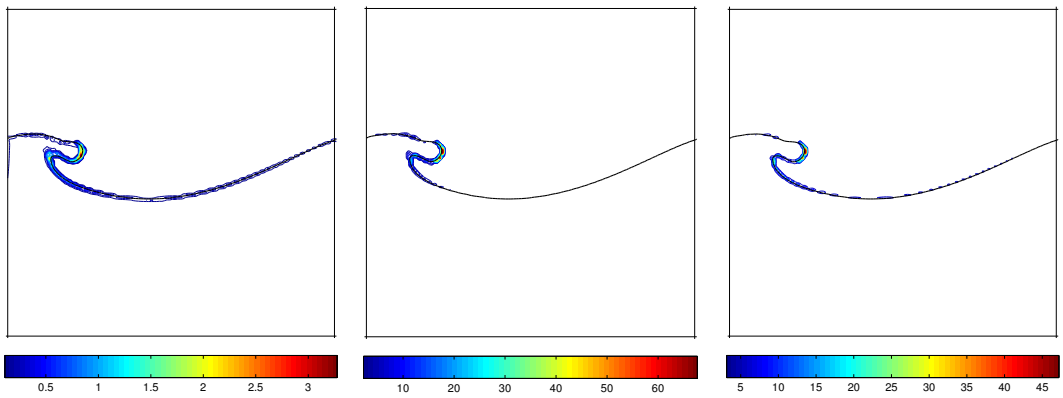

(a) $|\tau_D|$ at $t/T = 0.4$ (b) $|\tau_C|$ at $t/T = 0.4$ (c) $|\tau_A|$ at $t/T = 0.4$

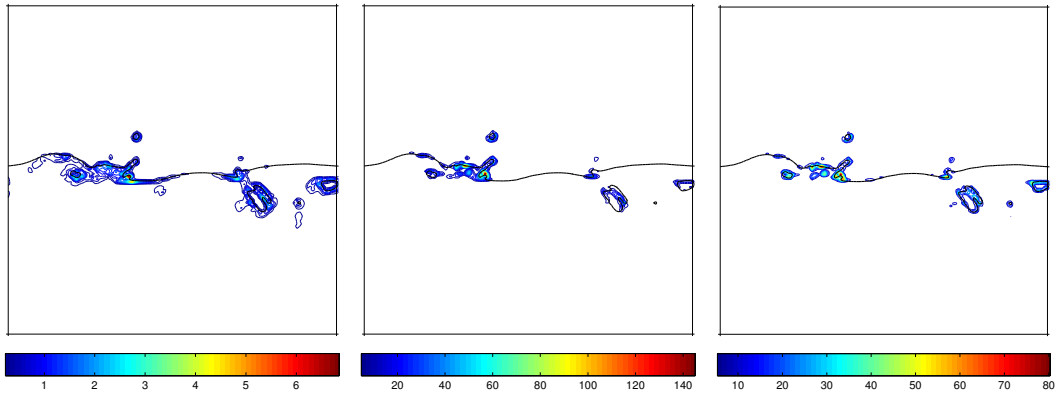

(d) $|\tau_D|$ at $t/T = 1.2$ (e) $|\tau_C|$ at $t/T = 1.2$ (f) $|\tau_A|$ at $t/T = 1.2$

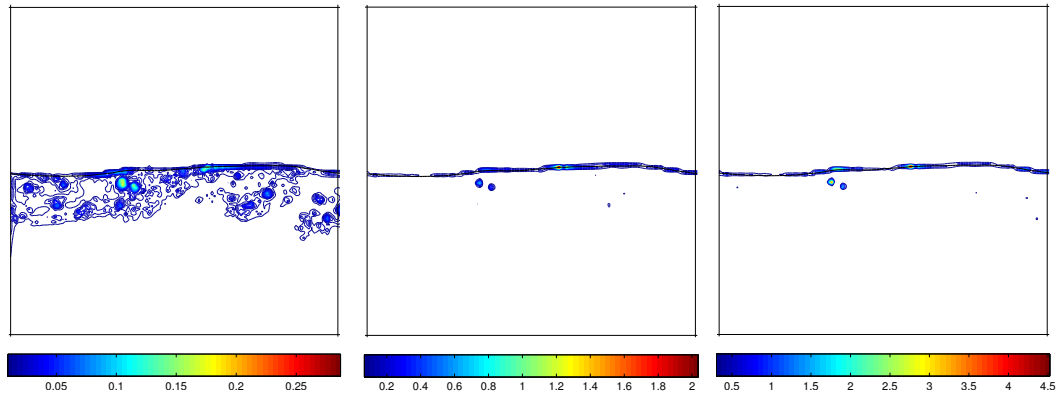

(g) $|\tau_D|$ at $t/T = 4.8$ (h) $|\tau_C|$ at $t/T = 4.8$ (i) $|\tau_A|$ at $t/T = 4.8$

Figure 3.20: Magnitude of the subgrid terms in the momentum equation using the large filter (5x5x5). Center-plane at $z = 0.5W$.

The overall subgrid contribution from the four terms tends to increase with the increase of the filter-cutoff length. The SGS terms tend to be highly localized near the interface, especially before the impact of the overturning jet. Large particle velocities in the toe region result in the subgrid terms becoming highly active in the early stages of the breaking process. The subgrid terms from the momentum equation (τ_C, τ_D, and τ_A) are visualized in Figure 3.19 on a center-plane of the computational domain at $z = 0.5W$ and using the small filter. Three instances in time are shown: before impact at $t/T = 0.4$, after impact at $t/T = 1.2$, and approaching steady-state at $t/T = 4.8$. The same instances in time are shown in Figure 3.20 for the 5x5x5 filter. The region over which the subgrid terms are active increases in size as the larger filter-cutoff length is used, but the majority of the subgrid presence is in close proximity to the free surface in both the before-impact and after-impact snapshots. The magnitudes of τ_C, τ_D, and τ_A are significantly reduced from their pre and post-breaking values as the flow approaches a steady state, indicating that the modeling approach for the largest subgrid contributors should be selected based on its ability to mimic the interaction of the resolved and subgrid scales during the most energetic stages of the flow.

Similar results are found for the subgrid interface term shown in Figure 3.21. The subgrid term activation is highly concentrated near the fluid interface and near small air and water droplets that cannot be resolved on the filtered grid. The magnitude of τ_I is found to increase together with the size of the filter stencil but similar magnitudes are found at $t/T = 1.2$ using both filters. The application of the larger filter spreads the influence of the subgrid term over a greater area, effectively smearing the flow information available at the grid level.

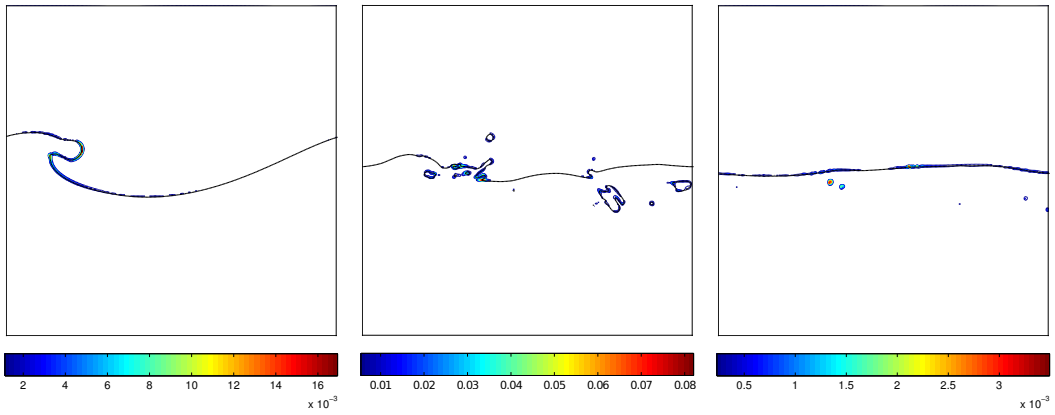

(a) SF, $t/T = 0.4$ (b) SF, $t/T = 1.2$ (c) SF, $t/T = 4.8$

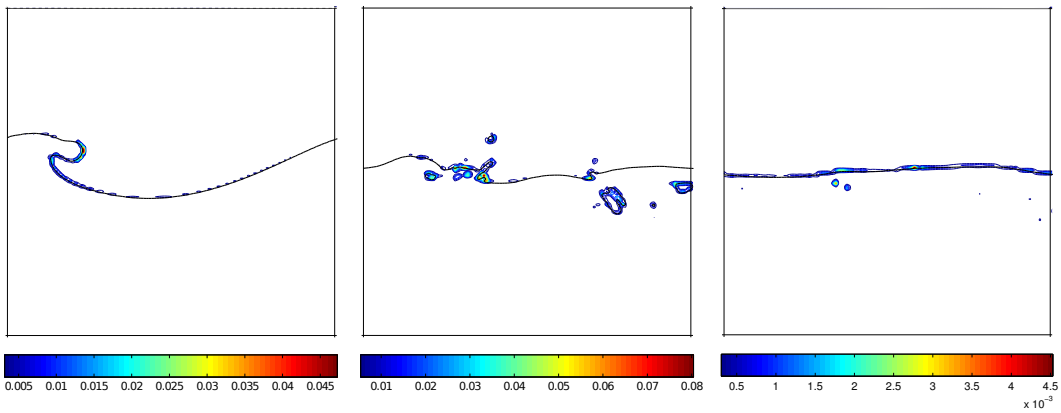

(d) LF, $t/T = 0.4$ (e) LF, $t/T = 1.2$ (f) LF, $t/T = 4.8$

Figure 3.21: Magnitude of the interface subgrid term $|\tau_I|$. Center plane at $z = 0.5W$.

3.3.4 Modeling of the Subgrid-Scale Terms

Several subgrid-scale modeling approaches are tested for their ability to model the interaction of the resolved and unresolved turbulent and interfacial structures for the breaking-wave problem. The same type of analysis was carried out for the phase-inversion problem in Section 3.2.2, where structural modeling based on the scale-similarity approach was found to yield promising correlation coefficients for the four studied subgrid terms. The breaking-wave flow presents new modeling challenges associated with the fluid-density ratio that is two orders of magnitude greater than in the oil-water phase-inversion problem. Additionally, the fluid-viscosity ratio is greater and the subgrid terms are typically more localized than in the phase-inversion problem.

The convective SGS stress tensor τ_C is modeled using the dynamic Smagorinsky, the scale-similarity, and the stress-similarity models. The original scale-similarity model is compared to the stress-similarity model to investigate the role of the filter-cutoff length used in the secondary filtering procedure. The two similarity-based models and the dynamic eddy-viscosity model are again used as proxies for the mixed SGS model. The stress-similarity concept is extended to the modeling of the diffusive, the acceleration, and the interfacial subgrid-scale terms. The performance of each model is evaluated based on the correlation coefficient between the true subgrid stress and the output of the model (see Equation 3.9).

The correlation coefficients of the three models used for the convective SGS stress are shown as a function of simulation time in Figure 3.22. Contrary to the findings of the phase-inversion study, the similarity-based models are not found to out-perform the dynamic Smagorinsky model by a large margin. The correlation coefficients of the three models are comparable for most of the sampled instances in time. A particular exception is found at $t/T = 0.8$ when the small filter stencil is used. At this time, the overturning jet has already made contact with the front face of the wave resulting in

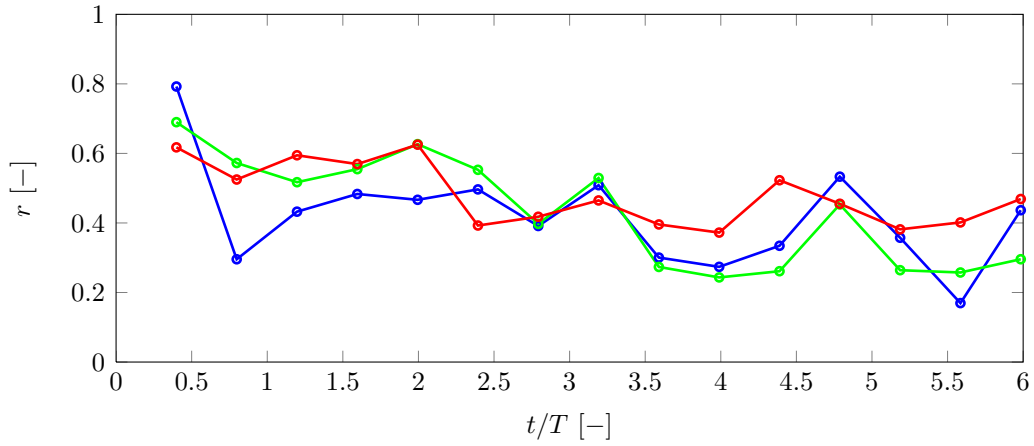

(a) Small filter: 3x3

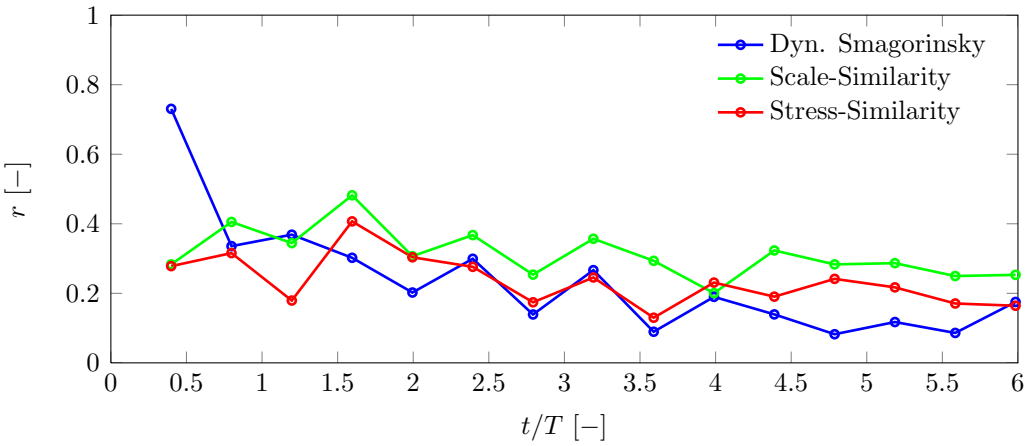

(b) Large filter: 5x5

Figure 3.22: Correlation coefficient for the convective SGS stress magnitude

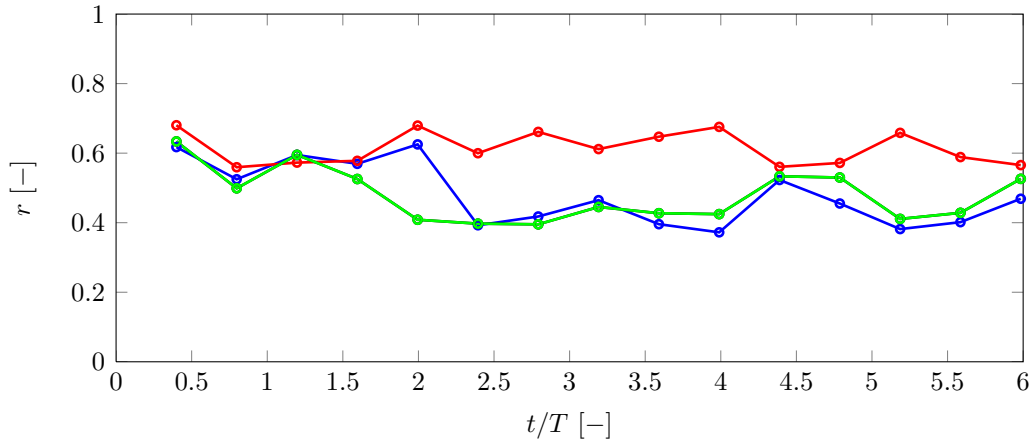

(a) Small filter: 3x3

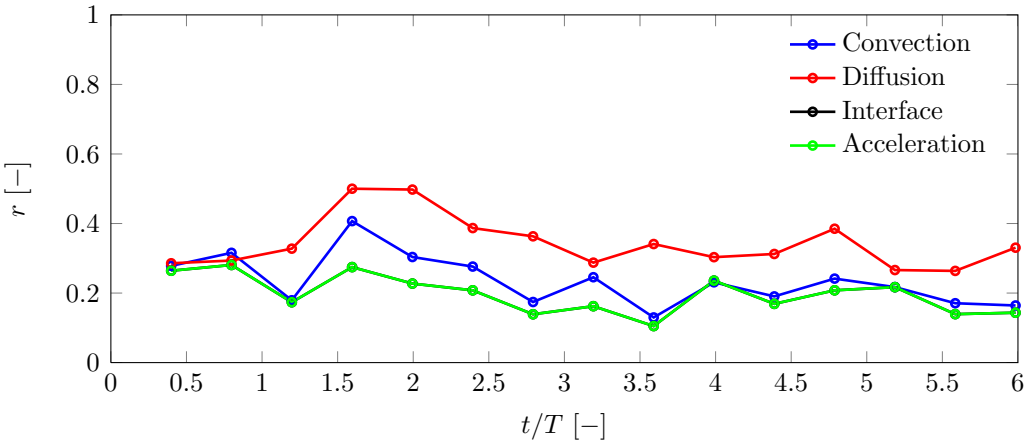

(b) Large filter: 5x5

Figure 3.23: Stress-similarity correlation coefficient for the convective, diffusion, acceleration, and interface SGS term magnitudes. Centerline plane at z = 0.5W.

the formation of complex interfacial structures. The introduction of these structures complicates the spatial variation of the fluid properties that are used in the dynamic coefficient calculation of the eddy-viscosity model. The dynamic procedure breaks down because of the built-in assumption of small variations between the grid and test levels. During the most important stages of wave breaking ($0.4 < t/T < 2.4$), the similarity-based models give an average correlation coefficient of approximately 0.55.

The correlation coefficients calculated using the data filtered with the 5x5x5 stencil are reduced compared to the small-filter results just as in the phase-inversion problem. The three tested models behave similarity throughout the simulated time period and the correlation coefficients are reduced by approximately 50% compared to the small filter results. The same trend is observed in Figure 3.23 where the correlation coefficients for the convective, diffusive, acceleration, and interfacial SGS terms are shown. The interface and acceleration terms have the same correlation coefficients due to the coupling between the density and volume fraction fields (see Section 3.2.2 for details). The diffusive term shows the best correlation for both filter sizes with a time-average value of approximately $r = 0.6$. The performance of the stress-similarity model for the other subgrid terms is somewhat worse with a time-average of $r \approx 0.5$ using the small filter. The model's performance is degraded by approximately 30 to 50% by the use of the larger filter in the *a priori* analysis.

The reduction in the correlation is investigated in more detail by examining the magnitudes of the true subgrid interfacial behavior $|\tau_I|$ and the modeled contribution $|\tau_I{}^*|$ based on the stress-similarity formulation. The same three instances in time (before and after impact, and approaching steady-state) are selected and the contours of the terms obtained using the small filter are shown in Figure 3.24 on the center-plane of the domain.

Before the overturning jet makes contact with the wave's front face, the magnitude of the modeled-subgrid term is approximately two to three times greater than

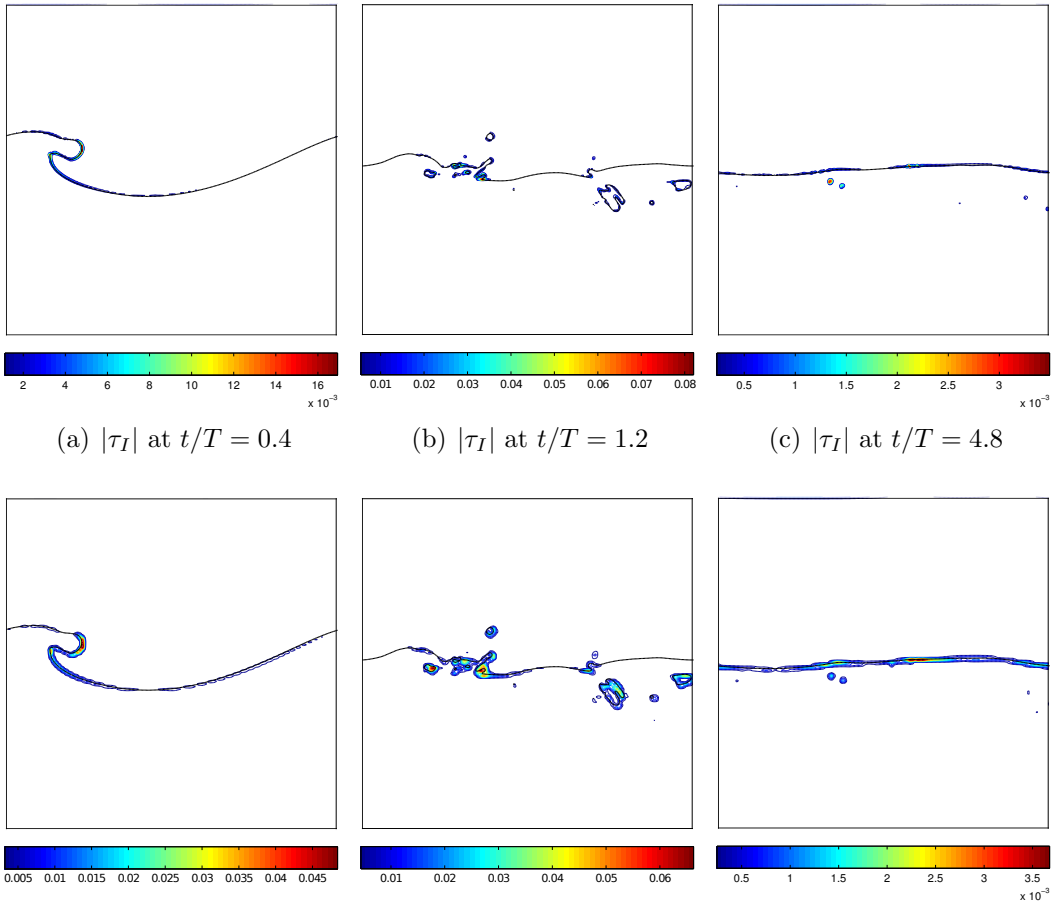

(a) $|\tau_I|$ at $t/T = 0.4$ (b) $|\tau_I|$ at $t/T = 1.2$ (c) $|\tau_I|$ at $t/T = 4.8$

(d) $|\tau_I{}^*|$ at $t/T = 0.4$ (e) $|\tau_I{}^*|$ at $t/T = 1.2$ (f) $|\tau_I{}^*|$ at $t/T = 4.8$

Figure 3.24: Magnitude of the true interface subgrid term $|\tau_I|$ and the modeled contribution $|\tau_I{}^*|$ using the stress-similarity approach. Small filter (3x3) and $C_I = 1$.

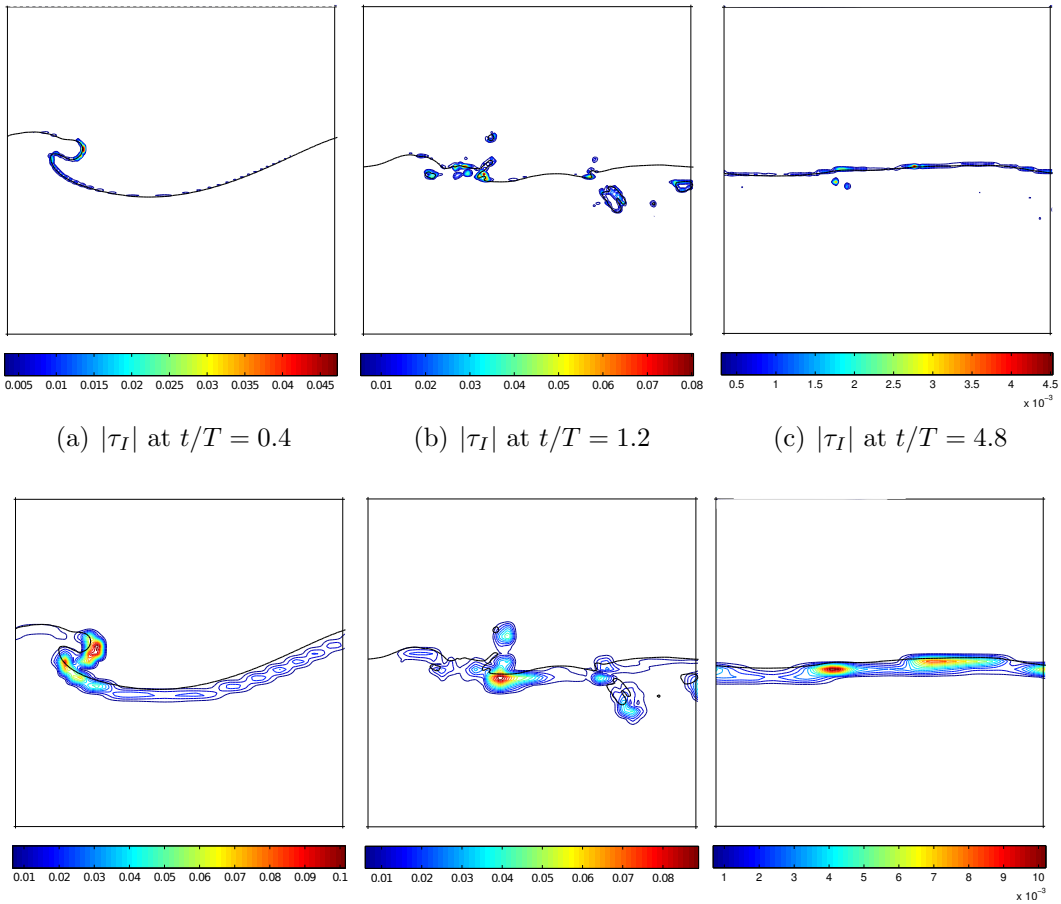

(a) $|\tau_I|$ at $t/T = 0.4$ (b) $|\tau_I|$ at $t/T = 1.2$ (c) $|\tau_I|$ at $t/T = 4.8$

(d) $|\tau_I{}^*|$ at $t/T = 0.4$ (e) $|\tau_I{}^*|$ at $t/T = 1.2$ (f) $|\tau_I{}^*|$ at $t/T = 4.8$

Figure 3.25: Magnitude of the true interface subgrid term $|\tau_I|$ and the modeled contribution $|\tau_I{}^*|$ using the stress-similarity approach. Large filter (5x5) and $C_I = 1$.

$|\tau_I|$. The same trend of over-estimating the subgrid contribution using the similarity approach with two different filter-cutoffs was found in the phase-inversion study, especially in the early stages of the flow development. The spatial distribution of the peak subgrid contribution is reproduced by the model at $t/T = 0.4$, but with greater spreading across the interface region due to the size of the test-filter stencil. The modeled term is found to match the magnitude of the true subgrid term at $t/T = 1.2$. At this point, the jet has already impacted the front face of the wave and several air cavities are entrained below the free surface. Addtionally, water droplets of various sizes are propelled into the air with large horizontal velocities. The model for the subgrid interfacial term is found to be highly active near the splash-up region and in the proximity of the entrained air cavities. The influence of the model extends beyond the region where the true subgrid term is confined to, resulting in the relative low correlation coefficients shown in Figure 3.23(a).

The correlation of the stress-similarity models was found to degrade further with the use of the larger stencil. This behavior is explained by the contours of the modeled interfacial SGS contribution shown in Figure 3.25. The large test-filter-cutoff length-scale spreads the influence of the model over a much greater region compared to the true subgrid term. The size of the test filter is selected to be twice the size of the grid filter based on the findings of previous *a priori* studies of various canonical turbulent flows. However, the results presented here indicate that the ratio of the test-to-grid filter needs to be examined in greater detail for interfacial flows where the turbulent structures of interest are confined to the regions proximal to the fluid interface.

3.4 Summary

This chapter presents the highly-resolved simulations of two canonical turbulent-interfacial flows and the *a priori* analysis of the subgrid-scale terms. The method

of quantifying the subgrid contributions is validated against published results of a fully-developed turbulent channel flow and the phase-inversion problem. Then, the subgrid terms are analyzed for the problem of a three-dimensional plunging-breaking wave. The relative maximum contributions of the convective and the interfacial SGS terms are on the order of the resolved counterparts during the most energetic stages of the wave breaking process. Several modeling techniques of the subgrid-scale behavior are examined by comparing the true subgrid terms versus the output of the models. The structural type of SGS modeling is found to be highly correlated with the true subgrid stresses, but the correlation coefficients tend to be strongly affected by the size of the grid and test-level filters.

CHAPTER 4

Large-Eddy Simulations of Turbulent Interfacial Marine Flows

In this chapter, important turbulent-interfacial flows are studied with large-eddy simulations. The stress-similarity-based model for the multiphase SGS terms is implemented into the LES solver. The phase inversion and the plunging-breaking wave problems are studied *a posteriori* to understand the role of the SGS terms in practice. The results from the *a priori* study are used as a basis for the selection the SGS terms that are modeled. Furthermore, the problem of steep and breaking waves impinging on a circular cylinder piercing the air-water interface is studied. The in-line force on the cylinder and the prediction of the free-surface elevation in the proximity of the structure are examined using several subgrid-scale modeling approaches.

The *a priori* findings from Chapter 3 require further examination through the *a posteriori* study using actual large-eddy simulations with implemented closure models. The correlation coefficients for various subgrid-scale stress models obtained *a priori* have been shown to not necessarily indicate the quality of the LES results (Park et al. (2005)). In fact, high correlation between the true subgrid-scale stress calculated from DNS data and the modeled subgrid-scale stress may not be sufficient to guarantee the model's performance in actual large-eddy simulations. Furthermore, the *a priori* analyses compare the maxima of the subgrid terms that are found to vary significantly in magnitude as a function of space and time and thus the conclu-

sions drawn from the *a priori* study may not translate directly to practical large-eddy simulations.

Several flow quantities including kinetic energy and its dissipation rate are computed from the large-eddy simulations and compared to the direct numerical simulations results where possible. Experimental data is used for validation for the cylinder in waves problem. The performance of the selected closure models applied to the simulation of the three interfacial flows is then summarized.

4.1 Modeling Multiphase Subgrid Contributions

The stress-similarity model is selected to approximate the subgrid behavior of the interfacial, acceleration, and diffusive SGS terms defined in Section 2.3.1. The model selection is justified through the *a priori* study and also based on published studies that utilize the stress-similarity concept to model non-traditional LES terms such as the subgrid scalar transport (Chumakov (2005)). The convective SGS stress is modeled using the dynamic Smagorinsky model and the mixed model of Zang et al. (1993) as implemented by the University of Rostock LeMoS research group (see for example Kornev et al. (2006)). The details of the convective models are discussed in Section 2.2.2.

The SGS terms associated with the presence of the fluid interface are modeled as follows:

$$\tau_{I_i}^* = C_I \left(\widehat{\overline{u}_i \, \overline{\alpha}} - \widehat{\overline{u}}_i \, \widehat{\overline{\alpha}} \right), \tag{4.1}$$

$$\tau_{A_i}^* = C_A \left(\widehat{\overline{\rho} \, \overline{u}_i} - \widehat{\overline{\rho}} \, \widehat{\overline{u}}_i \right), \tag{4.2}$$

$$\tau_{D_{ij}}^* = C_D \left(\widehat{M} - N \right), \tag{4.3}$$

where

$$M = \overline{\mu} \left(\frac{\partial \overline{u}_i}{\partial x_j} + \frac{\partial \overline{u}_j}{\partial x_i} \right) \tag{4.4}$$

$$N = \widehat{\overline{\mu}} \left(\frac{\partial \widehat{\overline{u}}_i}{\partial x_j} + \frac{\partial \widehat{\overline{u}}_j}{\partial x_i} \right) \tag{4.5}$$

and the star superscript indicates a modeled quantity. The test-level filtering uses a top-hat filter that is effectively twice the size of the implicit grid filter ($\widehat{\overline{\Delta}}/\overline{\Delta} = 2$). The model coefficients are initially set equal to one as recommended by Liu et al. (1994) and based on the findings of Cook (1997) who reported that in single-phase flows, the stress-similarity coefficient is relatively insensitive to the turbulent Reynolds number and the ratio of the test-to-grid filter. The *a priori* results in Chapter 3 indicate that the stress-similarity coefficients may need to be adjusted for the two multiphase flows studied here. In an effort to reduce the number of factors affecting the *a posteriori* analysis, the coefficients are held constant and they are not adjusted based on the correlation coefficients reported in the *a priori* results.

The modeled terms are implemented in OpenFOAM and are discretized in the same manner as the resolved counterparts.

4.2 Phase Inversion

The two-dimensional phase-inversion problem previously studied *a priori* in Section 3.2 is now examined using large-eddy simulations. Several models for the convective subgrid-scale stress are tested *a posteriori* together with the stress-similarity model for the interfacial and diffusive SGS terms. The maxima of the interfacial and diffusive SGS terms were identified as significant contributors to the corresponding filtered governing equations. The magnitude of the interfacial term was found to increases rapidly as the size of the filter is increased or effectively when a coarser LES grid is used. Two LES grids are used to examine the effects of the grid refinement on the models' ability to predict the global flow quantities of interest. Kinetic energy and its dissipation rate integrated over the entire domain and in each phase are the focus of the analysis because an accurate prediction of these flow quantities is critical

for modeling of the evolution of turbulent flow.

The time evolution of the domain or phase-integrated total kinetic energy KE is examined first. The kinetic energy is summed over the volume of the entire computational domain V or the individual phase V_α to obtain:

$$KE = \int_V \overline{\rho} \left(\frac{\overline{u}_i \, \overline{u}_i}{2} + k_{\text{sgs}} \right) \, \mathrm{d}V. \tag{4.6}$$

The total kinetic energy incorporates the subgrid-scale turbulent kinetic energy k_{sgs} approximated by the SGS model and the kinetic energy of the resolved scales $k_r = \overline{u}_i \overline{u}_i / 2$. Similarly, the kinetic energy dissipation rate ϵ combines the resolved dissipation rate ϵ_r and the SGS contribution:

$$\epsilon = \int_V \left(\nu \frac{\partial \overline{u}_i}{\partial x_j} \frac{\partial \overline{u}_i}{\partial x_j} + \epsilon_{\text{sgs}} \right) \, \mathrm{d}V \tag{4.7}$$

where the SGS dissipation rate is responsible for the energy transfer between the unresolved and the resolved scales and is modeled as $\epsilon_{\text{sgs}} = -\tau_{ij} \overline{S}_{ij}$ for zero-order closure models (Chumakov (2005)).

The two grids used to conduct large-eddy simulations of the phase-inversion problem are uniform in both spatial directions. The coarse grid (C) consists of 191^2 or 36,481 cells and the medium grid (M) contains 383^2 or 146,689 computational cells (see Table 3.2). The two selected grids correspond to the application of a 5x5 and a 3x3 filter stencil in the previous *a priori* study, respectively. The same discretization and numerical integration is used as in the case of the direct numerical simulations of the phase-inversion problem discussed in Section 3.1. The convective SGS stress tensor is modeled using the dynamic Smagorinsky model (DSMAG) that clips the effective eddy-viscosity at zero, and the dynamic mixed model (DMM). The stress-similarity model with constant model coefficients is used for both the interfacial (INT) and the diffusive (DIFF) SGS terms.

4.2.1 Total Kinetic Energy

The non-dimensional domain-integrated kinetic energy as a function of time and grid resolution is shown in Figure 4.1 for interfacial or diffusive SGS modeling only. The convective SGS stress tensor is not modeled at this point and the results obtained on the coarse and medium grids without any subgrid-scale stress modeling are included for reference. The coarse grid with no turbulence modeling over-predicts the peak kinetic energy in the domain as well as in the latter less-energetic stages of the simulation. The medium grid with no turbulence modeling reproduces the peak kinetic energy near $t = 13\ s$ but fails to capture the secondary peak near $t = 23\ s$ and the magnitude of the kinetic energy between approximately $20\ s < t < 60\ s$. The introduction of the interfacial SGS model on the coarse grid results in an improved prediction of the less-energetic stages of the flow. In the case of the medium grid, the interfacial term fails to improve the prediction significantly. The diffusive SGS model provides a similar improvement on the coarse grid as the interfacial term but results in a large over-prediction of the kinetic energy on the medium grid after $t = 60\ s$. The relatively poor performance of the simulations without modeling of the convective SGS stress are expected because the interfacial and the diffusive stress-similarity models alone are not sufficient to model the appropriate behavior of the energy cascade (Chesnel et al. (2011b)).

Figure 4.2 shows the non-dimensional domain-integrated kinetic energy for several combinations of the convective, interfacial, and the diffusive SGS modeling. Figure 4.2(a) plots the results obtained with the dynamic Smagorinsky model as the convective SGS stress model while Figure 4.2(b) plots the results with the dynamic mixed model. The dynamic Smagorinsky model improves the prediction of the kinetic energy on the coarse grid after $t = 50\ s$ compared to the no-model simulation, but the convective model offers no measurable improvement on the medium grid. The addition of the interfacial model to the dynamic Smagorinsky model proves to

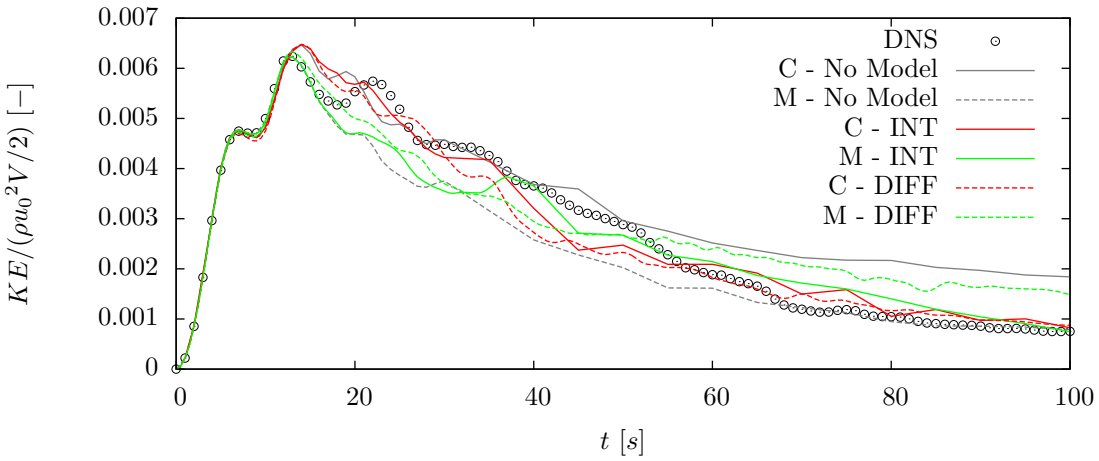

Figure 4.1: Total kinetic energy of the phase inversion simulation with interfacial or diffusive SGS modeling only

be ineffective in improving the results on the medium grid. On the coarse grid, the DSMAG+INT combination results in an over-prediction of the latter stages of the domain-integrated kinetic energy. The dynamic mixed model results show an overall improvement over the dynamic Smagorinsky results, especially after approximately $t = 60\ s$. The dynamic mixed model proves to be more robust for varying grid resolutions because the results from both the coarse and the medium grid with DMM only are very similar. The addition of the interfacial and the diffusive SGS modeling to DMM yields slight improvements on the coarse grid while on the medium grid the additional terms degrade the performance of the dynamic mixed model.

Because of the insufficient spatial resolution of the coarse mesh, the test-filtering procedure for the interfacial stress-similarity model breaks down and gives poor estimation for the subgrid behavior. At this level of grid refinement the test-filtering procedure uses under-resolved interfacial features that poorly reflect the true subgrid behavior. On the medium grid, the interface features are resolved with greater detail but the contribution of the interfacial SGS model is not sufficient to provide a significant improvement in the prediction of the flow compared to the DNS data. The magnitude of the interfacial SGS term contribution $\partial\tau_{Ii}/\partial x_i$ modeled with the stress-

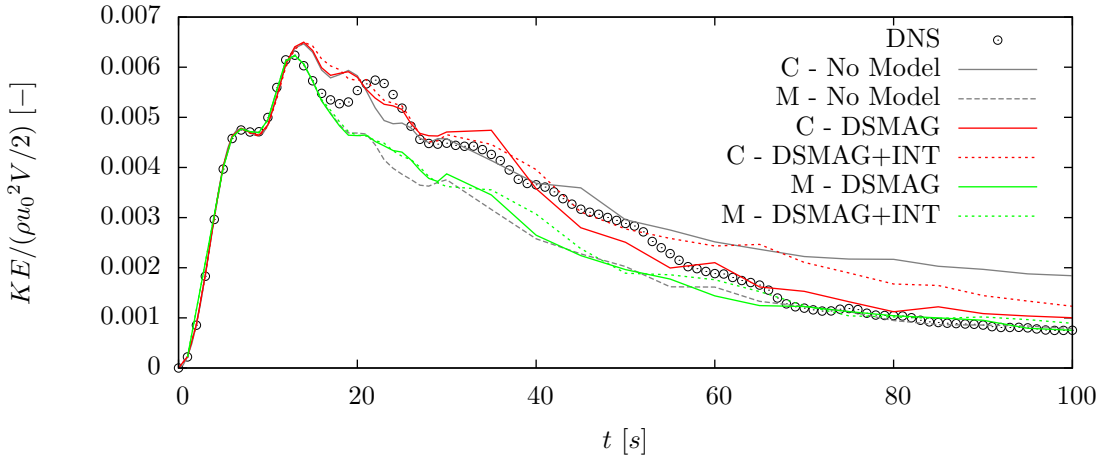

(a) Dynamic Smagorinsky Model

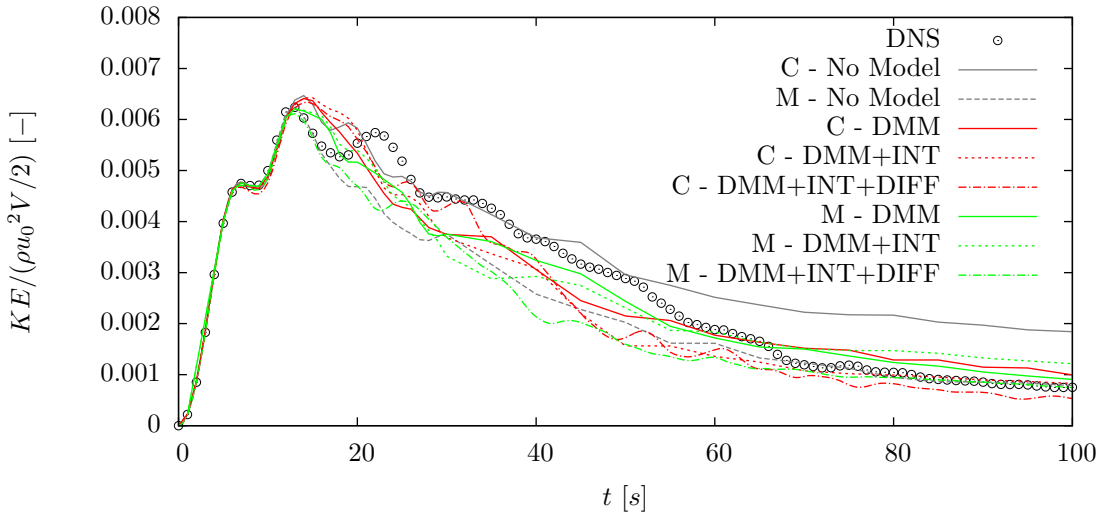

(b) Dynamic Mixed Model

Figure 4.2: Total kinetic energy of the phase inversion simulation with interfacial and convective SGS modeling

similarity concept is shown in Figure 4.3 on both LES grids. The model's contribution on the medium grid reaches 1% of the resolved term in small localized regions of the interface. This behavior was found in the *a priori* study and is also verified through the *a posteriori* analysis. A dynamic adjustment of the stress-similarity coefficient for the interfacial subgrid-scale model appears to be necessary in order to improve the model's performance on sufficiently-resolved LES grids.

Figure 4.4 depicts the kinetic energy integrated over only the water phase or where $0.99 \leq \alpha \leq 1$ and without the interfacial SGS modeling. The influence of interface on the performance of the selected SGS models is partially removed in this analysis to study the models' performance away from the turbulent water-oil interface. The dynamic Smagorinsky model results on the coarse grid match the DNS data for the majority of the simulation but the model is unable to correctly predict the most energetic stage of the flow development between $15\ s < t < 20\ s$. The results from the medium grid during the same time interval show a slight under-prediction of the kinetic energy in water followed by a significant under-prediction between $20\ s < t < 55\ s$. The results using the dynamic mixed model by itself and combined with the diffusive SGS model are shown in Figure 4.4(b). The mixed model is again found to be more robust for different grid resolutions compared to the dynamic Smagorinsky model because of the addition of the scale-similarity contribution which reduces the model's dependence on the eddy-viscosity component. The medium grid results are improved over the DSMAG simulations while the addition of the diffusive model to DMM on the coarse grid yields an improvement in prediction of KE in water between $20\ s < t < 35\ s$.

4.2.2 Kinetic Energy Dissipation Rate

The selected models are now examined for their ability to simulate the correct energy transfer process between the resolved and subgrid scales by examining the kinetic

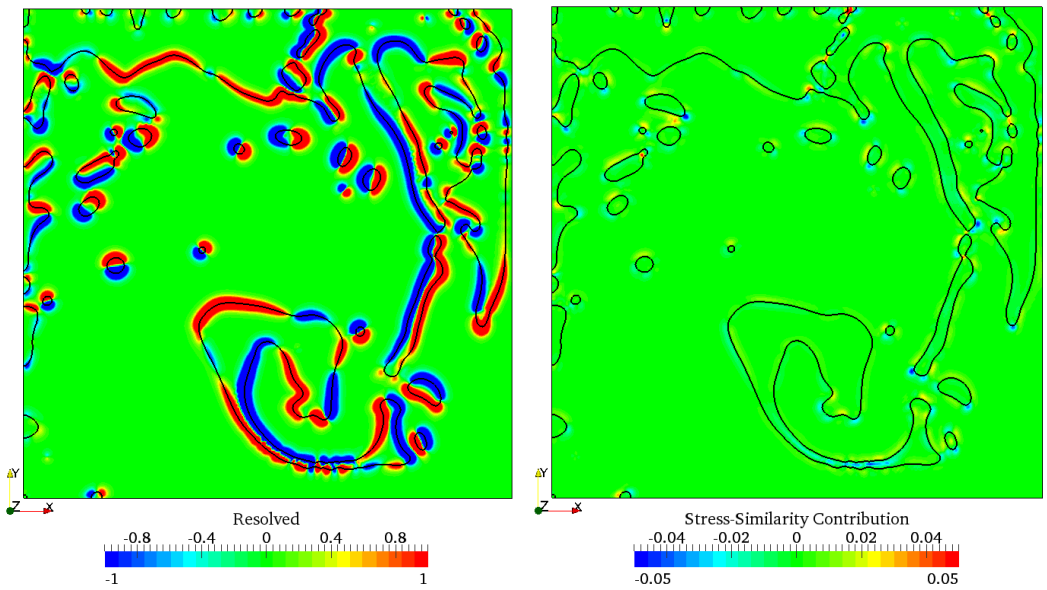

(a) M - DMM+INT

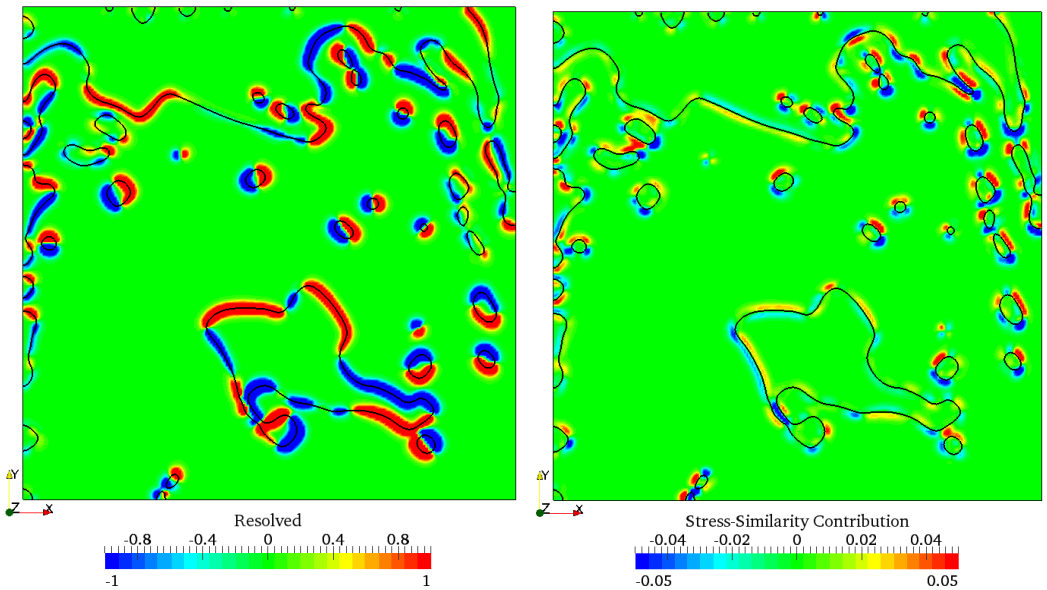

(b) C - DMM+INT

Figure 4.3: Maximum resolved component of the interface equation and the corresponding interfacial stress-similarity model contribution at $t = 17\ s$

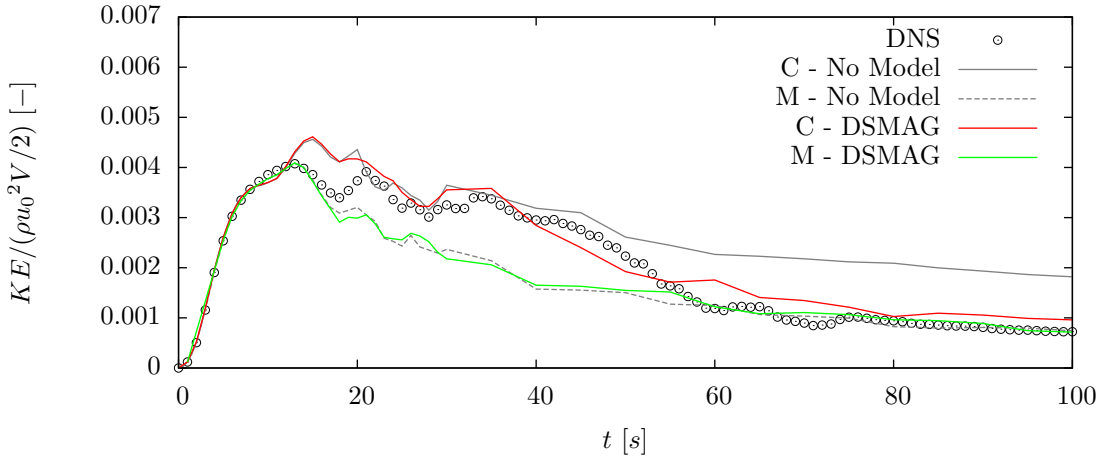

(a) Dynamic Smagorinsky Model

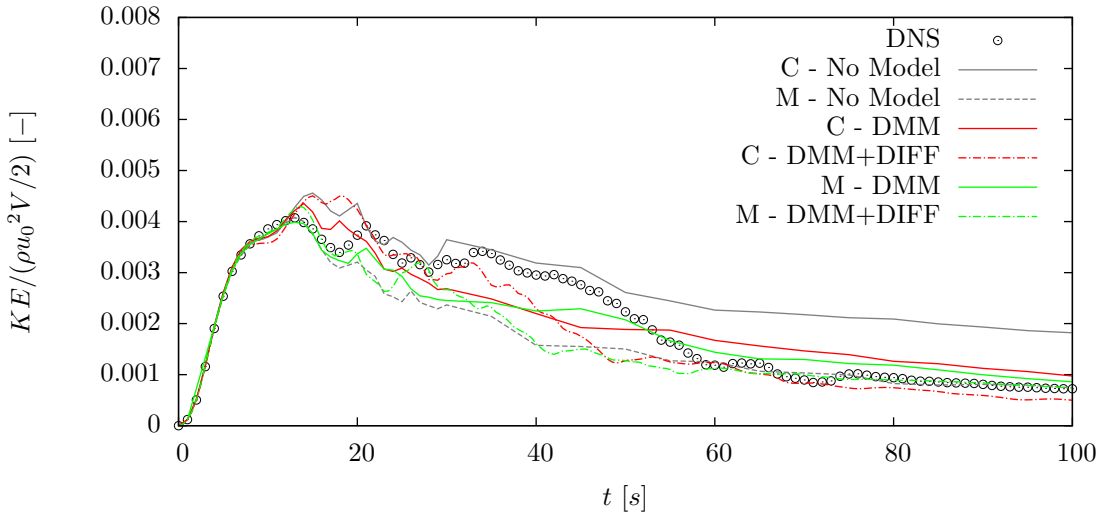

(b) Dynamic Mixed Model

Figure 4.4: Kinetic energy in water for the phase inversion simulation with interfacial and convective SGS modeling

energy dissipation rate integrated over the computational domain.

Figure 4.5 shows the results for interfacial and diffusive SGS modeling only without consideration for the convective term. In these simulations, the emphasis is placed on the resolved kinetic energy dissipation rate because of the lack of an eddy-viscosity model responsible for the subgrid dissipation. The first peak in the dissipation rate near $t = 7\ s$ is accurately reproduced in all simulations because at this time the flow is mostly laminar and the interface is relatively undisturbed. The global maximum is correctly predicted in magnitude on both grids, but its time of occurrence matches the DNS results only on the medium grid using the diffusive SGS stress-similarity model. The increase in the dissipation rate between $55\ s < t < 70\ s$ is not captured on either grid.

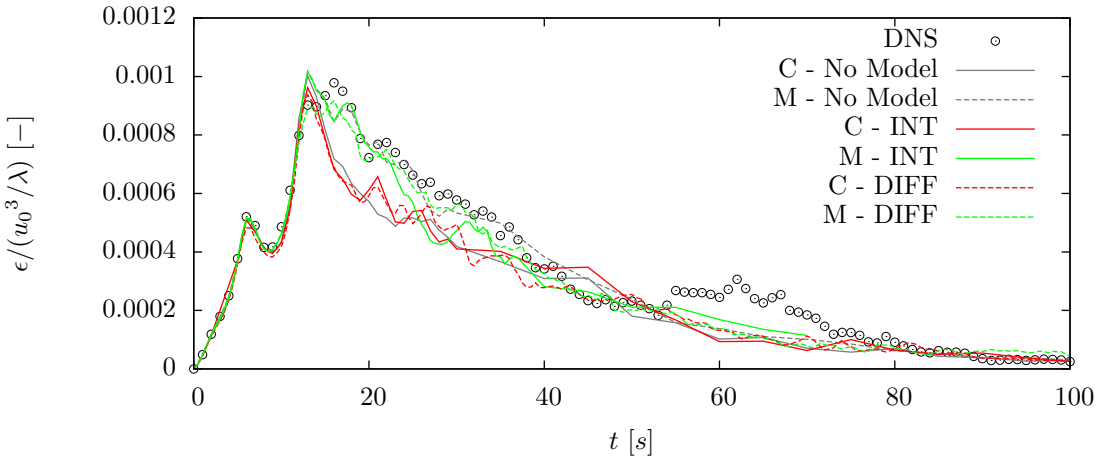

Figure 4.5: Kinetic energy dissipation rate for the phase inversion simulation with interfacial or diffusive SGS modeling only

The results with the convective SGS models are shown in Figure 4.6. The dynamic mixed model results on the medium grid correctly predict the time and magnitude of the peak dissipation rate occurrence, whereas the maximum occurs too early on the coarse grid and the addition of interfacial or diffusive SGS modeling does not improve the result. The differences between the coarse and medium grids using DMM are smaller than for DSMAG, but between $20\ s < t < 40\ s$ the dynamic Smagorinsky

model on the medium grid gives the best prediction of the domain-integrated dissipation rate. The various combinations of the convective, interfacial, and diffusive SGS modeling do not offer a significant improvement over just modeling of the convective subgrid-scale stress tensor. These results are similar to the analysis of the kinetic energy results shown previously.

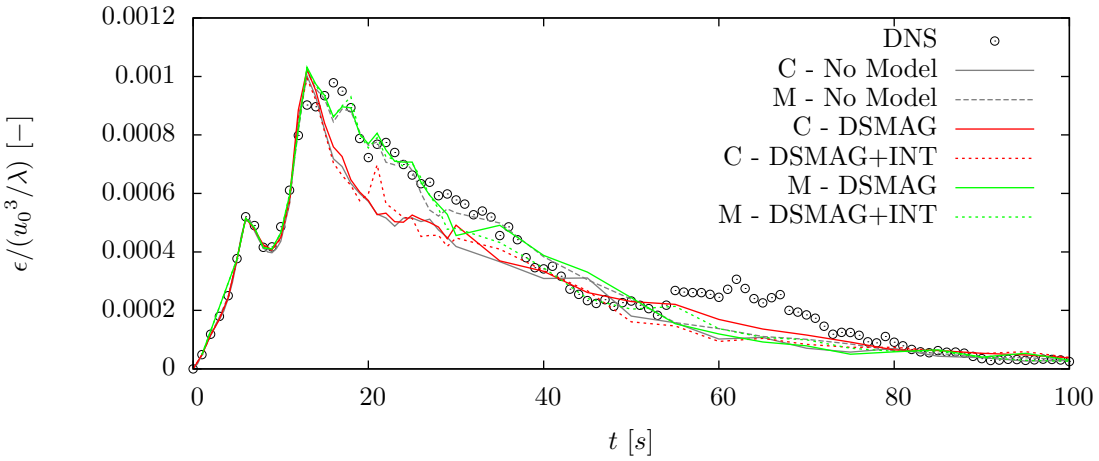

(a) Dynamic Smagorinsky Model

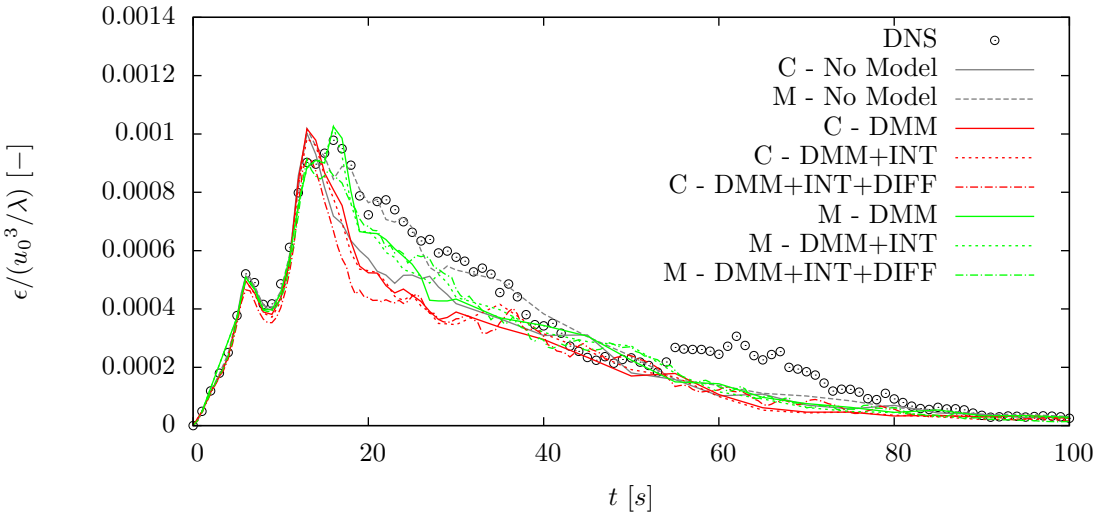

(b) Dynamic Mixed Model

Figure 4.6: Kinetic energy dissipation rate for the phase inversion simulation with interfacial, diffusive, and convective SGS modeling

The fully-resolved direct numerical simulation results for the maximum dissipation rate at $t = 17\ s$ are shown in Figure 4.7(a). Local dissipation rate maxima are found

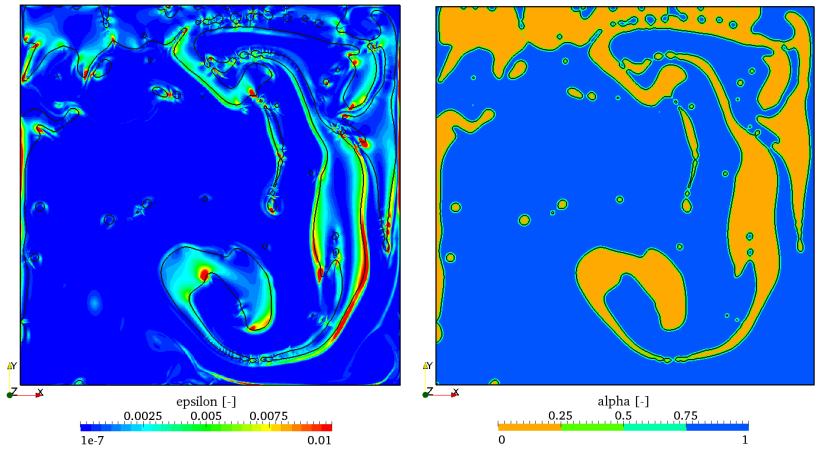

(a) DNS

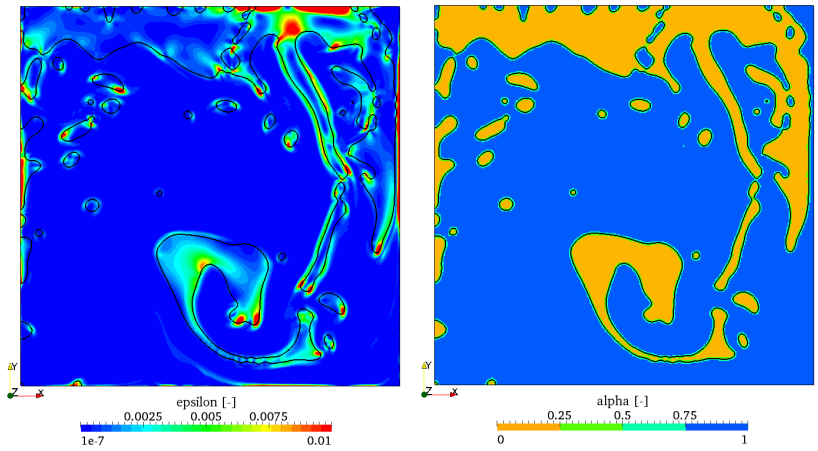

(b) M - DMM+INT

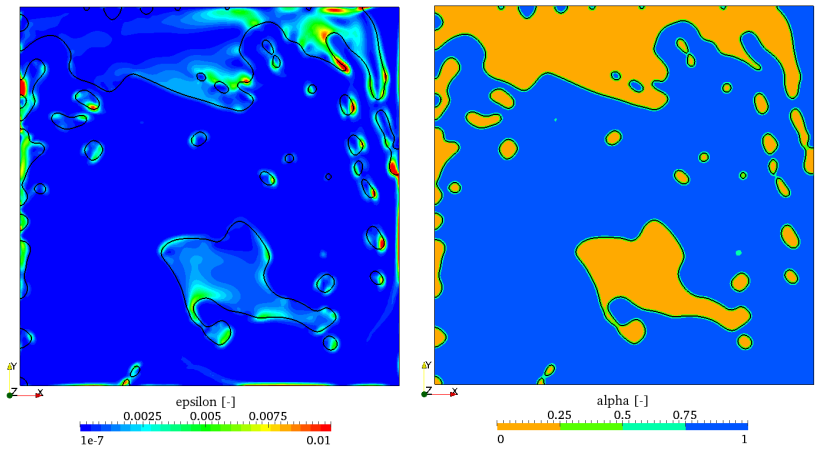

(c) C - DMM+INT+DIFF

Figure 4.7: Contours of the total non-dimensional dissipation rate $\epsilon/({u_0}^3/L)$ and the corresponding volume fraction for the phase-inversion problem at $t = 17\ s$. The oil phase corresponds to the orange region where $\alpha < 0.5$ and the water phase corresponds to the blue region where $\alpha > 0.5$.

near the left and top walls where the oil is present and at the oil-water interface where large velocity gradients are found. In order for the large-eddy simulations to correctly model these regions there must be an appropriate balance between the resolved and subgrid-scale contributions. The best LES results for the kinetic energy dissipation rate are found using the medium grid and the dynamic mixed model combined with the interfacial SGS model (shown in Figure 4.7(b)), while the worst LES results are found using the coarse grid and with the DMM+INT+DIFF combination (shown in Figure 4.7(c)). The reduction of resolved-flow detail such as the long oil filaments is clearly shown on the coarse LES grid and to a lesser extent on the medium grid. The dynamic mixed model combined with the interfacial stress-similarity model on the medium grid reproduces the the large-local dissipation rates near the walls and in some regions of the water-oil interface. The results on the coarse grid significantly under-predict these flow characteristics and hence the domain-integrated dissipation rate is also under predicted.

4.3 Plunging-Breaking Wave

The *a posteriori* study of the LES models is now extended to the three-dimensional problem of a plunging-breaking water wave previously studied with direct-numerical simulations in Section 3.3. The diffusive and the interfacial SGS terms were identified as relatively important contributors to the filtered governing equations, similar to the findings in the phase-inversion problem. The acceleration term was found to be larger for the plunging-breaking wave compared to the phase-inversion problem, but this SGS term is not examined here. The acceleration SGS term is found to be more than an order of magnitude smaller relative to the other SGS terms and hence it is not modeled to bound the scope of the study.

Domain-integrated quantities including the kinetic energy and the kinetic energy

dissipation rate are investigated on a relatively coarse numerical grid compared to the DNS resolution. The LES domain has the same physical dimensions as the DNS grid (see Figure 3.13) and is discretized with 128 cells in the streamwise and vertical direction ($N_x = N_y = 128$) and 64 cells in the spanwise direction ($N_z = 64$), giving a uniformly-spaced numerical grid with 1,048,576 computational cells. The selected grid corresponds to the application of a 5x5x5 filter stencil in the *a priori* study. The spanwise and streamwise boundaries are periodic while the top and bottom are considered as no-slip boundaries. The initial wave profile and water particle velocities are initialized in the same manner as in the *a priori* study using Stokes third-order theory. The same discretization and numerical integration schemes are used as in the case of direct numerical simulations.

The dynamic mixed model is tested individually and also combined with the stress-similarity model with constant coefficients for the diffusive and the interfacial subgrid-scale terms. The dynamic Smagorinsky model is combined with the interfacial SGS model based on the results found in the phase inversion simulations. A pure stress-similarity model combining the diffusive and interfacial terms without any convective SGS modeling is also examined.

4.3.1 Kinetic Energy and Energy Dissipation

The kinetic energy and its dissipation rate integrated over the computational domain are calculated using Equations 4.6 and 4.7. The non-dimensionalized results are summarized in Figure 4.8 for the first two wave periods. During this time period the flow changes rapidly as the initial wave profile breaks in a plunging event and thus the largest magnitudes of the kinetic energy and its dissipation rate are recorded. The ability of the LES model to predict the most energetic stages of the flow evolution is important because in the case of wave impacts on offshore structures, the occurrence of the largest excitation forces is typically correlated with the high-energy events.

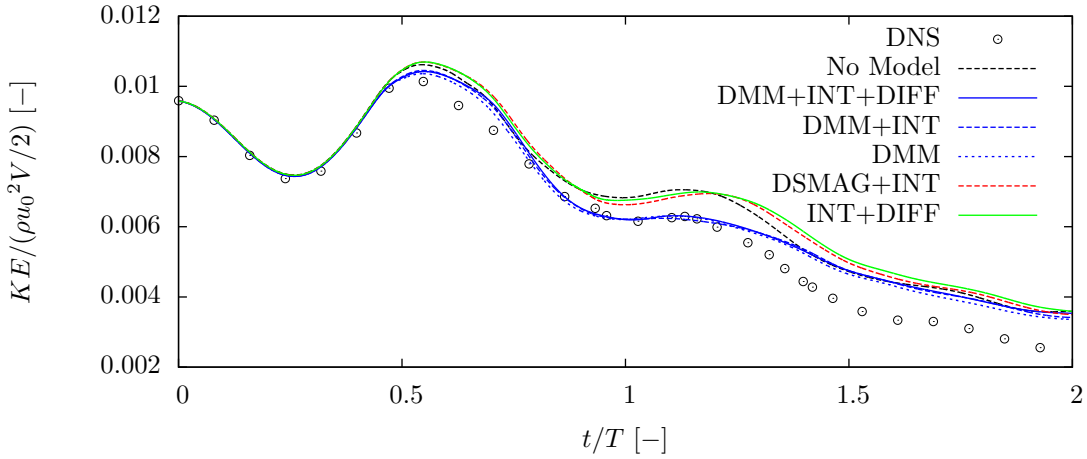

(a) Kinetic energy

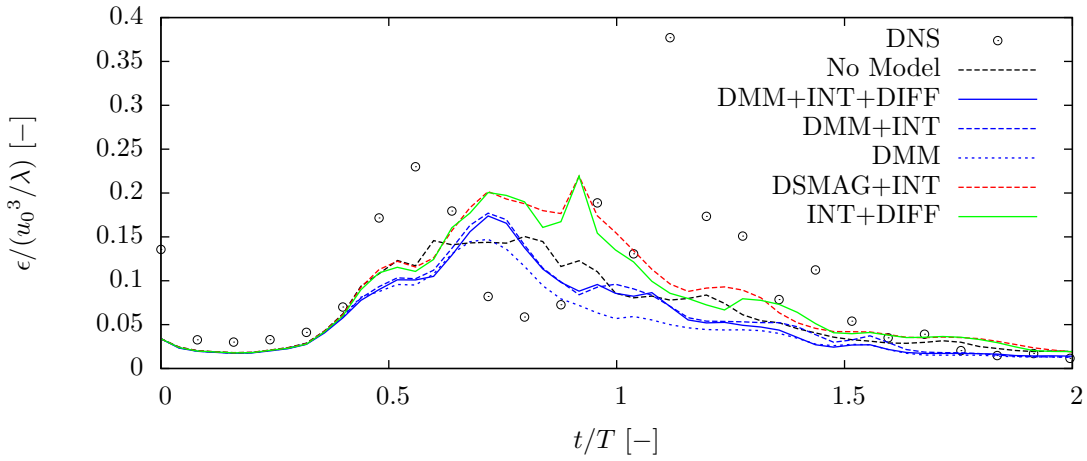

(b) Kinetic energy dissipation rate

Figure 4.8: Domain-integrated flow quantities as a function of time from large-eddy simulations of the plunging-breaking wave

The peak kinetic energy in the domain at $t/T = 0.55$ is slightly over-estimated using all the tested subgrid-scale stress model combinations. The domain-integrated dissipation rate is also found to have a local maximum at this time, but the models used for the large-eddy simulations are unable to capture the magnitude of this peak and under-estimate it by approximately 100%. Between $0.75 < t/T < 1.00$ the LES results over-predict the dissipation rate and at approximately $t/T = 1.15$, the peak of the dissipation rate is not reproduced. As the kinetic energy dissipation rate decreases after $t/T = 1.5$ to pre-breaking levels, all the large-eddy simulations shown

converge to the DNS result. The dynamic Smagorinsky model combined with the interfacial SGS model replicates the dissipation rate near $t/T = 1$. The dynamic mixed model successfully simulates the kinetic energy in the domain between $0.7 < t/T < 1.2$ whereas the dynamic Smagorinsky model offers no benefit over the kinetic energy estimate obtained on the coarse grid with no SGS modeling. The addition of the interfacial and diffusive subgrid models to DMM produces minor changes to the predicted domain-integrated kinetic energy. The dissipation rate is found to generally increase with the additional subgrid models included but the two peaks identified with direct numerical simulations are not fully reproduced.

Simulations with the interfacial SGS model combined with a convective SGS model offer some improvement over the no-model results. The local dissipation-rate maximum near $t/T = 0.75$ reproduced in these simulations is delayed by approximately $0.2t/T$ compared to the DNS results, whereas the no-model result does not yield a sharp dissipation-rate peak at this time. Additionally, the domain-integrated kinetic energy found with the no-model simulation is consistantly over-predicted after $t/T = 0.5$.

4.3.2 Interfacial Subgrid-Scale Contribution

The interfacial stress-similarity model results are examined for the plunging-breaking wave problem in order to understand the contribution of the subgrid model. Isosurfaces of $\partial\tau_{Ii}/\partial x_i$ modeled with the constant-coefficient stress-similarity model ($C_I = 1$) colored by the magnitude are included in Figure 4.9 for several instances in time. Between $0.2 < t/T < 1.2$, the peak contribution of the interfacial SGS model reaches approximately 1.5% of $\partial\overline{u}_i\overline{\alpha}/\partial x_i$ or the maximum resolved term in the interface equation. The *a priori* analysis showed that the divergence of the interfacial subgrid-scale term can reach up to 10% of the resolved maximum term during this stage of the flow development. The under-predicted interfacial model contribution

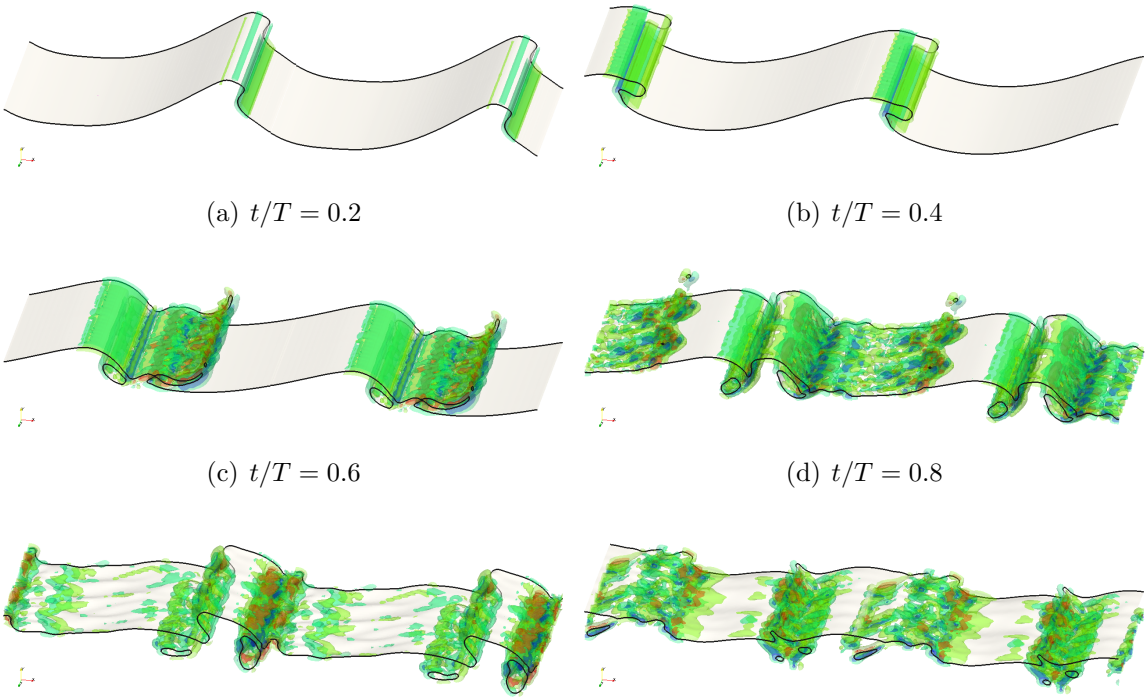

(a) $t/T = 0.2$ (b) $t/T = 0.4$

(c) $t/T = 0.6$ (d) $t/T = 0.8$

(e) $t/T = 1.0$ (f) $t/T = 1.2$

Figure 4.9: Isosurfaces of the interfacial stress-similarity model contribution during the plunging event. Largest positive and negative magnitudes (shown in red and blue, respectively) correspond to approximately 1.5% of the maximum resolved term in the interface equation.

can be linked to the relatively low correlation coefficients of the constant-coefficient stress-similarity model as shown in Figure 3.23(b). The correlation coefficient for the interface term varies between approximately $0.1 < r < 0.3$ throughout the simulation time of six wave periods.

The *a posteriori* study of the plunging-breaking wave is conducted using a coarse LES grid corresponding to the application of the large filter in the *a priori* study. Several combinations of the dynamic mixed model and the dynamic Smagorinsky model with the stress-similarity model for the diffusive and interfacial subgrid terms are examined. The results for the total kinetic energy and the kinetic energy dissipation rate indicate that the tested models are unable to correctly predict the evolution and the temporal maxima of the dissipation rate. The dynamic mixed model is found to perform better than the dynamic Smagorinsky model in predicting the total kinetic energy in the domain, indicating that the inclusion of the similarity-based component in the convective subgrid model is important for turbulent-interfacial flows. The contribution of the constant-coefficient stress-similarity model for the interfacial SGS term is under-predicted and thus not sufficient to significantly affect the solution.

4.4 Cylinder in Waves

The following sections focus on the simulation of breaking waves impinging on a bottom-fixed circular cylinder piercing the free surface. An overview of the problem setup is presented first, followed by a validation study based on experimental data. The effects of the subgrid-scale term modeling in large-eddy simulations of breaking-wave impacts are then investigated.

4.4.1 Problem Description

The force on a cylinder impinged upon by steep and/or breaking three-dimensional waves is studied numerically. The simulation setup is based on a recent experimental campaign summarized in Nielsen et al. (2012) and Bredmose et al. (2013). The campaign focused on an experimental evaluation of wave loads on a vertical-circular cylinder piercing the free surface. The experiments were conduced at the Danish DHI wave basin in an effort to study offshore wind platforms and their survivability in various seastates and especially when steep waves are present.

The monopile platform was fixed to a sloping bottom (slope of 1/25) and secured in place by load cells. A system of wave probes was used to capture the free-surface elevation at several locations close to the wave maker and the cylinder (see Figure 4.10(b)). The model-scale cylinder diameter D was 0.075 m or 6.0 m in full scale. In the results presented here the calm-water depth at the location of the cylinder is 0.78 m in model scale. Both small-amplitude linear regular waves and high-steepness regular waves are investigated. The length of the incoming waves is held constant at 3.34 m in model scale and the wave period T is 1.54 s, corresponding to a wave number k of 1.82 and intermediate water depth. The small-amplitude linear waves have a steepness ratio $H/\lambda = 0.030$ while the steep-regular waves are initialized with $H_0/\lambda_0 = 0.084$ where H_0 and λ_0 are the initial wave height and wave length, respectively, generated at the inlet boundary or the wave maker. An initial steepness ratio is specified because as the train of steep waves interacts with the sloping seabed the effective steepness ratio tends to increase and the waves eventually break in the proximity of the cylinder.

The computational domain is modeled after the experimental setup and is depicted in Figure 4.10. The domain width W is approximately $23D$ wide to minimize the interaction of reflected waves with the side walls, the inlet length L_{in} is equal to λ and the outgoing waves are damped out near the outlet boundary over $L_{out} = 3\lambda$. The

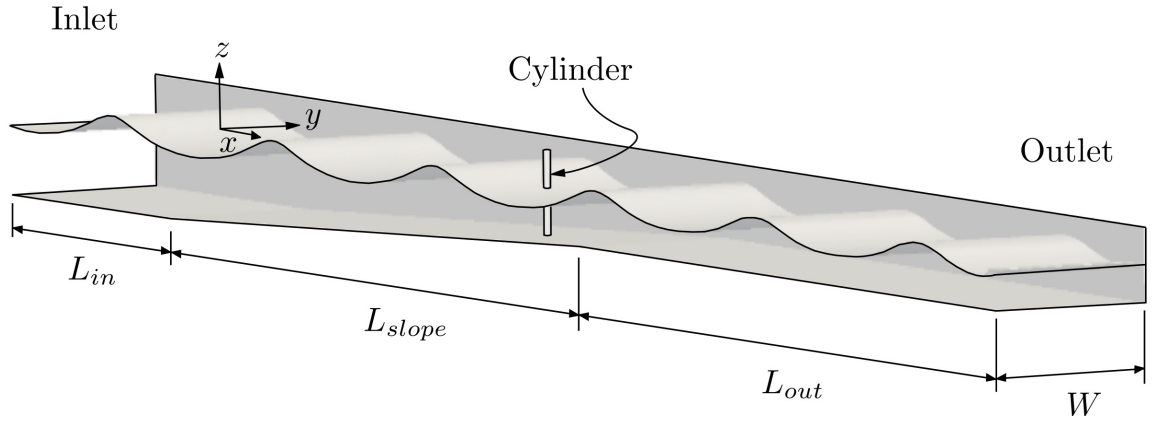

(a) Main dimensions of the computational domain

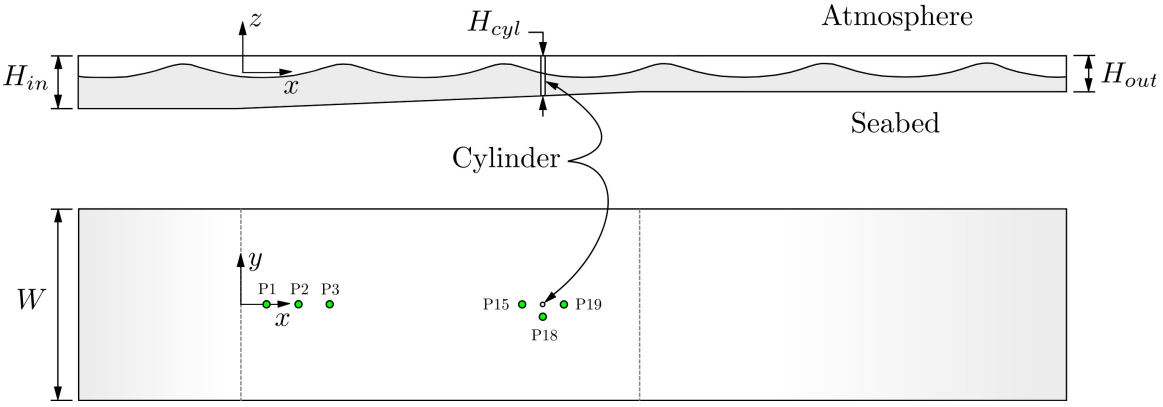

(b) Side centerline profile illustrating the 1/25 seabed slope formed between the inlet and outlet boundaries and top view depicting an approximate location of the wave probes

Figure 4.10: Details of the computational domain

incoming waves are generated using the OpenFOAM extension toolkit waves2Foam (Jacobsen et al. (2011)) which utilizes relaxation zones near the domain inlet and outlet for both wave generation and damping in order to avoid unwanted wave reflections. This toolkit also provides the user with a large selection of wave theories including linear waves, several orders of Stokes theory, cnoidal theory, and more. The flow field can be initialized using any wave theory to obtain the free-surface elevation and water particle velocities everywhere in the computational domain.

The fully-structured computational grids are constructed using the software Pointwise. The coarse grid consists of approximately 3.6 million cells and the fine grid contains approximately 22 million cells. At least 400 grid points per wave length and 40 grid points per wave height are used to accurately represent the free surface with negligible numerical dissipation as shown by Piro (2013). The cylinder, seabed, and the lateral boundaries are modeled as slip boundaries and hence they do not allow for the development of viscous boundary layers. In the cases studied here, inertial forces dominate the forces acting on the cylinder, but the full implications of not resolving the viscous boundary layer formed near the body are of interest for future work. The influence of the viscous boundary layers is anticipated to become significant when shorter wave lengths and hence larger D/λ ratios are of interest.

The governing equations are discretized and integrated in time as in the previously discussed simulations with the exception of the convective term in the momentum equation and the advection term in the interface equation. These terms are discretized with flux-limited schemes to preserve the monotonicity of the solution while retaining an overall second-order accuracy. Limited schemes has been shown by Jasak (1999) to be more robust for non-uniform grids, which are common in industrial simulations because of the complexity of the geometry involved. The additional numerical dissipation that is introduced by such schemes can adversely affect LES, but its influence is highly dependent on the grid quality (Sagaut (2001)). The quality

of the grids used in this study is relatively high based on several grid quality criteria including cell expansion ratio, skewness, and non-orthogonality. Because of the high quality grids used, the impact of the numerical dissipation associated with the limited schemes is expected to be small.

4.4.2 Linear Regular Waves

The numerical method used to simulate water waves is first validated using small-amplitude linear waves with $H/\lambda = 0.030$. Airy waves are generated on the coarse grid at the domain's inlet and propagated in the direction of the cylinder. No turbulence modeling is used in this case because of the small wave steepness used and the lack of complex free-surface structures. The free-surface elevation and in-line force on the cylinder are recorded for 20 periods and compared to the experimental data. The free-surface elevation non-dimensionalized by the wave amplitude A as a function of time from four different wave probes is shown in Figure 4.11. Probe P1 is located on the centerline and near the wave maker. Probe P15 is located approximately $3D$ in front of the cylinder, probe P18 is located at the streamwise location of the cylinder but offset laterally by $6D$, and probe P19 is located approximately $3D$ downstream of the cylinder on the centerline.

The amplitude and period of the incoming waves and the free-surface elevation downstream from the cylinder are closely reproduced in the simulation. Minor differences in the phases are expected because of the difficulty in a perfect reproduction of experimental data that can often contain some measurement error. The wave peaks and troughs are consistently reproduced throughout the simulation indicating that the choice of a limited linear scheme for the discretization of the convective term does not result in an excessive dissipation of energy. The in-line force acting on the cylinder is non-dimensionalized with $\rho g A D^2$ and presented in Figure 4.12. The difference between the numerical and experimental results is greater here than in the

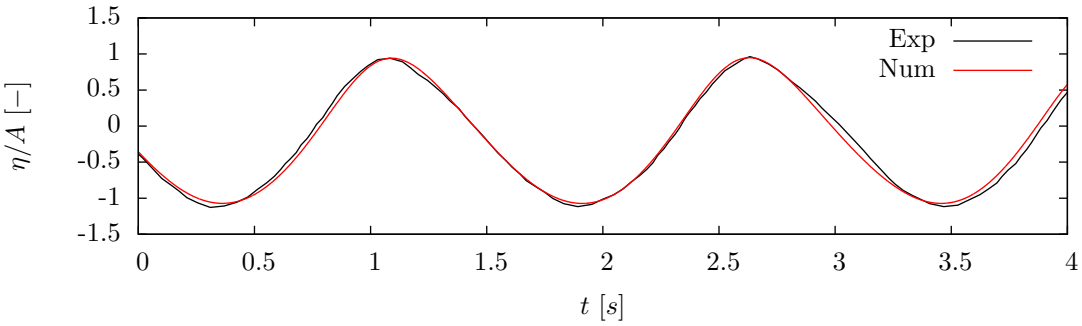

(a) Probe 1: $x = 1.00\ m$, $y = 0.00\ m$

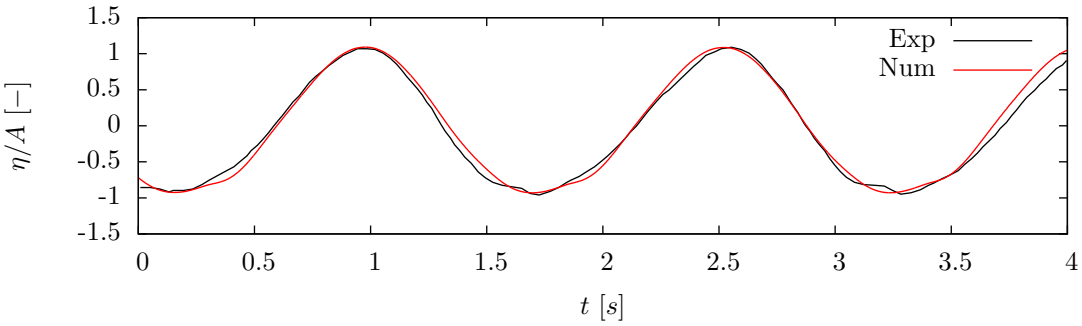

(b) Probe 15: $x = 7.50\ m$, $y = 0.00\ m$

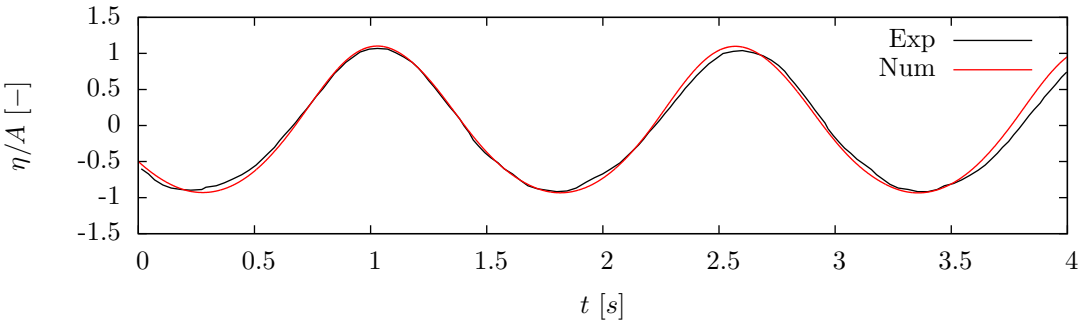

(c) Probe 18: $x = 7.75\ m$, $y = -0.50\ m$

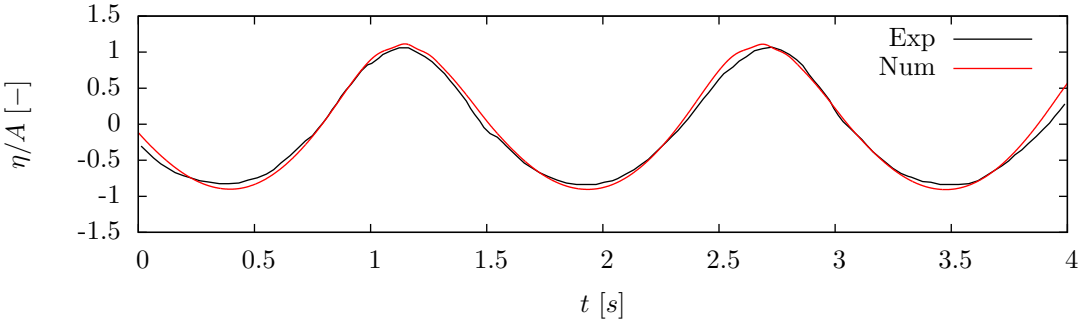

(d) Probe 19: $x = 7.95\ m$, $y = 0.00\ m$

Figure 4.11: Free-surface elevation of regular-linear waves at four probe locations

case of the free-surface elevations but the amplitude and period of the force signal obtained using the present numerical simulation is on par with the currently available state-of-the-art numerical tools. It is worthwhile to point out that in this case of small-amplitude linear waves and large λ/D ratios the magnitude of the in-line force on a circular cylinder is effectively predicated using the Morison's equation at a much-reduced computational cost. However, the goal of this study is to validate the numerical toolkit used to simulate water waves with the finite volume approach and in a time-accurate manner before applying this toolkit to problems with steep and breaking waves where the Morison's equation is less accurate due to the assumptions used in its formulation.

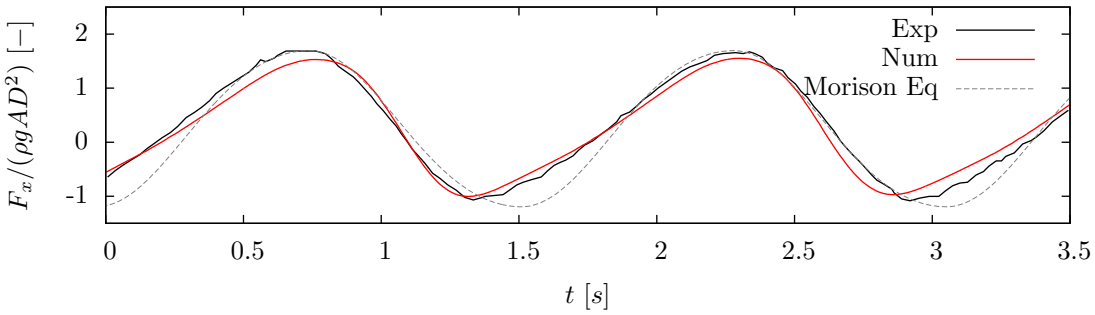

Figure 4.12: Cylinder in-line force due to regular-linear waves

4.4.3 Steep Regular Waves

The steepness ratio of the incoming waves is now increased to $H_0/\lambda_0 = 0.084$ to study the interaction of nonlinear waves with the bottom-fixed cylinder. Stoke's fifth-order nonlinear wave theory is used to simulate physical waves in an intermediate water depth. The ratio of the the wave height to the mean water depth h is $H_0/h = 0.37$ and the ratio of the mean water depth to the wave length is $h/\lambda_0 = 0.233$. The Ursell parameter is $U = H_0{\lambda_0}^2/h^3 = 6.76$ or less than the $U < 40$ limit of Stokes fifth-order theory (Dean and Dalrymple (1991)).

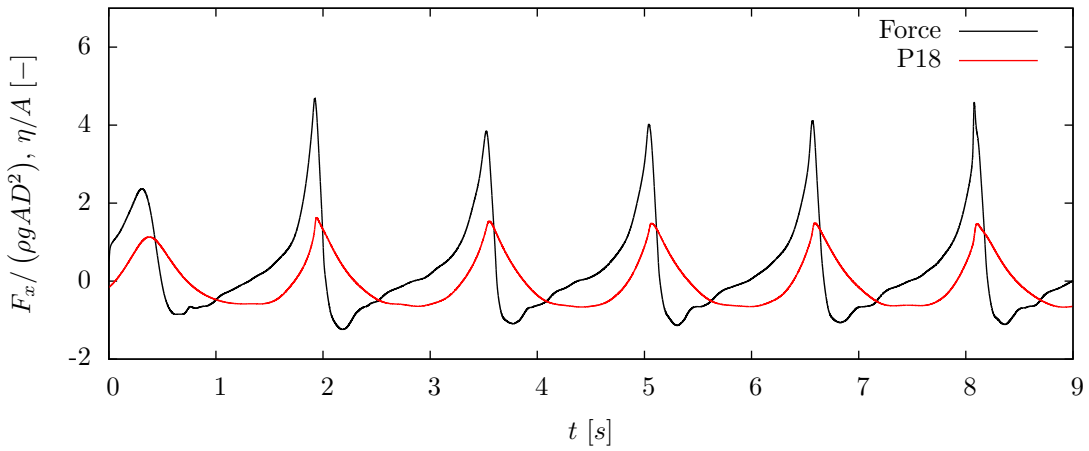

Figure 4.13: In-line force and free-surface elevation at probe 18 ($x = 7.75\ m$, $y = -0.50\ m$) for steep regular wave impacts ($H_0/\lambda_0 = 0.084$)

The decreasing water depth due to the sloping seabed results in the incoming waves becoming steeper and eventually breaking in either a plunging or spilling event. A sample force and free-surface elevation time history of the steep-regular waves impinging on the cylinder calculated on the fine grid with no turbulence modeling is shown in Figure 4.13. The free-surface elevation is recorded at probe P18 which is located next to the cylinder. The entire flow field at $t = 0\ s$ is initialized with the fifth-order Stokes waves and the first wave peak is located approximately $6D$ in front of the cylinder. Because this wave travels over a small portion of the sloping seabed before impacting the cylinder, no breaking event occurs and the resulting in-line force acting on the cylinder is considerably smaller compared to the following wave impacts. In Figure 4.14, four instances in time between $0.2\ s < t < 0.8\ s$ illustrate the flow-field through the free-surface elevation contour colored by the non-dimensional amplitude (top portion of the image) and the dynamic pressure $p_d = p - \rho g h$ on a centerline plane (bottom portion of the image). The pile-up of water on the front face of the cylinder is visible in Figure 4.14(b) followed by formation of a wake as the wave propagates past the cylinder. The dynamic pressure field reaches its maximum near the wake peak and remains mostly unaffected by the presence of the cylinder

and the small deformation of the wave profile.

The next wave propagates over the majority of the sloping seabed before arriving to the location of the cylinder. The free-surface elevation recorded at probe P18 next to the cylinder is found to increase significantly compared to the first wave event. Figure 4.15 shows the development of this wave profile between $1.6\ s < t < 2.2\ s$. The formation of the overturning jet characteristic of plunging-breaking waves is observed in Figure 4.15(b) right before impact which generates spray and results in the collapse of the plunging breaker in the wake of the cylinder. The in-line force on the cylinder is approximately 100% greater than the in-line force resulting from the non-breaking steep wave. The increase in the force on the cylinder due to breaking events has been previously shown both experimentally (Apelt and Piorewicz (1987); Chakrabarti et al. (1997); Wienke et al. (2001)) and numerically (Bredmose et al. (2013); Ramirez et al. (2012); Zang et al. (2010)). The overturning and subsequent collapse of the wave generates large turbulent structures which are highly three-dimensional in nature unlike the pre-breaking wave which is mostly two-dimensional. The latter instances in time depicted in Figures 4.15(c) and 4.15(d) show the formation of these structures that are on the order of the cylinder diameter in length near the free surface. Detailed resolution of spray generation and smaller turbulent structures is not possible with this grid resolution but the turbulence that is resolved is responsible for a large portion of the turbulent energy budget.

The third wave arrives at the location of the cylinder at approximately $t = 3.5\ s$. The wave breaks before reaching the cylinder and thus it resembles a spilling breaker at the time of arrival to the location of the cylinder. Unlike the second wave which forms a toe at the wave crest that eventually plunges in the proximity of the cylinder, this wave and the subsequent waves are generated over a flat bottom before they propagate over the entirety of the sloping seabed. The interaction of the initial wave with a steepness of $H_0/\lambda_0 = 0.084$ and the sloping bottom results in wave breaking

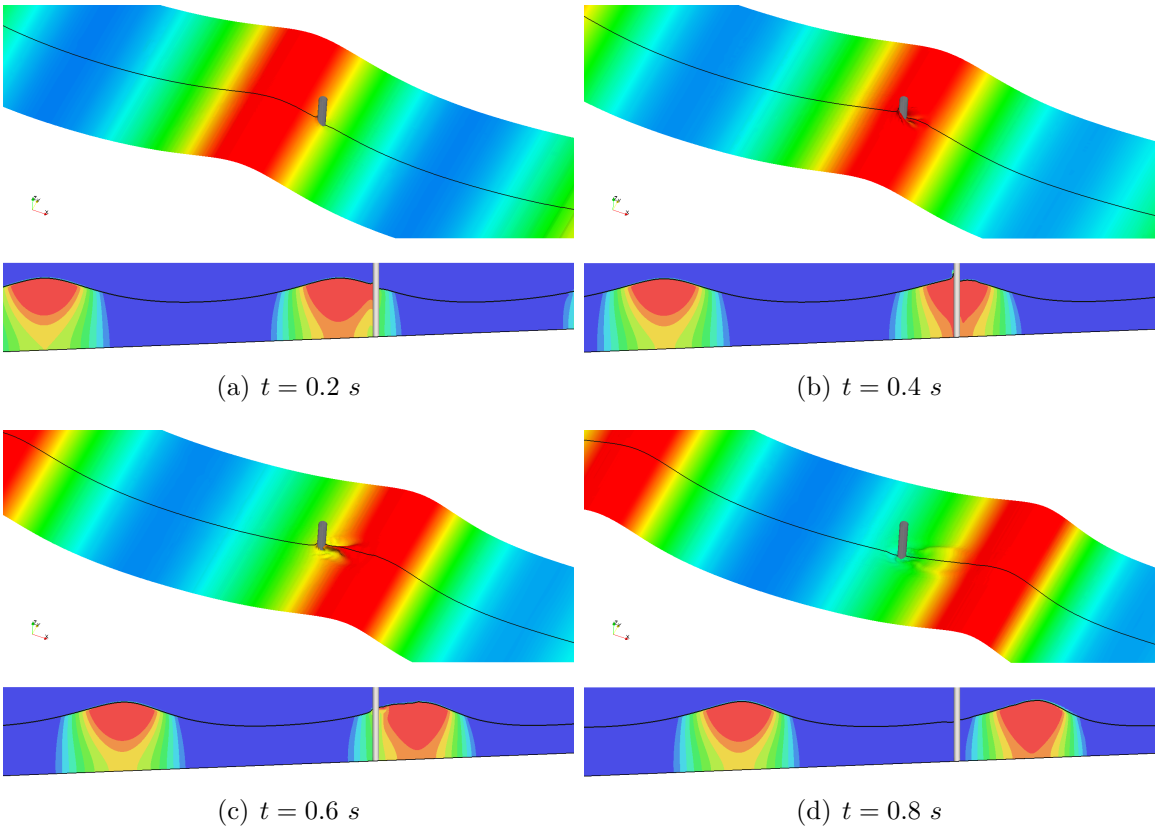

(a) $t = 0.2\ s$ (b) $t = 0.4\ s$

(c) $t = 0.6\ s$ (d) $t = 0.8\ s$

Figure 4.14: Steep regular wave ($H_0/\lambda_0 = 0.084$) impinging on the cylinder. Free-surface contour colored by non-dimensional amplitude (η/A) and contours of the dynamic pressure p_d on a centerline slice.

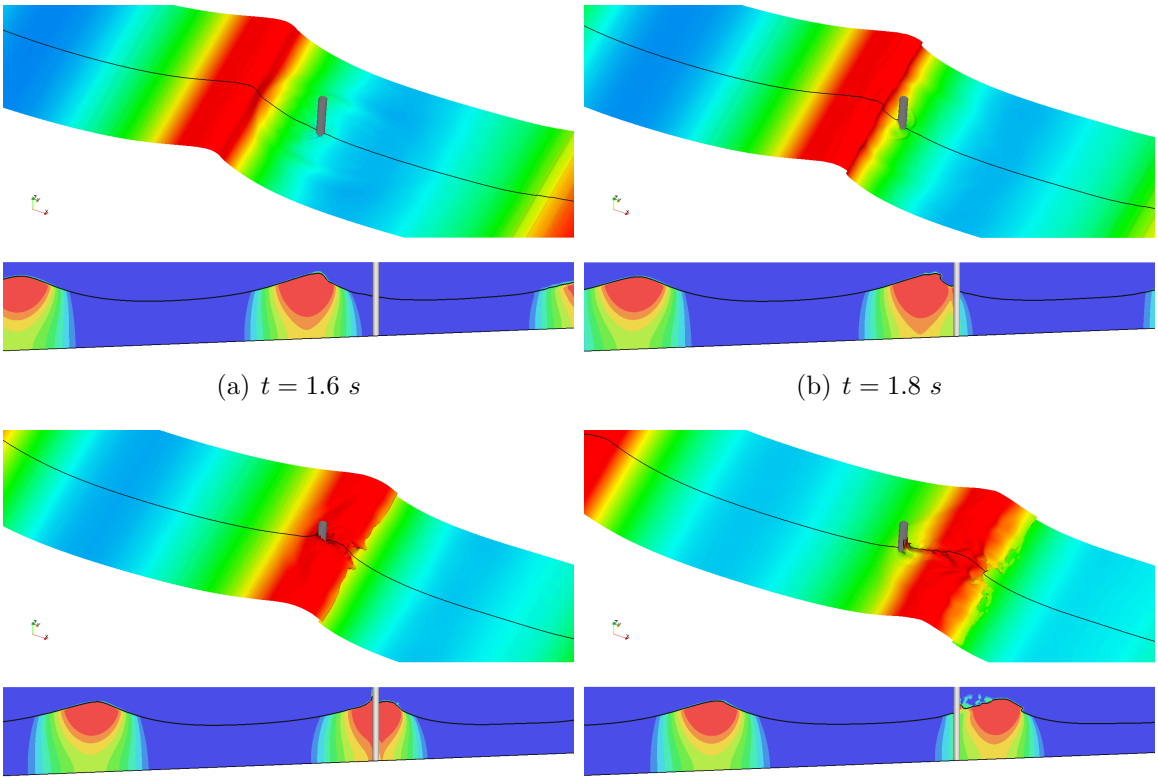

(a) $t = 1.6\ s$ (b) $t = 1.8\ s$

(c) $t = 2.0\ s$ (d) $t = 2.2\ s$

Figure 4.15: Breaking wave ($H_0/\lambda_0 = 0.084$) plunging in front of the cylinder. Free-surface contour colored by non-dimensional amplitude (η/A) and contours of the dynamic pressure p_d on a centerline slice.

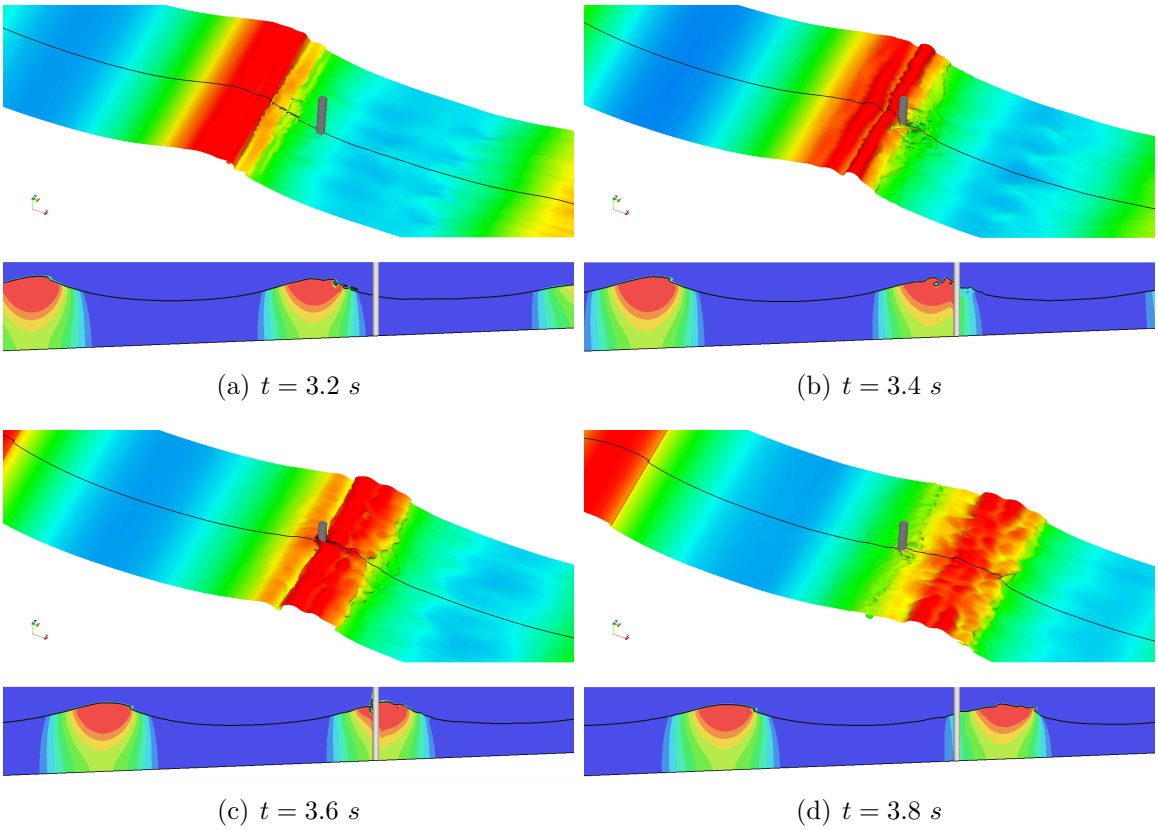

(a) $t = 3.2\ s$ (b) $t = 3.4\ s$

(c) $t = 3.6\ s$ (d) $t = 3.8\ s$

Figure 4.16: Breaking wave ($H_0/\lambda_0 = 0.084$) spilling in front of the cylinder. Free-surface contour colored by non-dimensional amplitude (η/A) and contours of the dynamic pressure p_d on a centerline slice.

occurring in front of the cylinder and a spiller-like wave impact. The free surface is highly distorted through the spilling process and through the interaction with the cylinder as shown in Figure 4.16. The free surface contains roller-like structures that span the domain width until they propagate past the cylinder. The free surface then becomes highly three-dimensional and a wide range of turbulent interfacial structures is observed. The roller-like structures result in an in-line force profile that is less steep and smaller in magnitude than in the case of the plunging breaker. The impact force is approximately 50% greater than the force of a regular non-breaking steep wave because of the increased wave height and the highly-energetic breaking process occurring near the time of impact. The dynamic pressure contours also indicate that the largest pressures are more localized and found closer to the free surface when compared to the plunging breaker and the non-breaking steep wave. The presence of the interfacial-turbulent structures during the spilling events is beneficial to the application of the scale-similarity concept presented in Chapter 2 because the resolved portion of the highly-unsteady free surface may sufficiently model the effects of the subgrid interface behavior.

4.4.4 Steep Regular Waves and Modeling of Interfacial Turbulence

The results of the *a priori* analysis presented in Section 3.3 and the *a posteriori* analysis in Sections 4.2 and 4.3 are used to perform large-eddy simulations of steep waves impinging on a circular cylinder. The computational setup discussed in Section 4.4.3 is used and the models for the convective and interfacial subgrid-scale terms are introduced on the coarse grid. The results of these large-eddy simulations are then compared to the force and surface-elevation data obtained on the fine grid. The results from the fine grid are used for comparison because the experimental data collected at the DHI wave basin are unavailable for public access at the time of writing.

Nonetheless, the present numerical results provide a highly-resolved dataset that is sufficient for a preliminary evaluation of the LES models.

The *a priori* analysis of the phase inversion and breaking-wave problems identified the convective term as the largest subgrid-scale terms in the studied interfacial flows. This result is anticipated because the convective effects are responsible for a significant portion of the energy transfer that is truncated through the application of the low-pass filter. Additionally, previous applications of the single-phase LES concepts to select multiphase problems have shown relative success in predicting global quantities of the flow when only modeling the convective SGS stress tensor. The interfacial SGS term was often found to be the second largest SGS term in the breaking-wave problem, especially at the most energetic stage of breaking. The maximum magnitude of the interfacial term relative to the resolved contribution can be of the same order of magnitude as the convective term in the two interfacial flows studied. Additionally, the interfacial term is found to increase in magnitude when coarser grids or larger filtering stencils are used and thus the interfacial SGS term is anticipated to be important in industrial applications where coarse numerical grids are common. With industrial applications in mind, the coarse grid described in Section 4.4.1 is used to perform large-eddy simulations utilizing models for the convective and the interfacial terms. The convective SGS stress is modeled using the robust dynamic mixed model. The generalized scale-similarity or the stress-similarity concept described in Section 2.3 is applied to model the interfacial SGS term.

The non-dimensional in-line force obtained on the coarse grid with and without subgrid-scale modeling is compared to the highly-resolved data from the fine grid simulation. The time series for the first six impacts is shown in Figure 4.17(a) and a close-up of $4.5\ s < t < 9.0\ s$ is shown in Figure 4.17(b). The simulation with the dynamic mixed model and the stress-similarity model for the interface term (DMM+INT) is shown to give the same force profile as the other simulations between

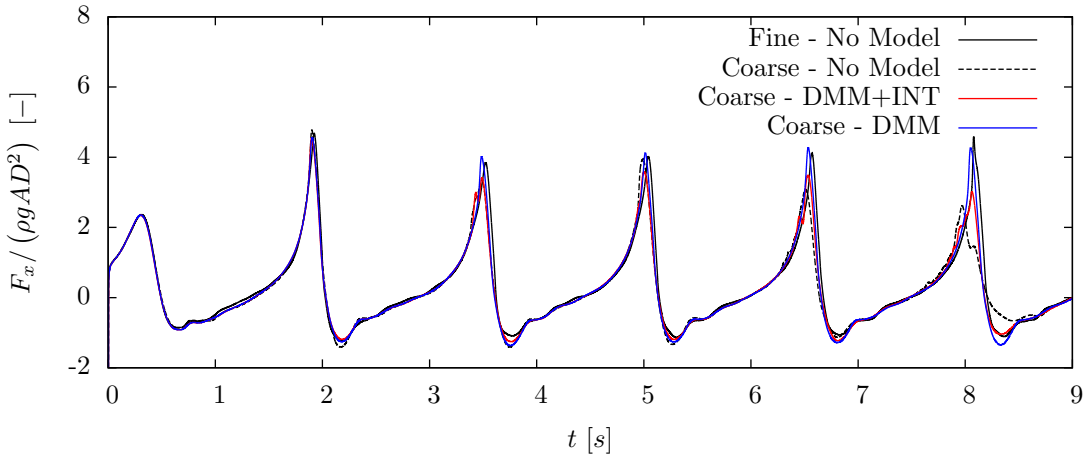

(a) First six impacts

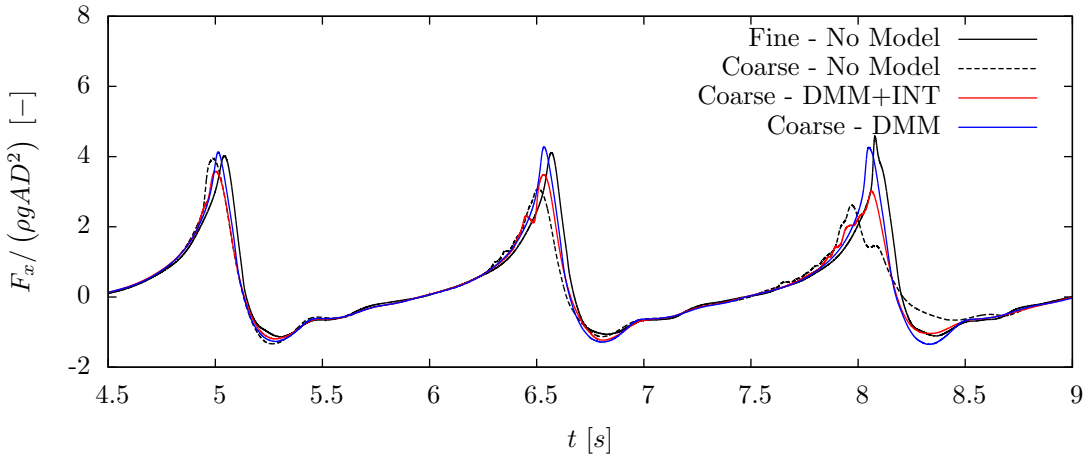

(b) Close up of the latter three wave impacts

Figure 4.17: In-line force on the coarse and fine grid for steep regular wave impacts ($H_0/\lambda_0 = 0.084$)

$0\ s < t < 1\ s$ where a steep non-breaking wave impacts the cylinder. This is expected because the free surface does not undergo significant deformations as this time and the contribution from the turbulence models is limited by the dynamic procedure. Between $1.5\ s < t < 4.5\ s$ the cylinder is impinged upon by a plunging-breaking wave and then a spilling-breaking wave, as described in Section 4.4.3. The force on the cylinder and the timing of the arrival of the peak force due to the plunging-breaking wave is captured well on the coarse grid. Similarly, the first spilling wave event and the associated force is predicted well regardless of the use of the SGS modeling.

The maximum negative force on the cylinder associated with the formation of a wake behind the cylinder is over-predicted when the SGS modeling is not used. The free surface immediately behind the cylinder undergoes a significant deformation due to negative pressure on the suction side of the cylinder prior to impact. At the location of probe P19 ($x = 7.95\ m$, $y = 0.00\ m$ or $3D$ downstream from the cylinder) the free-surface elevation on the centerline shown in Figure 4.19(a) does not differ between the two coarse grid simulations. The over-prediction of the maximum negative force is therefore linked to the flow field in the immediate proximity of the cylinder. Two isosurfaces of the interfacial SGS term are shown at $t = 2.0\ s$ and $t = 2.2\ s$ in Figure 4.18. In the wake region, the stress-similarity model for the interfacial SGS term is shown to be highly active when the peak of the wave moves past the cylinder.

During the next three impacts between $4.5\ s < t < 9.0\ s$ the waves break in either a weak plunging or spilling manner and the differences between the simulations on the coarse grid become more pronounced. The flow field now retains a portion of resolved turbulence near the cylinder once several waves propagate by and a calm condition is no longer achievable before the arrival of the next wave. During all three impacts the maximum negative force on the cylinder obtained using the combination of the dynamic mixed model and the interface SGS model shows an excellent match with

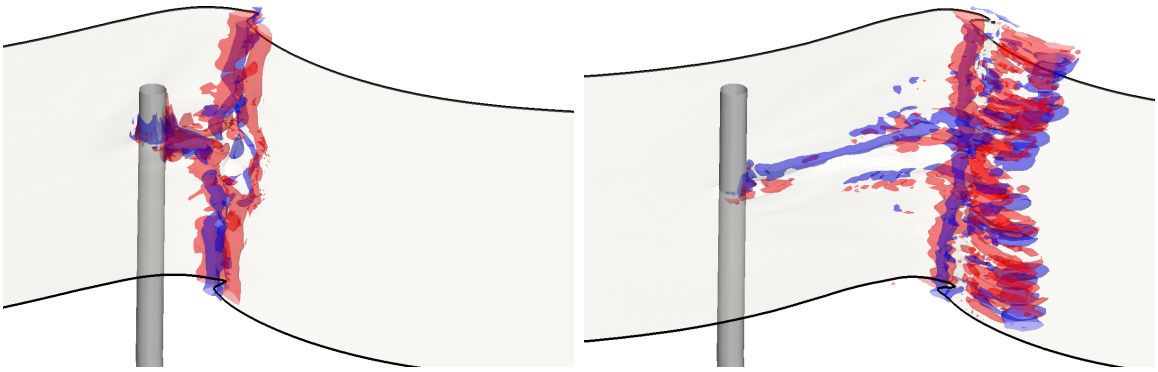

(a) $t = 2.0\ s$ (b) $t = 2.2\ s$

Figure 4.18: Isosurfaces of the interfacial SGS term contribution in the wake region

the results from the fine grid. The benefit of employing the selected SGS modeling is clearly shown near $t = 8.3\ s$ where the simulation without SGS modeling severely under-predicts the maximum negative force on the cylinder. Additionally, the subgrid models allow for a more accurate prediction of the arival time of the peak force. During the last shown impact the coarse grid simulation without SGS models predicts the arrival of the maximum force approximately 0.2 s (13% of the wave period) too early, whereas the case with SGS models closely matches the arrival time compared to the fine grid simulation. The magnitude of the peak force is under-predicted during all three wave impacts in both the no-model and the DMM+INT simulations. Similarly, the free-surface elevation recorded at the three near-cylinder probes (shown in Figure 4.19(b)) is also under-predicted, but the error is reduced when using the SGS models, particularly during the last two impacts. Additionally, the combined use of the dynamic mixed model and the interfacial model improves the profile of the arriving waves and reduces the spreading of the wave peaks. Simulation using just the dynamic mixed model yields the closest results for the force and surface-evelation profiles compared to the reference simulation on the fine grid.

To understand how the SGS modeling is using the resolved turbulent structures to mimic the subgrid behavior and hence improve the force and free-surface elevation

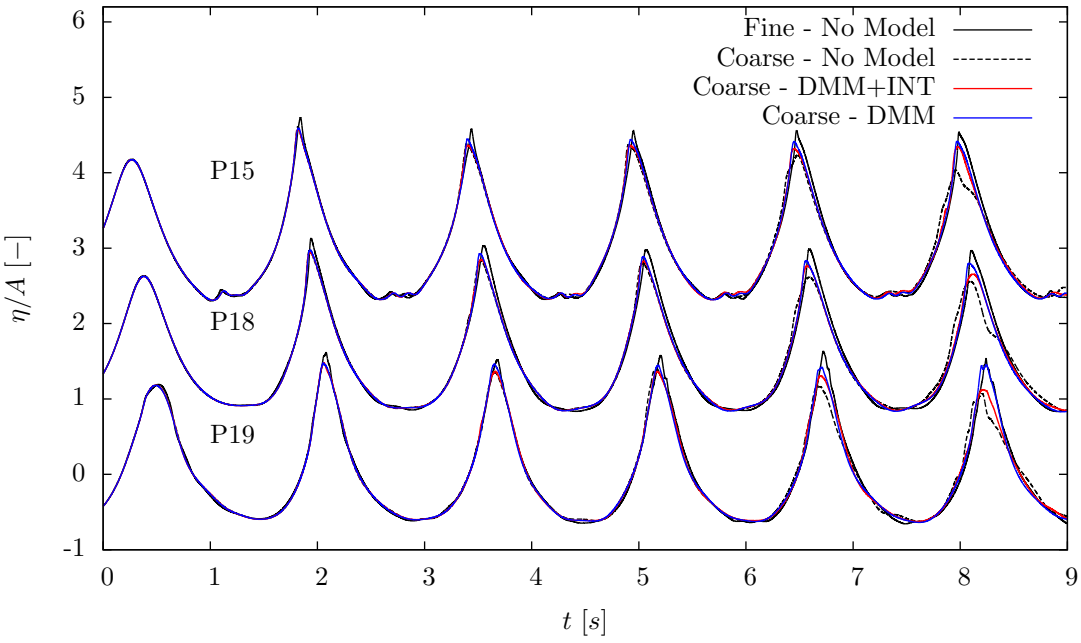

(a) First six impacts

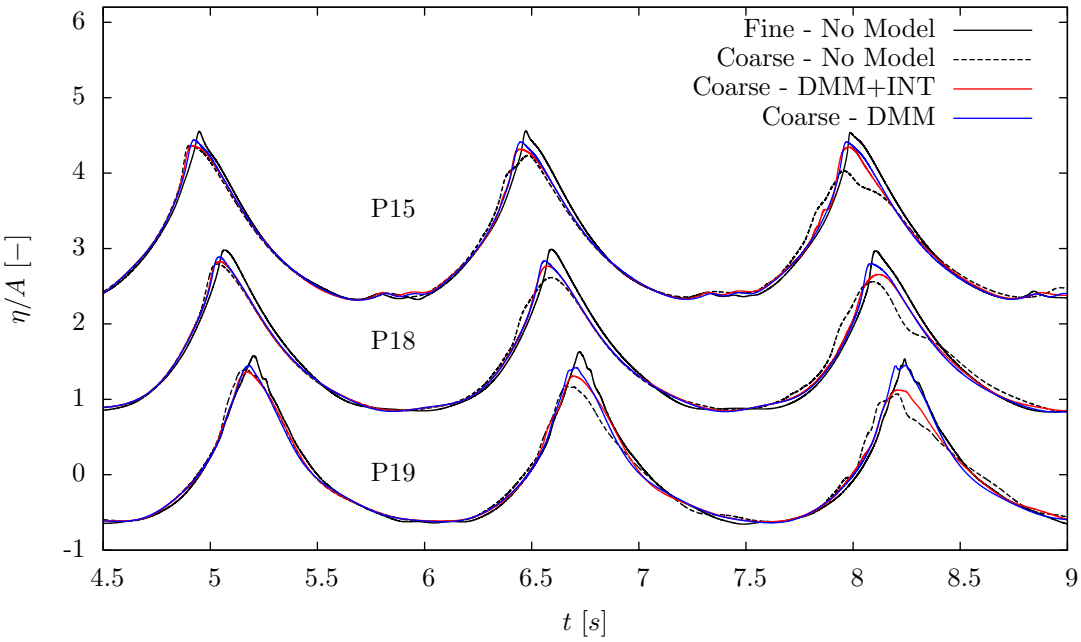

(b) Close up of the latter three wave impacts

Figure 4.19: Free-surface elevation at three near-cylinder probes on the coarse and fine grid for steep regular wave impacts ($H_0/\lambda_0 = 0.084$). Vertical offset of $\eta/A = 1.5$.

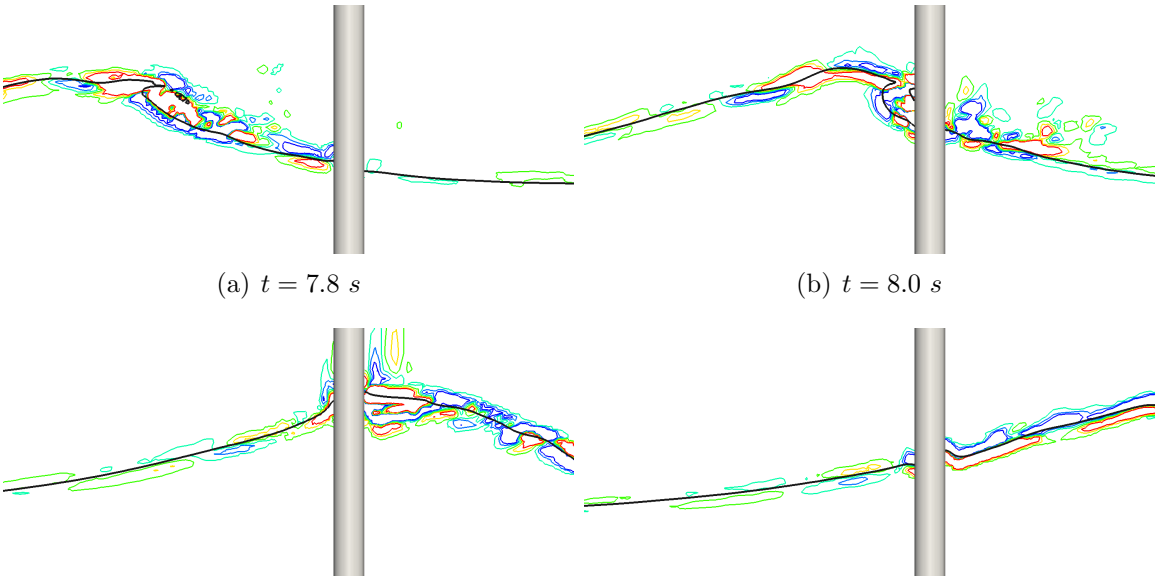

(a) $t = 7.8\ s$ (b) $t = 8.0\ s$

(c) $t = 8.2\ s$ (d) $t = 8.4\ s$

Figure 4.20: Centerline free-surface contour (black) and contours of the divergence of the interface SGS term modeled using the stress-similarity model

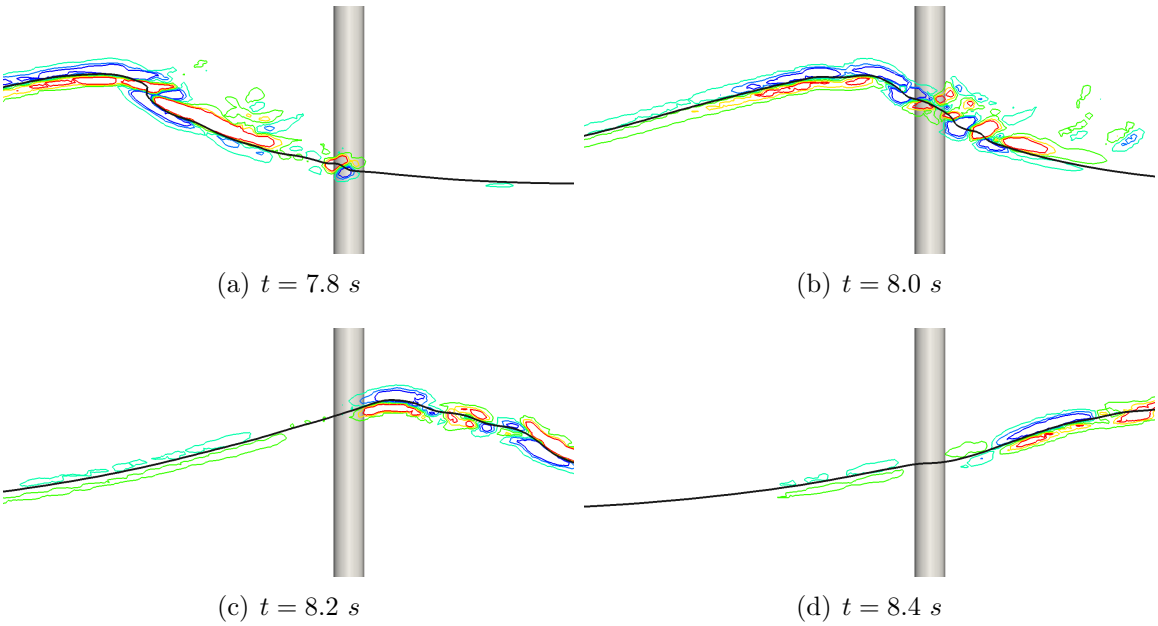

(a) $t = 7.8\ s$ (b) $t = 8.0\ s$

(c) $t = 8.2\ s$ (d) $t = 8.4\ s$

Figure 4.21: Free-surface contour (black) and contours of the divergence of the interface SGS term modeled using the stress-similarity model on a plane at $y = 1D$

predictions, the contribution of the interfacial SGS model is investigated. Contours of the interfacial SGS term $\partial\tau_{Ii}/\partial x_i$ are shown in Figure 4.20 on the centerline and in Figure 4.21 on a plane offset laterally by one diameter between 7.8 $s < t <$ 8.4 s when the largest difference between the coarse grid simulations is found. The contribution of the interfacial model is limited to the region near the free surface where τ_I is nonzero. The contours shown correspond to regions where the stress-similarity model contributes between 5% to 15% of the maximum resolved term in the interface equation (Equation 2.43) using $C_I = 1.0$.

Large-eddy simulations with the interfacial and the convective SGS models offer some benefits compared to a simulation without any SGS modeling. In the problem investigated here, modeling of just the convective SGS stress gives better overall results of the force and free-surface elevation predictions compared to the combined convective and interfacial modeling. The peaks of the force and free-surface elevation are shown to be reduced by up to 32% when the interfacial SGS term model is introduced with $C_I = 1.0$. Such overly-dissipative behavior is likely due to a too large of a contribution from the stress-similarity model with a constant coefficient. The influence of the interfacial SGS model is further investigated in Figure 4.22 by changing the stress-similarity model contribution through a reduction of the model coefficient by 50% ($C_I = 0.5$) and 90% ($C_I = 0.1$). Smaller contribution from the interfacial model results in better peak-force prediction and an improvement in the prediction of the maximum negative force acting on the cylinder. The stress-similarity coefficient can be computed dynamically through the application of the generalized Germano identity (Equation 2.21) at a secondary test-filter level used to extract flow information beyond the first test-filter level. The additional test-filtering process could dynamically adjust the amount of contribution from the interfacial SGS model based on the resolved interfacial structures and their interaction with the resolved velocity field. Dynamic coefficient adjustment has been shown to improve convective SGS modeling

for the interfacial flows (Chesnel et al. (2011a)) and hence it should also improve the combined interfacial and convective SGS modeling performance for breaking-wave flows. The implementation and testing of this procedure is recommended for future work.

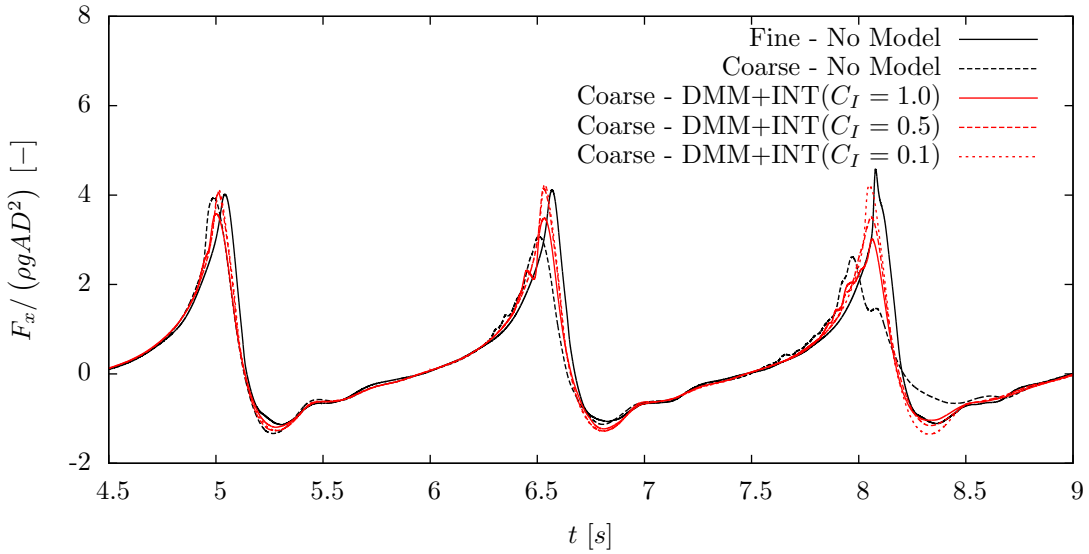

Figure 4.22: In-line force as a function of C_I for steep regular wave impacts ($H_0/\lambda_0 = 0.084$)

4.5 Summary

In this chapter, the *a posteriori* analysis of the phase-inversion and the plunging-breaking wave problems is presented. The large-eddy simulations of the two canonical flows are executed with subgrid-scale models for the largest SGS terms identified through the *a priori* analysis. Additionally, multiphase large-eddy simulations of breaking waves impinging on an offshore structure are discussed. The dynamic mixed model is found to be the most consistent and robust model for the convective SGS term. The interfacial subgrid-scale model based on the stress-similarity concept is shown to have a potential benefit to large-eddy simulations of turbulent-interfacial flows. An appropriate resolution of the interface is necessary because the model relies

on a test-filtering procedure and an extraction of resolved interface information to model the subgrid behavior. Based on the analysis of the interfacial subgrid contributions, a dynamic procedure for the calculation of the stress-similarity coefficients or a dynamic adjustment of the test-to-grid level filter is also necessary to improve the performance of the stress-similarity model.

CHAPTER 5

Summary and Conclusions

5.1 Summary

The interaction of turbulence with a deformable interface separating two phases has been studied with highly-resolved numerical simulations of multiphase flows relevant to the marine industry. Two canonical flows including the phase inversion problem and the plunging-breaking wave problem are studied with the direct numerical simulations approach to resolve the most active turbulent scales in both phases and to accurately represent the evolution of the interface. The DNS data allows for an in-depth study of the smallest scales that are not resolved using lower-fidelity numerical tools such as large-eddy simulations. The inversion of an oil inclusion inside of a closed domain filled with water is studied first to examine the turbulent-interfacial scales using a simple two-dimensional domain and to compare the present findings against previously published results. The breaking process of a three-dimensional water wave is also simulated to determine the influence of the large density and viscosity ratios on the turbulence-interface interaction. The *a priori* analysis is applied to both canonical flows in order to determine the hierarchy of the subgrid-scale terms present in the governing equations of multiphase large-eddy simulations. Additionally, several approaches commonly used to model the subgrid behavior are benchmarked for performance in multiphase applications. A structural model for the subgrid terms

associated with the presence of the interface is found to correlate well with the true subgrid behavior. The model is implemented in the LES solver to study the two canonical flows with the *a posteriori* approach. Finally, a complex flow involving breaking and spilling-wave impacts on an offshore structure is examined with the large-eddy simulations solver.

The phase-inversion problem is studied because it contains many of the relevant features of turbulent-interfacial flows also found in the marine environment. The unstable initial conditions of the oil result in a complex deformation of the interface and turbulence generation due to the interaction of the two phases and also due to the presence of no-slip boundaries. The relative importance of the the smallest interfacial and turbulent scales that are typically not resolved in large-eddy simulations is examined by comparing the subgrid quantities to the resolved counterparts. The traditional convective subgrid stress also present in single-phase LES equations is found to be the largest subgrid contribution in the phase-inversion problem, but the influence of the diffusive and the interfacial subgrid terms increases rapidly when the filter size is increased. The structural modeling approach in the form of the stress-similarity model is found to be highly correlated with the true subgrid terms during the most energetic stages of the flow development.

The simulation of the plunging-breaking wave focuses on three-dimensional turbulent-interfacial flow features that form upon impact of the overturning jet onto the front face of the wave. Air cavities are entrained and filament-like structures are ejected during impact, eventually leading to the formation of small air bubbles and water droplets in the proximity of the free surface. The presence of the small-interfacial features in highly-energetic regions of the flow field and the large density ratio result in the subgrid interfacial contribution to be comparable in magnitude to the resolved term. The convective subgrid term is also found to be important and a significant contributor to the LES governing equations. The modeled subgrid behavior obtained

using the stress-similarity model is found to be less correlated with the true subgrid terms than in the phase-inversion problem. The degraded performance of the model is associated with non-homogeneity of the subgrid structures, the ratio of the test and grid-level filters, and the constant-coefficient implementation of the model, resulting in a poor localization of some regions responsible for the largest subgrid contributions.

Large-eddy simulations of the two canonical flows have been executed to study the influence of the modeled subgrid terms in practice. The evolution of the kinetic energy and its dissipation rate is computed using several different combinations of subgrid term modeling. The dynamic mixed model that incorporates a similarity component and a dissipative eddy-viscosity component is found to be the most robust model for the convective subgrid-scale stress. The interfacial subgrid-scale model based on the stress-similarity concept is shown to have a potential benefit to large-eddy simulations of turbulent-interfacial flows. An appropriate resolution of the interface is necessary because the model relies on a test-filtering procedure and an extraction of resolved interface information to model the subgrid behavior. Additionally, based on the analysis of the interfacial subgrid contributions, a dynamic procedure for the calculation of the stress-similarity coefficients or a dynamic adjustment of the test-to-gird level filter is also necessary in practical applications.

Breaking-wave impacts on a bottom-mounted vertical circular cylinder have been simulated with large-eddy simulations. The technique used to generate and propagate the regular linear and fifth-order Stokes waves is validated against experimental results. Steep waves are propagated over a sloping seabed resulting in a series of different types of wave impacts on the offshore structure including a regular non-breaking steep wave, a plunging-breaking wave, and spilling-breaking waves. The in-line force on the structure due to a wave that breaks directly in front of the cylinder in a plunging manner is found to be approximately 100% greater than the force due to a steep non-breaking wave. A spilling breaker results in the in-line force

that is 50% greater than the non-breaking wave. The use of subgrid-scale modeling does not influence the force and free-surface elevation prediction when non-breaking waves are studied because of the low level of turbulence and free-surface deformation associated with non-breaking wave impacts. The significant deformation of the free surface and near-interface turbulence generated during wave breaking result in a large subgrid contribution that must be modeled to obtain correct in-line force predictions. An appropriate model for the convective subgrid-scale stress must incorporate resolved-flow information through the scale-similarity concept because purely dissipative eddy-viscosity type of modeling is known to behave poorly near the fluid interface. The contribution of the interfacial subgrid model is found to be important in replicating the peak negative in-line force on the cylinder, but a dynamic coefficient calculation is necessary to adapt the model to the local-resolved-flow conditions.

5.2 Contributions

The major contributions of this work are highlighted here, along with a description of how each contribution impacts the field of numerical simulation of turbulent-interfacial flows.

- The hierarchy the subgrid-scale terms present in the governing equations of multiphase large-eddy simulations has been established for two canonical turbulent-interfacial flows. The relative magnitudes of the subgrid terms related to turbulence and the presence of the interface are quantified during the most important stages of the flow evolution. The comparison of the maximum subgrid contributions to the resolved contributions indicates that the interfacial subgrid term can be significant in marine flows characterized by large density and viscosity ratios. The subgrid interface information is shown to be a strong function of the filter size and its magnitude to be of similar importance as the traditional

convective term also found in single-phase large-eddy simulations.

- The performance of subgrid-scale models in application to multiphase flows is evaluated through the comparison of the correlation between the modeled and the true subgrid-scale stresses. The output of the scale-similarity structural model is found to be highly correlated with the true subgrid-scale stress computed from the direct numerical simulation data. Pure eddy-viscosity modeling of the convective subgrid term is determined to be inappropriate for LES of turbulent-interfacial flows.

- The stress-similarity model is implemented in the LES solver to evaluate the impact of the additional subgrid terms that are a result of the spatial filtering across the interface separating the two immiscible phases. The model is found to be highly sensitive to the resolution of the interfacial scales and the ratio of the test-level to the grid-level filter. Unlike in many single-phase flows, the stress-similarity model coefficient set equal to one is not appropriate for the simulation of complex multiphase flows such as those involving breaking-water waves.

- Impact loads on a vertical circular cylinder due to steep-regular non-breaking and breaking waves are predicted using large-eddy simulations. Subgrid modeling of the convective term is found to be important for a correct prediction of the maximum in-line force and the free-surface elevation occurring at the time of wave breaking. Modeling of the subgrid interfacial term using the resolved features of the interface may be beneficial in simulations of similar turbulent-interfacial flows when combined with a method for a dynamic adjustment of the model coefficient.

5.3 Future Work

The current implementation of the stress-similarity model in the LES solver uses a constant user-specified coefficient. A dynamic calculation of this coefficient based on a second level of test filtering should improve the performance of the model. However, a method for determining a sufficient level of the interface resolution would be necessary in order for the additional test-filtering procedure to use well-resolved information and for the method to yield an appropriate coefficient as a function of space and time.

The evaluation of the subgrid terms for the breaking-wave flow uses a viscosity ratio that is approximately twice the physical ratio. The hierarchy of the subgrid terms is not anticipated to be affected by this deviation from the physical value, but the relative magnitudes of the interfacial and the diffusive terms are likely affected. A parametric study of the influence of the viscosity and density ratios would give a clear guideline as to how sensitive the subgrid terms are to the phase properties.

A detailed comparison of the in-line forces on the cylinder due to impinging-breaking waves against experimental data could clarify the benefits of the various subgrid-scale modeling. Additionally, simulations with a fully-resolved boundary layer on the surface of the cylinder would provide a better insight into the interaction of the viscous boundary layer with the turbulence associated with the wave-breaking process. A detailed description of the turbulent-interfacial features in the proximity of a floating offshore structure may allow for a more accurate prediction of vortex-induced vibrations and motions.

The importance of the local compressibility effects of the air pockets that are entrained during the plunging event may be important to the process of turbulence generation and dissipation. Baumgarten et al. (2002) have shown that the assumption of incompressibility may result in an over-estimation of the bubble breakup energy which may in turn affect the turbulent kinetic energy cascade. In multiphase flows with large viscosity and density rations such as in the case of water-wave flows, the

compressibility effects are likely to be a strong function of the severity of the plunging event and thus their relative impact on the evolution of the flow should be considered in the next stage of this work.

BIBLIOGRAPHY

Apelt, C. J. and Piorewicz, J. Laboratory studies of breaking wave forces acting on vertical cylinders in shallow water. *Coastal Engineering*, 11:263–282, 1987.

Bardina, J., Ferziger, J. H., and Reynolds, W. C. Improved subgrid models for large eddy simulation. *Journal of AAIA*, 80:1357, 1980.

Baumgarten, C., Stegemann, J., and Merker, G. A new model for cavitation induced primary break-up of diesel sprays. *Zaragoza*, 9:11, 2002.

Brackbill, J. U., Kothe, D. B., and Zemach, C. A continuum method for modeling surface tension. *Journal of Computational Physics*, 100:335–354, 1992.

Bredmose, H., Slabiak, P., Sahlberg-Nielsen, L., and Schlutter, F. Dynamic excitation of monopiles by steep and breaking waves. experimental and numerical study. In *ASME2013 32nd International Conference on Ocean, Offshore and Arctic Engineering*, 2013.

Carati, D., Ghosal, S., and Moin, P. On the representation of backscatter in dynamic localization models. *Physics of Fluids*, 7:606–616, 1995.

Chakrabarti, S. K., Kriebel, D., and Berek, E. P. Forces on a single pile caisson in breaking waves and current. *Applied Ocean Research*, 19:113–140, 1997.

Chan, E. S. and Melville, W. Plunging wave forces on surface-piercing structures. In *Journal of Offshore Mechanics and Arctic Engineering*, 1989.

Chan, E.-S., Cheong, H.-F., and Tan, B.-C. Laboratory study of plunging wave impacts on vertical cylinders. *Coastal Engineering*, 25:87–107, 1995.

Chesnel, J., Menard, T., Reveillon, J., and Demoulin, F.-X. Subgrid analysis of liquid jet atomization. *Atomization and Sprays*, 21:41–67, 2011a.

Chesnel, J., Reveillon, J., Menard, T., and Demoulin, F. X. Large eddy simulation of liquid jet atomization. *Atomization and Sprays*, 21:711–736, 2011b.

Chong, M. S., Perry, A. E., and Cantwell, J. A general classification of threedimensional flow fields. *Physics of Fluids*, 2:765–777, 1990.

Christensen, E. D., Bredmose, H., and Hansen, E. A. Extreme wave forces and wave run-up on offshore wind turbine foundations. In *Copenhagen Offshore Wind*, 2005.

Christensen, E. D. and Deigaard, R. Large eddy simulation of breaking waves. *Coastal Engineering*, 42:53–86, 2001.

Chumakov, S. G. *Subgrid models for large eddy simulation: scalar flux, scalar dissipation and energy dissipation.* PhD thesis, University of Wisconsin - Madison, 2005.

Cook, A. W. Determination of the constant coefficient in scale similarity models of turbulence. *Physics of Fluids*, 9:1485–1487, 1997.

Damian, S. M. Description and utilization of interfoam multiphase solver. Technical report, International Center for Computational Methods in Engineering, 2012.

de Ridder, E. J., Aalberts, P., van den Berg, J., Buchner, B., and Peeringa, J. The dynamic response of an offshore wind turbine with realistic flexibility to breaking wave impact. In *ASME 2011 30th International Conference on Ocean, Offshore and Arctic Engineering*, 2011.

de Villiers, E. *The potential of large eddy simulation for the modeling of wall bounded flows.* PhD thesis, Imperial College of Science, Technology and Medicine, 2006.

Dean, R. G. and Dalrymple, R. A. *Water wave mechanics for engineers and scientists.* World Scientific, 1991.

Ferziger, J. H. and Perić, M. *Computational methods for fluid dynamics.* Springer Berlin, 1996.

Frigaard, P., Anderson, T. L., Ramirez, J. R. R., Sorensen, S. P. H., Martinelli, L., Lamberti, A., Troch, P., de Vos, L., Kisacik, D., Stratigaki, V., Zou, Q., Monk, K., Vandamme, J., Damsgaard, M. L., and Gravesen, H. Loads on entrance platforms for offshore wind turbines. In *HYDRALAB III Joint User Meeting Hannover*, 2010.

Fureby, C. Iles and les of complex engineering turbulent flows. *Journal of Fluids Engineering*, 129:1514–1523, 2007.

Germano, M. A proposal for a redefinition of the turbulent stresses in the filtered navierstokes equations. *Physics of Fluids*, 29:2323–2324, 1986.

Germano, M., Pimoelli, U., Moin, P., and Cabot, W. H. A dynamic subgrid-scale eddy viscosity model. *Physics of Fluids*, 3:1760–1765, 1991.

Goda, Y., Haranaka, S., and Kitahata, M. Study of impuslive breaking wave forces on piles. Technical report, Port and Harbour Research Institute, 1966.

Gullbrand, J. and Chow, F. K. The eect of numerical errors and turbulence models in large-eddy simulations of channel ow, with and without explicit ltering. *Journal of Fluid Mechanics*, 495:323–341, 2003.

Hildebrandt, A. and Schlurmann, T. Breaking wave kinematics, local pressures, and forces on a tripod structure. In *Coastal Engineering*, 2012.

Iafrati, A. Numerical study of the effects of the breaking intensity on wave breaking flows. *Journal of Fluid Mechanics*, 622:371–411, 2009.

Iafrati, A. Energy dissipation mechanisms in wave breaking processes: Spilling and highly aerated plunging breaking events. *Journal of Geophysical Research*, 116: 1–22, 2011.

Iafrati, A., Onorato, M., and Babanin, A. Analysis of wave breaking events generated as a result of a modulation instability. In *29th Symposium on Naval Hydrodynamics*, 2012.

Irschik, K., Sparboom, U., and Oumeraci, H. Breaking wave characteristics for the loading of a slender pile. In *28th Int. Conf. Coastal Eng., ICCE*, 2002.

Issa, R. I. Solution of the implicitly discretized fluid flow equations by operator-splitting. *Journal of Computational Physics*, 62:40–65, 1986.

Jacobsen, N. G., Fuhrman, D. R., and Fredsoe, J. A wave generation toolbox for the open-source cfd library: Openfoam®. *International Journal of Numerical Methods in Fluids*, 2011.

Jasak, H. *Error Analysis and Estimation for Finite Volume Method with Applications to Fluid Flow*. PhD thesis, Imperial College, University of London, 1996.

Jasak, H. High resolution NVD differencing scheme for arbitrarily unstructured meshes. *International Journal for Numerical Methods in Fluids*, 31:431–449, 1999.

Kim, J., Moin, P., and Moser, R. Turbulence statistics in fully developed channel flow at low reynolds number. *Journal of Fluid Mechanics*, 177:133–166, 1987.

Kim, W. and Menon, S. A new dynamic one-equation subgrid-scale model for large eddy simulation. In *33rd Aerospace Sciences Meeting and Exhibit*, 1995.

Kornev, N. V., Tkatchenko, I. V., and Hassel, E. A simple clipping procedure for the dynamic mixed model based on taylor series approximation. *Communications in Numerical Methods in Engineering*, 22:55–61, 2006.

Labourasse, E., Lacanette, D., Toutant, A., Lubin, P., Vincent, S., Lebaigue, O., Caltagirone, J.-P., and Sagaut, P. Towards large eddy simulation of isothermal two-phase flows; governing equations and a priori tests. *International Journal of Multiphase Flow*, 33:1–39, 2007.

Lakehal, D. and Liovic, P. Turbulence structure and interaction with steep breaking waves. *Journal of Fluid Mechanics*, 674:522–577, 2011.

Larocque, J., Vincent, S., Lacanette, D., Lubin, P., and Caltagirone, J.-P. Parameter study of LES subgrid terms in a turbulent phase separation flow. *International Journal of Heat and Fluid Flow*, 31:536–544, 2010.

Lilly, D. K. A proposed modification of the germano subgrid-scale closure method. *Physics of Fluids*, 4:633–635, 1992.

Liu, S., Meneveau, C., and Katz, J. On the properties of similarity subgrid-scale models as deduced from measurements in a turbulent jet. *Journal of Fluid Mechanics*, 275:83–119, 1994.

Lubin, P. *Large Eddy Simulation of plunging breaking waves*. PhD thesis, Universite Bordeaux, 2004.

Lubin, P., Glockner, S., Kimmoun, O., and Branger, H. Numerical study of the hydrodynamics of regular waves breaking over a sloping beach. *European Journal of Mechanics B/Fluids*, 30:552–564, 2011.

Lubin, P., Vincent, S., Abadie, S., and Caltagirone, J.-P. Three-dimensional large eddy simulation of air entrainment under plunging breaking waves. *Coastal Engineering*, 53:631–655, 2006.

Meneveau, C. and Katz, J. Scale-invariance and turbulence models for large-eddy simulation. *Annual Review Fluid Mechanics*, 32:1–32, 2000.

Meneveau, C., Lund, T. S., and Cabot, W. H. A lagrangian dynamic subgrid-scale model of turbulence. *Journal of Fluid Mechanics*, 319:353–385, 1996.

Moin, P. and Mahesh, K. Direct numerical simulation: A tool in turbulence research. *Annual Review Fluid Mechanics*, 30:539–578, 1998.

Morison, J. *The force exerted by surface waves on piles*. Petroleum Transactions, AIME, 1950.

Nielsen, A. W., Schlutter, F., Sorensen, J. V. T., and Bredmose, H. Wave loads on a monopile in 3D waves. In *ASME 2012 31st International Conference on Ocean, Offshore and Arctic Engineering*, 2012.

Olsson, E., Kreiss, G., and Zahedi, S. A conservative level set method for two phase flow ii. *Journal of Computational Physics*, 225:785–807, 2007.

Olsson, E. and Kreiss, G. A conservative level set method for two phase flow. *Journal of Computational Physics*, 210:225–246, 2005.

Park, N., Yoo, J. Y., and Choi, H. Toward improved consistency of a priori tests with a posteriori tests in large eddy simulation. *Physics of Fluids*, 17, 2005.

Perlin, M., Choi, W., and Tian, Z. Breaking waves in deep and intermediate waters. *Annual Review Fluid Mechanics*, 45:115–145, 2013.

Piro, D. J. *A Hydroelastic Method for the Analysis of Global Ship Response Due to Slamming Events*. PhD thesis, University of Michigan, 2013.

Pope, S. B. *Turbulent Flows*. Cambridge University Press, 2000.

Ramirez, J., Frigaard, P., Andersen, T. L., and Christensen, E. D. Breaking wave on a slender cylinder: comparison of experimental data and numerical results. In *31st International Conference on Ocean, Offshore and Arctic Engineering*, 2012.

Rusche, H. *Computational Fluid Dynamics of Dispersed Two-Phase FLows at High Phase Fractions*. PhD thesis, Imperial College of Science, Technology & Medicine - University of London, 2002.

Sagaut, P. *Large eddy simulation for incompressible flows*. Springer Berlin, 2001.

Salvetti, M. V. and Banerjee, S. A priori tests of a new dynamic subgrid scale model for finite difference large eddy simulations. *Physics of Fluids*, 7:2831–2847, 1995.

Sarghini, F., Pimoelli, U., and Balaras, E. Scale-similar models for large-eddy simulations. *Physics of Fluids*, 11:1596–1607, 1999.

Scardovelli, R. and Zaleski, S. Direct numerical simulation of free-surface and interfacial flow. *Annual Review of Fluid Mechanics*, 31:567–603, 1999.

Shen, L. and Yue, D. K. P. Large-eddy simulation of free-surface turbulence. *Journal of Fluid Mechanics*, 440:75–116, 2001.

Smagorinsky, J. General circulation experiments with the primitive equations. Technical report, Department of Commerce - Weather Bureau, 1963.

Song, C. and Sirviente, A. I. A numerical study of breaking waves. *Physics of Fluids*, 16:2649–2667, 2004.

Toutant, A., Chandesris, M., Jamet, D., and Lebaigue, O. Jump conditions for filtered quantities at an under-resolved discontinuous interface. part 1: Theoretical development. *International Journal of Multiphase Flow*, 35:1100–1118, 2009.

van Haren, S. W. Testing DNS capability of OpenFOAM and STAR-CCM+. Master's thesis, Delft University of Technology, 2011.

Vincent, S., Larocque, J., Lacanette, D., Toutant, A., Lubin, P., and Saguat, P. Numerical simulation of phase separation and a priori two-phase LES filtering. *Computers and Fluids*, 37:898–906, 2008.

Vreman, B., Geurts, B., and Kuerten, H. A priori tests of large eddy simulation of the compressible plane mixing layer. *Journal of Engineering Mathematics*, 29:299–327, 1995.

Watanabe, Y., Saeki, H., and Hosking, R. J. Three-dimensional vortex structures under breaking waves. *Journal of Fluid Mechanics*, 545:291–328, 2005.

Whitham, G. B. *Linear and Nonlinear Waves*. John Wiley & Sons, 1974.

Wienke, J., Sparboom, U., and Oumeraci, H. Breaking wave impact on a slender cylinder. In *Coastal Engineering Conference*, 2001.

Zang, J., Taylor, P. H., and Tello, M. Steep wave and breaking wave impact on offshore wind turbine foundations - ringing re-visited. In *25th International Workship on Water Waves and Floating Bodies*, 2010.

Zang, Y., Street, R. L., and Koseff, J. R. A dynamic mixed subgrid-scale model and its application to turbulent recirculating flows. *Physics of Fluids*, 5:3186, 1993.

Zhao, Q., Armfield, S., and Tanimoto, K. Numerical simulation of breaking waves by a multi-scale turbulence model. *Coastal Engineering*, 51:53–80, 2004.